Photoresponsive gold nanoparticles : towards multi-functional organic electronics devices

Corinna Raimondo

UNIVERSITÉ DE STRASBOURG

UNIVERSITÉ DE STRASBOURG

EDSC
Ecole Doctorale des Sciences Chimiques

ÉCOLE DOCTORALE DES SCIENCES CHIMIQUES

[UMR 7006 - Institut de Science et d'Ingénierie Supramoléculaires]

THÈSE

présentée par

Corinna RAIMONDO

soutenue le : **22 Juin 2012**

pour obtenir le grade de

Docteur de l'université de Strasbourg

Discipline / Spécialité : Chimie

Photoresponsive gold nanoparticles: Towards Multi-functional Organic Electronics Devices

THÈSE dirigée par :

M. SAMORì Paolo	Professeur, Institut de Science et d'Ingénierie Supramoléculaires, Universitè de Strasbourg

RAPPORTEURS :

M. CALAME Michel	Lecturer, University of Basel
M. BASSANI Dario	Directeur de Recherche, CNRS Bordeaux

MEMBRES DU JURY :

M. HOSSEINI Wais	Professeur, Universitè de Strasbourg
M. CALAME Michel	Lecturer, University of Basel
M. BASSANI Dario	Directeur de Recherche, CNRS Bordeaux
M. SAMORì Paolo	Professeur, I.S.I.S., Universitè de Strasbourg

Acknowledgements

It is a great pleasure to thank my supervisor, Paolo Samorì for allowing to live my first not-Italian experience, working in his group on challenging and really exciting projects, letting me try all the crazy ideas I had and pushing me on the one I couldn't believe could work (by the way, on most of them you were absolutely right). I really need to thank him for standing my opinionated personality; I know it is not always easy. It has been a great experience.

I would like to thank Hiroshi Uji-i and Johan Hofkens for allowing me working in their groups, for the "science" and their way to face it, for the lab evenings and the support. It has been great visiting Leuven.
I would like to thank our collaborators: Marcel Mayor, Federica Reinders and Fabian Sander, for the synthesis of the molecule, the discussions and the help with the TEM images. It was a great pleasure as well to collaborate with Bernard Doudin and Vina Faramarzi for the nanotrenches electrodes.
I wish to thank Gerald J. Meyer for the fruitful discussions over complex kinetical processes and to Thomas Ebbesen for the tips on how to write papers and on the discussions about the scientific world.

A special thanks goes to Cristiana, Masako and Nina, brilliant examples of how it is not necessary to choose between family and career.

I am truly in debt with Marie-Claude, for helping me out in all the burocracy and especially for taking care of all my mistakes and adventures. Thank you very much.

This thesis could not even start without the help of quite a few people. First of all James, who always supported me, believed in me, thought me so much about becoming a scientist (and a grown-up as well), and was always ready to help me with endless English issues. Thank you so much!
Anna, for the talks, the sharing and the solid example. Thank you very much, dear.

Gael, because I deeply trust him (you are great) and I know our paths will cross again.
Petr, because without you I couldn't have any decent NMR in my thesis, for the never boring sharing, and not ever trivial answers to whatever topic.
Pierre, for being just there every time I need you, thanks.

All the people who red, re-red, and tried to understand my thesis, in particular Jeni, Olli, James, Pierre, Ashleigh, Artur, Ema and of course Paolo. I owe you.

I need to thank the people who welcomed me here, most of all Adi and Selvaggia without whom I could have slept under a bridge. Barbara because I'll never forget my first French movie (in Chinese with French subtitles), because of the bike lessons, of the "tortelli di zucca" and because you have been a friend. Alvaro, for the supporting while everything was messed up.

Who allowed me feeling at home, i.e. my dear flatmates Anna, Ashleigh, Gabrielle, Lucas and Men. You have been really important to me, essential indeed, and you are all truly great people.

The friends who shared the path Alex, Celine, Claudio, Deniz, Ema, Estelle, Fredrick, Gareth, Ghislaine, Giangi, Irene, Jose, Maria Giovanna, Manuel, Massimo, Mihai, Nuria, Pierre, Sabine, Serena, Silvia, Susana, Thomas, Ylenia, Victoire, Viola. My life in Strasbourg could have been much more difficult without you. Thank you.
Expecially Celine, Estelle and Maria Giovanna for always showing me that you care. To Massimo for the numerous dinners and your modesty. To Giangi for the guitar-singing afternoons, the hugs and the sharing, I am happy you came. To Viola, as an example of strength, forgiveness and sympathy.

I feel in debt with the ISIS people, especially the first floor denizens, for the random talk in the corridors and the discussions about science and life. In particular a special thanks goes to Aurelian, Ben, Cyriaque, Yuri, Manu, Tal, Juemin.

All my lab-mates for the fruitful discussions: Carlos-Andres, Cristiana, Francesca,

Gabriella, Karima, Leszek, Luc, Massimo B., Markus, Pasquale, Sebastian, Tim.
In particular:
Anna L. for the few, but truly worth to remember discussions, thanks.
Jeff for all you taught me on the AFM.
Rebecca, because most of the time the real intelligence is not understood.
Matthias, for the smart questions and most of all for the "example of equilibrium" that you have been.
Mirella, for taking care of all the small things we always forget.
J.Olly, because are theories that "make the world go round".
Artur, for the endless suggestions on how to menage my working (and not only) life.
Ema, for the sharing in our office, the scientific discussions, and that pinch of Opera that always makes me smile.
Chiara, because when I was lost you were there.
Maria, for the support and the sharing.
Oliver for your way to "suggest" I am wrong, and for the great support and help in this last part of my thesis.
Silvia, for everything we lived together, talks, laughs, holidays, demonstrations and arguments.
Appan, for the suggestion to how to live a healthier life, and most of all for your kindness.
A special thanks goes to Nuria, for the long lab evenings, the "supporting food" and the discussions.

I would like also to thank all the lab-mates in Leuven, it has been awesome.

I am grateful to my Marie-Curie co-fellows in particular to Petra for all the help you gave me, for the real friendship and because everything is just really easy with you.

To the "Monday beer folks" because even Monday, thanks to you, looks like a wonderful day.

I need to thank my closest friends, the "comari", because having a skype-laugh with you

gives me energy and because when everything in my life goes to hell, you are there.

Thanks to my parents, Mario and Marina, you have been the greatest example.
To my aunt and oncle, Angela e Oriano, because I know it hasn't been easy, I am truly lucky.
To my brother, Andrea, for the random talks, the similar chosen path, the difficult but full, understanding or each other feelings; I am really happy you are here.

Last but not least, who is sharing the everyday life with me, who hugged me, woke-me –up, cleaned and did the grocery shopping while I was getting crazy for this thesis. The person that daily reminds me the full picture (most of the time exaggerated) of my potential. I didn't think I could find such a creative, bright and caring person, with whom life becomes so easy. Ti amo, Tesoro.

To Mario and Marina,

Table of Contents

Résumé de thèse

“Vers des dispositifs organo-électroniques à réponses multiples”

Les trois dernières décennies ont vu l’émergence de l’Electronique Organique (Organique Electronics) ainsi que son établissement en tant que domaine scientifique interdisciplinaire ayant pour objectif d’exploiter les propriétés intrinsèques des molécules afin de pouvoir créer des dispositifs tels que des diodes électroluminescentes, des transistors à effet de champs ou des cellules solaires. Ces dispositifs font désormais partie intégrante de notre vie quotidienne, étant présents dans de nombreux objets (écrans, lames de rasoir, téléphones mobiles,…)

On dénombre actuellement deux défis scientifiques majeurs dans ce domaine. Le premier est de s’attacher à augmenter l’efficacité des dispositifs par l’utilisation de nouveaux matériaux, l’amélioration des procédés techniques ou la création de dispositifs à topologie inédite. Le deuxième consiste en l’intégration de fonctionnalités multiples un seul dispositif, en particulier à travers la conception de systèmes à réponses multiples et de dispositifs modulables par l’exposition à divers stimuli indépendants les uns des autres (lumière, signaux électriques ou magnétiques,…) [1] Atteindre ces objectifs nécessite la compréhension des mécanismes fondamentaux de la physico-chimie, gouvernants les propriétés de base de l’électronique organique tels l’injection ou le transfert de charge et le transport.

L’objectif de ces travaux de thèse est donc le développement de systèmes complexes, auto-assemblés, électro-actifs, dont les propriétés électriques et optiques au sein de dispositifs organo-électroniques peuvent être modulées en réponse aux stimuli extérieurs. Une attention toute particulière a été portée à la fabrication de transistors à effet de champ organique dans lequel le courant de jonction peut être contrôlé de deux

manières : optiquement (contrôle photochimique) ou électriquement (contrôle de l'électrode « gate »).

Ce but a pu être atteint en développant nos propres briques élémentaires et par l'étude de leurs propriétés physico-chimiques afin de modéliser tous les mécanismes impliqués. Le système choisi appartient à la famille des entités photo-sensibles, dans ce cas le choix s'est porté sur les azobenzènes. Leur isomérisation entre deux état stables et largement étudiés, appelés *trans* et *cis*, contrôlé par la lumière, est relativement facile à contrôler et à caractériser. La photo-isomérisation entre l'état *trans* et *cis* peut être induite par irradiation UV alors que l'isomérisation inverse de l'état *cis* vers l'état *trans* est induit par irradiation par lumière visible ou thermiquement.

Un dérivé de l'azobenzène fonctionnalisé par une unité thiol (AZO, Image 1), synthétisé dans sa forme protégée par un groupe thioester, a été choisi au vu des résultats précédents étudiant sa chimisorption sur une surface d'or -Au(111)- formant des monocouches auto-assemblées. Elles présentent un très haut degré d'isomérisation, une grande stabilité, même pour la forme *cis* généralement instable (prouvée par la mesure d'une constante d'isomérisation *cis* vers *trans* environ quatre fois plus grande sur surface qu'en solution). Ce comportement inédit a été attribué aux fortes interactions intermoléculaires dans la monocouche auto-assemblée.

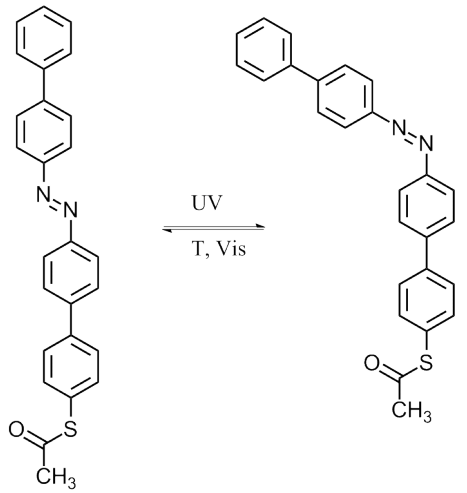

Image 1 : Structure et reaction d'isomérisation du compose AZO protégé par un acetyl thioester

L'incorporation de cette monocouche dans des dispositifs bi-fonctionnels (tel que ceux basés sur C-AFM ou une goutte de mercure à jonction verticale), les deux états photo-stationnaires ont présentés des résistance d'effet tunnel bien différentes l'une de l'autre.[2,3] En dépit de l'importance de ces résultats, l'utilisation de jonctions horizontales semble cruciale pour toutes les applications technologiques.

Les résultats de ces travaux de thèse tentent de répondre à trois questions majeures :

- Comment intégrer des azobenzènes dans un dispositif à géométrie horizontale pour créer deux jonctions terminales photo-commutable ?
- Quel est le rôle des interactions intermoléculaires dans les processus d'isomérisation d'azobenzènes dans le cas de monocouches denses ?
- Comment obtenir le degré de contrôle le plus élevé dans l'utilisation de monocouche d'azobenzènes pour photo-moduler le transport de charges dans un transistor organique à effet de champ ?

Nous avons tout d'abord testé la capacité à mesurer la commutabilité d'un courant photo-modulé par un azobenzène. Ceci a été effectué en incorporant des jonctions horizontales en créant un dispositif basé sur des électrodes métalliques planes, séparées de 100 nm, et reliées entre elles par des microsphères recouvertes de monocouches d'azobenzènes (schéma et mécanisme d'opération dans l'Image 2).

Le circuit présente une commutation induite par la lumière, avec une reproductibilité supérieure à 90%, démontré statistiquement, et comparé avec les jonctions contenant des couches d'alcanes thiols, non sensibles à la lumière.[4]

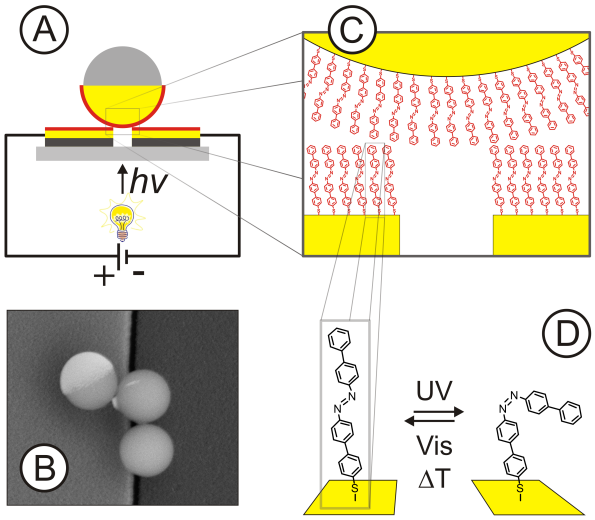

Image 2 (A) Représentation schématique du circuit moléculaire. Une particule de silice de type Janus contenant un hémisphère d'or. Cet hémisphère d'or et l'électrode d'or planaire (en jaune) sont tous les deux recouverts par une monocouche auto-assemblée adsorbée chimiquement (en rouge), soit de dodécanethiol, soit d'azobenzène. (B) Image par microscopie électronique à balayage des microsphères d'1 µm de diamètre et bloquée au-dessus d'une tranchée préparée par lithographie électronique. La sphère en haut à gauche, non bloquée par la tranchée révèle que le revêtement se trouve sous la sphère, reliant les deux électrodes. (C) Image des interactions entre les molécules dans la géométrie présente. (D) Réaction chimique de *cis-trans* isomérisation de l'azobenzène bi-phénylique fonctionnalisé par un thiol terminal.

L'échelle de cette approche a été réduite en utilisant des électrodes espacées de 50 nm reliées par des nanoparticules d'or de 80 nm de diamètre couvertes d'azobenzènes. Les propriétés photo-sensibles d'un tel système ont été explorées aussi bien en testant un dispositif modèle que par des mesure par c-AFM.

Les transistors à effet de champs semblent être des éléments clés pour les nouvelles entités logiques basées sur une structure organique. Il a été récemment montré qu'une photo-réponse pouvait être intégrée à ces transistors en adsorbant chimiquement des monocouches d'azobenzènes sur les électrodes source et drain, afin de contrôler photo-chimiquement l'injection de charges à l'interface.[5] Une amélioration du courant photo-modulé peut être envisagée en intégrant un grand nombre d'azobenzène dans le transistor. Ceci peut être obtenu en employant des nanoparticules d'or recouvertes d'azobenzènes. Elles présentent des propriétés optiques, électroniques pré-programmées, dépendantes de leur taille et qui diffèrent de manière spectaculaire de celles dans le métal. Le comportement de ces nanoparticules d'or recouvertes

d'azobenzènes a tout d'abord été étudié en termes de quantité de molécules et de cinétique d'isomérisation. 4 tailles différentes (diamètre de 1, 3, 15, 30 nm) de nanoparticules ont été synthétisées et analysées par ^{1}H-RMN, MET, spectroscopie UV-Vis. Ces systèmes présentent un processus d'agrégation/désagrégation particulier et un comportement cinétique dépendant de la taille des objets étudiés (Image 3).[6] Une meilleure compréhension de ces mécanismes a pu être atteinte par des études cinétiques démontrant le rôle des interactions intermoléculaires dans le processus d'isomérisation (rendement et stabilité de la forme *cis*).

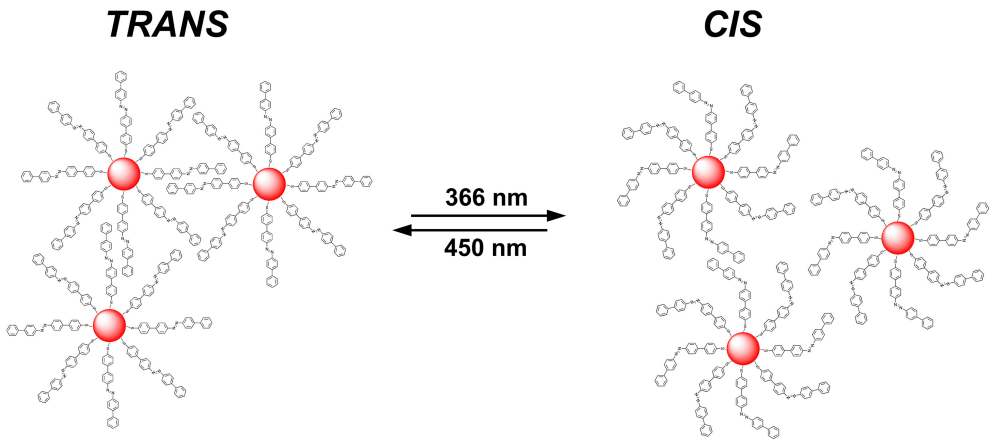

Image 3 Représentation des interactions entre les molécules AZO recouvrant les particules d'or dans les deux formes d'isomérisation.

En combinant l'adaptation physico-chimique des différentes interfaces il a aussi été possible de créer un transistor à effet de champ présentant une augmentation du courant. En particulier la couche semi-conductrice a été préparé en mélangeant un polymère dopé p (du poly(3-hexylthiophene - P3HT) avec les nanoparticules d'or couvertes d'azobenzènes, menant à différentes propriétés de sorties et de transfert pour ce dispositif aussi bien qu'une capacité à stocker des charges dépendante de l'isomère initialement choisi pour la préparation du dispositif. Il a pu être montré que ces transistors sont capables de commuter entre deux différents états de courant en fonction de la longueur d'onde d'irradiation. Ceci a pu être reproduit sur plus de 25 cycles consécutifs sans signe de fatigue détéctable.[7] Une image du dispositif est présentée dans l'Image 4.

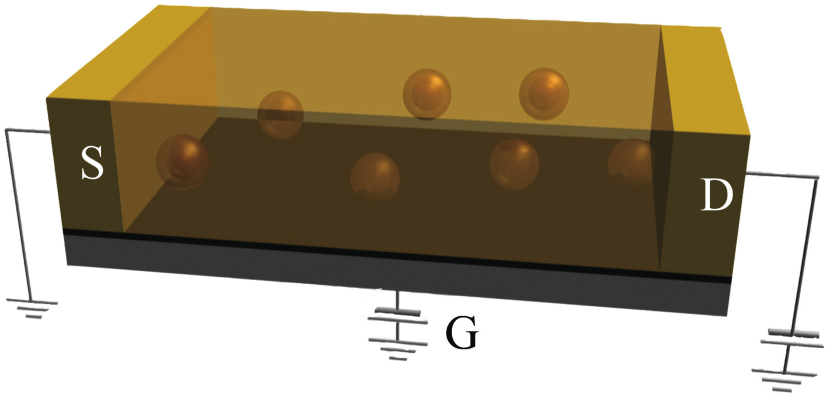

Image 4 Représentation du dispositif

En conclusion, il a pu être montré que des monocouches auto-assemblées d'azobenzènes adsorbées chimiquement sur des surface planes ou non sont des outils puissants pour la fabrication de dispositifs électroniques organiques. En particulier une double fonctionnalité a pu être transmise à un transistor à effet de champ qui peut être modulée aussi bien électriquement qu'optiquement. Ces résultats ouvrent la voie à de nouvelles solutions dans les transferts digitaux entre signaux optiques et électriques. Il est même possible d'envisager l'utilisation de ces transistors photo-commutables pour différentes applications liées à la détection chimique.

Références:

1. Y.L. Guo, G. Yu, Y.Q. Liu, *Advanced Materials*, **2008**, 22, **4427-4447**.
2. J. Mativetsky, G. Pace, M.A. Rampi, M. Mayor, P. Samorì *J. Am. Chem. Soc.* **2008**, 130, **9192-9193**.
3. V. Ferri, M. Elbing, G. Pace, M. Zharnikov, P. Samorì, M. Mayor, M.A. Rampi, *Angew. Chem. Int. Ed.* **2008**, *47*, **3407-3409.**
4. V. Faramarzi, C. Raimondo, F. Reinders, M. Mayor, P. Samorì, B. Doudin, *APL*, in press.
5. N. Crivillers, E. Orgiu, F. Reinders, M. Mayor, P. Samorì, *Advanced Materials* **2011**, 23, **1447-1452**.
6. C. Raimondo, F.Reinders, U.Soydaner, M.Mayor, P.Samorí, *Chem. Comm.,* **2010**, 46, **1147 – 1149**.
7. C.Raimondo, N.Crivillers, F.Reinders, M.Mayor, P.Samorí (manuscript in submission)

Chapter 1. Introduction

"Technology extends our ability to change the world"
American Association for the Advancement in Science

Some of the main technological challenges in the upcoming years are related to energy efficiency and (renewable) materials. In this frame organic and polymer based (opto)electronics appears as a smart solution. Continuously increasing worldwide request for technological supplies, stimulate the search for new ways to create devices relying on smaller amount of materials and operating with lower energy consumption.

By mimicking Nature, chemists have put a great effort in the synthesis of new non-natural materials based on small (organic) molecules and polymers that are functional by design.[1] Single molecules are nowadays able, for example, to move objects aside or lift them, to accumulate and release charges, to undergo specific reactions when subjected to a certain external stimulus, etc.[2] The creation of these functional materials requires an in-depth multiscale understanding of the physico-chemical processes involved, which can be obtained both through theoretical and experimental studies.

By mastering this approach in the last decade many discoveries have been made on fundamental electronic, optical, mechanical, magnetic and biologic properties of materials down to the nanoscale.[3] A great effort has been devoted to the synthesis of nanostructured materials, allowing the achievement of a fair control over the sizes and the properties of the materials themselves.[4,5] From another point of view, the development of software packages enabling fast computing (*ab-initio* and molecular dynamic simulations) have made it possible to unravel the electronic structures of the systems and the chemical bonding.[6] It has also been also possible to achieve a better understanding of interfaces both from an experimental and theoretical point of view, and statistical theories have been developed in order to better understand complex nanostructured materials.[7] The use of self-assembly of molecules has been scaled up to be useful in applications,[8-10] measuring probes have been created in order to achieve insights at the molecular level; single-charge, single-spin and phononic vibrations have been probed at the nanoscale, for instance by mean of scanning probe techniques.

Nevertheless, many issues have to be solved or improved. The failure ratio at the laboratory scale, for example when working with nanodevices is still to high to allow scaling-up. No complete understanding of all the processes involved at the nanoscale have been reached yet. Long-term stability and consistent response when an external impulse is applied are not yet achieved, *i.e.* degradation and reliability issues are still present in organic-based materials. Low-cost and "green devices" still need to be created to allow worldwide spread of technology.

To allow understanding of the studied system and to overcome the problems listed above, a possibility relies in the integration step by step of functionalities in devices and the employment of complementary techniques in order to understand all the processes involved.

In a multicomponent material, each component can confer to the ensemble a given function. The integration of more components in a single material or device represents a solution to multifunctionality, i.e. to the integration of multi-gating capacities in a single device. This is the field of responsive systems that when subjected to an external stimulus, like a change in pH, light irradiation, electrochemical stimulus, etc., undergo a well-defined state change. Among responsive materials, photochromic molecules have attracted increasing attention. The possibility to tune their physico-chemical properties, by an external stimulus, makes

them particularly interesting also in the fields of molecular motors, switches and so on.[11-14] In addition, light represents a cheap, renewable and clean stimulus.
Coupling the photochromic properties of these molecules with the characteristics typical of inorganic nanostructured materials allows not only their controlled integration in devices but also the exploitation of, for example, the single electron charging characteristics of nanomaterials dependent on quantum sizes effects.

In this thesis a well-defined photochromic molecular building-bock, i.e. a thiolated bi-phenyl based azobenzene, is coupled with different nanostructured systems. The properties of the hybrid architectures are explored and exploited to fabricate multifunctional (nano)devices.

The thesis is divided in two main parts: one treats the system from a fundamental point of view whereas the second is focused on the applications.
In particular',

- Chapter II describes the theoretical background of the research. First the basic properties of materials through interactions between them mainly from a charge transfer point of view, nanojunctions, nanoparticles and organic field -effect transistors are presented. Then the physical-chemistry behind the instruments used is outlined.

- Chapter III mainly deals with all the experimental techniques already published in literature that have been used in the framework of the thesis and both the devices characterization, including the chosen way to extract data from the devices. The design of the basic building blocks of this thesis is outlined here.

- Chapter IV focuses on the understanding of the properties of the basic nanostructured building blocks utilized in this thesis, i.e. the nanoparticles. Characterization of both its aggregation/solvation behavior and the kinetics of isomerization are presented, along with surface enhanced Raman spectroscopy results.

The applicative part includes

- Chapter V, presenting the integration of the tested molecule and building blocks into nanogap electrodes of different sizes.

- Chapter VI, reporting the integration of azobenzene coated Au nanoparticles in an organic field-effect transistor, to obtain photoresponsive organic field-effect transistor.

Chapter VII summarizes the thesis and provides outlooks in the field.

References

1 Muller, T. J. J. & Bunz, U. H. F. Functional Organic Materials. *Wiley-VHC* (2007).

2 Balzani, V., Credi, A. & Venturi, M. Molecular Devices and Machines. *Wiley-VHC* (2004).

3 Baird, D., Nordmann, A. & Shummer, J. Discovering the nanoscale. *IOS Press, Amsterdam* (2009).

4 Grzelczak, M., Perez-Juste, J., Mulvaney, P. & Liz-Marzan, L. M. Shape control in gold nanoparticle synthesis. *Chemical Society Reviews* **37**, 1783-1791 (2008).

5 Wiedwald, U. & Ziemann, P. Preparation, properties and applications of magnetic nanoparticles. *Beilstein Journal of Nanotechnology* **1**, 21-23 (2010).

6 Schatz, G. C. Using theory and computation to model nanoscale properties. *Proceedings of the National Academy of Sciences of the United States of America* **104**, 6885-6892 (2007).

7 Mello, P. A. & Kumar, N. Quantum Transport in Mesoscopic Systems. *Oxford University Press* (2004).

8 Bogwe, R. Self-assembly: a review of recent developments. *Assembly Automation* **28**, 211-215 (2008).

9 Zhou, Y. F. & Yan, D. Y. Supramolecular self-assembly of amphiphilic hyperbranched polymers at all scales and dimensions: progress, characteristics and perspectives. *Chemical Communications*, 1172-1188 (2009).

10 Whitesides, G. M. & Grzybowski, B. Self-assembly at all scales. *Science* **295**, 2418-2421 (2002).

11 Lehn, J. M. Conjecture: Imines as unidirectional photodriven molecular motors-motional and constitutional dynamic devices. *Chemistry-a European Journal* **12**, 5910-5915 (2006).

12 Huang, T. J. *et al.* A nanomechanical device based on linear molecular motors. *Applied Physics Letters* **85**, 5391-5393 (2004).

13 Colasson, B. X., Dietrich-Buchecker, C., Jimenez-Molero, M. C. & Sauvage, J. P. Towards molecular machines and motors based on transition metal complexes. *Journal of Physical Organic Chemistry* **15**, 476-483 (2002).

14 Sauvage, J. P. Transition metal-containing rotaxanes and catenanes in motion: Toward molecular machines and motors. *Accounts of Chemical Research* **31**, 611-619 (1998).

Chapter 2. Theoretical background

In the following chapter an overview of the theoretical backgrounds of this thesis is presented. First materials and devices are described mostly from a charge transfer point of view, then a description of the physical-chemistry behind the techniques employed is presented.

2.1 Different kind of materials (metal-semiconductors-insulators)

A solid material exhibits numerous properties. Among them it can be classified depending on its conductivity (σ) and conductivity behavior within temperature, σ(T). In inorganic chemistry, a metal is a solid having high σ that decreases upon increasing of the T. A semiconductor has instead lower σ that increase within T while an insulator has really low σ and no T temperature dependence.

An easy way to compare the different materials from this point of view is using the molecular orbital theory (MO) that describes the different molecules as formed by molecular orbitals, each one weighted combination of the atomic orbitals of the atoms composing the molecule. The MO theory represents the different conductivity scenario by comparing the band gap for each system (Figure 2.1.1). The occupation function and the dependence of the resistivity from the temperature are shown in Figure 2.1.1 as well.

In metals the conduction band is partially filled with conduction electrons having lower energy then the Fermi energy ($E<E_F$). The states just above the Fermi energy can be easily occupied by the electron just below. The conduction electrons can move freely in a perfect crystal.

In an insulator, instead, the valence band is completely filled and the conduction and valence bands are separated by an energy gap called E_g. To be able to conduct, a charge carrier in the valence band requires $\Delta E>E_g$ to become a conduction charge carrier.

In a semiconductor the band structure is similar to the one of insulators but with a much smaller E_g, typically in the order of 1-3 eV.

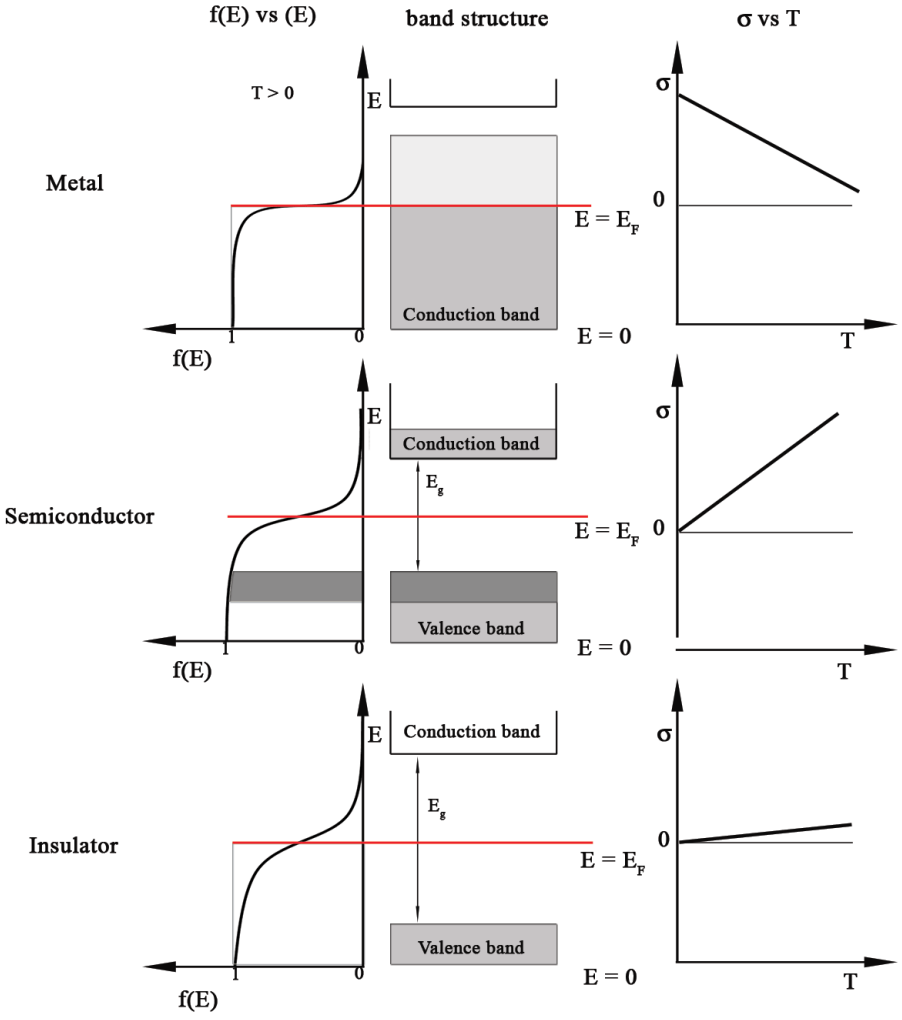

Figure 2.1.1 Occupation function (derived from the Fermi-Dirac statistics), MO representation of the bands and dependence of the conductivity from the temperature for inorganic metals, semiconductors and insulators.

At a temperature equal to 0 K, the energy of the last occupied orbital, the Fermi level, (named HOMO in MO nomenclature) is the Fermi energy, and all orbitals at lower energies are fully occupied.

The population of molecular orbitals follows the Fermi-Dirac distribution presented in equation 2.1:

$$f(E) = \frac{1}{e^{-(E-\mu)/kT}+1} \qquad (2.1)$$

Where, E is the energy of the considered level, μ is the electronic chemical potential, k is the Boltzmann constant and T is the temperature of the system.

Decreasing the band gap, the σ of the solid material will increase. The T dependence can be instead explained considering that in the metals increasing the T the phononic vibrations will increase with consequent decrease in electron's mean free path. In semiconductors instead increasing the T will mean increasing the thermal excitation and allowing more carriers to overcome the band-gap and this effect dominates the increase in scattering. In insulators the band-gap is high enough not to allow any significant conductivity, in this case a variation of T will not help/prevent any transport.

To describe organic materials theoretically, thanks to the MO theory with the LCAO (Linear Combination of Atomic Orbitals) approximation and the Hückel method, it is possible to resolve the Hamiltonian for organic molecules as well. The result is a band structure similar to the one obtained for inorganic materials.

It is then possible to theoretically describe organic materials actually behaving as metals, semiconductors and insulators.

It is worth mentioning that the theoretical description, just cited, of conduction in organic materials is a rough approximation of the processes involved in these materials. Until now, to my knowledge, no full quantitative and qualitative description of these materials has been achieved even if an increasing effort of matching experimental results with theoretical predictions allowed development of models that quite accurately describe the experimental evidence.

Examples of organic conductors (and semiconductors) are charge-transfer salts as metal dithiolenes. These are normally fully conjugated molecules, having planar π

molecular orbitals, characterized by donors and/or acceptors properties. The π-donors and/or acceptor are segregated in domains and partially charged.[1-4]

Organic and inorganic insulators are, from a charge transfer point of view equivalents.

The only differences are related to the applications since, theoretically, organic dielectrics should be easily modifiable by synthesis, allowing proper tuning of the dielectric constant, the molecular packing, etc. Until now the best results and reproducibility have been found for inorganic dielectrics but research on organic dielectrics is ongoing.

An in-depth overview of the Organic Semiconductors and the charge transfer mechanisms involved are reported in the following subchapter.

2.1.1 Organic Semiconductors

When comparing organic and inorganic semiconductors one of the main differences is the absolute value of the mobility. The inorganic semiconductors have in fact three order of magnitude higher mobility compared to the organic ones. To understand the process it is necessary to consider the different chemical nature of the two systems.

Organic solids can posses a high degree of both short-range and long-range order.

When an organic molecule is aromatic or conjugated, the $2p_z$ orbitals on each carbon atom will interact with each other and the π electrons will delocalize over the molecule on the bonding orbitals. The antibonding orbitals (at higher energy) will remain empty. In these classes of organic compounds the Kronig-Penney Model can be applied.[5]

In molecular crystals, the high degree of order and relatively strong forces between the single atoms in the molecules can be in contrast with the weaker van der Waals intermolecular forces. This is one of the main reasons of smaller mobility in organic semiconductors. In this case the orbitals description deriving from the molecular orbital theory is still applicable even if, when moving towards the solid state, a shift in the energetic levels will occur (Figure 2.1.2).

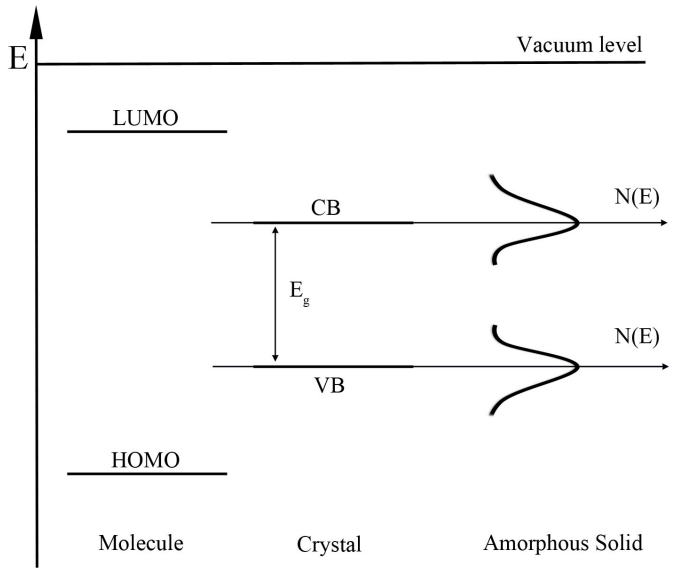

Figure 2.1.2 Plot E (energy) versus N(E) (density of states), representative of the difference in MO for a molecule in vacuum, a molecular crystal and an amorphous solid. HOMO and LUMO are respectively the Highest Occupied Molecular Orbital and the Lowest Unoccupied Molecular Orbital, CB and CV are respectively the conduction and valence bands.

Particularly interesting both from a fundamental and an application point of view, are semiconducting organic polymers. The type of molecules and bonds forming the polymer, i.e. the strength of interaction between neighboring orbitals, determines the extent of the conjugation and is one of the main factors determining the conductivity of the chain. If all the bonds are saturated, no conjugation is present and the electrons will barely delocalize. In this case the polymer will have a band gap high enough to be considered an insulator. When instead unsaturated bonds are present, the degree of delocalization rise decreasing the band gap energy and making possible the existence of a conductive or semi-conductive polymers.

In a very simple case, taking into account the simple example of a linear polymer composed of N atoms separated by a distance d, it will be possible to approximate the total polymer length to Nd. In this case, the Schrödinger wave equation for an electron confined in a one-dimensional box will give the eigenenergies in equation 2.2.

$$E_m = \frac{\hbar^2 \pi^2 n^2}{2m(Nd)^2} \qquad (2.2)$$

Where, m is the mass of the electron and n is a quantum number, ħ is the reduced Planck constant.

If the N p orbitals in the polymeric chain have, according to Pauli, 2 electrons fin each orbital, HOMO and LUMO energies will be computable according to equation 2.3 and 2.4

$$E_{HOMO} = \left(\frac{N}{2}\right)^2 \left[\frac{\hbar^2\pi^2}{2m(Nd)^2}\right] \tag{2.3}$$

$$E_{LUMO} = \left(\frac{N}{2}+1\right)^2 \left[\frac{\hbar^2\pi^2}{2m(Nd)^2}\right] \tag{2.4}$$

and the resulting band gap will be (equation 2.5):

$$E_g = E_{LUMO} - E_{HOMO} = (N+1)\left[\frac{\hbar^2\pi^2}{2m(Nd)^2}\right] \approx \frac{\hbar^2\pi^2}{2md}\left(\frac{1}{N}\right) \tag{2.5}$$

From the last equation it is evident that the band gap is inversely proportional to the polymer chain length, vanishing for macroscopic dimensions.

This physical description doesn't take into account the fact that the lowest energy for the overall system is governed by Peierls distortion. The lowest energy, i.e. most stable, geometry doesn't correspond to the metallic case in which the electrons are fully localized over the backbone but to a semiconductive state in which the electrons are localized and resonate between neighboring bonds. Even in the polymeric case another important factor limiting the mobility is the intermolecular transport.

Another important factor that need to be considered is the geometry of the chain, the overlap between the single atomic orbitals, in fact, can occur only if the overlapping is geometrically allowed. A rotation of the bonds, for instance due to hindered side groups in the polymeric chain will decrease the overlap, hence the conjugation length.

2.1.2 Conductivity and mobility in polymers

The following thesis work will focus attention mostly on semiconducting polymers in the solid state, which is the reason why a more in-depth explanation of the factors involved in the electrical and morphological characteristics of these materials is presented here.

From an intramolecular point of view, the conductivity in polymers mainly depends on three factors: the number of the charge carriers and their mobility and the morphology of the solid.

The number of charge carriers depends on the chemical structure, on the doping and on the presence of topological defects in the backbone.

From a charge carriers mobility point of view, as previously stated, the reported mobilities for organic semiconductors are much lower compared to their inorganic counterparts. To understand this difference in behavior it is necessary to address the factors determining the mobility of an electron in a solid material. There are two extreme scenarios: complete delocalization or complete confinement of the charge carrier. In the case of full delocalization, the conduction derives from the excitation of an electron that is an orbital delocalized on the overall material. In this case the resistance is only due to phononic, electronic or defect mediated scattering processes. If instead the charge carrier is highly localized, the conduction process will be due to hopping between neighboring sites. Being highly improbable that there are no defects in the semiconductor's backbone, the most probably process will involve hopping. The main difference between the two extreme cases is: one is phonon limited while the second is phonon assisted (Figure 2.1.3).

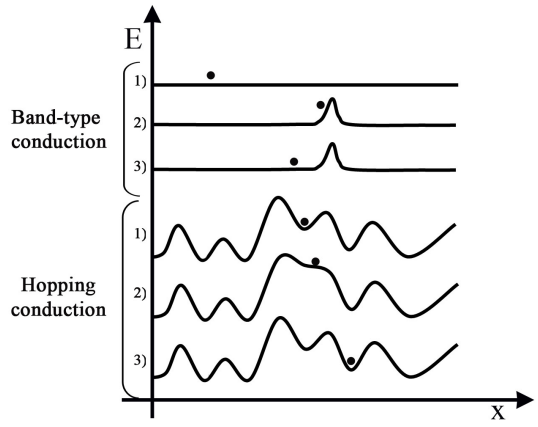

Figure 2.1.3 Comparison between band-like and hopping transport mechanisms in solids by representative plotting of energy versus displacement over the lattice. On the top, band-like conduction,

1) the free carrier is delocalized over the crystal structure, 2) phononic vibration occurs, 3) the charge carrier is scattered, i.e. his mobility is reduced. On the bottom, hopping-like conduction, 1) the charge carriers are localized, for example, in a defect side, 2) phononic vibration occurs, 3) the charge carrier can move to the following site. Figure adapted from ref.[6]

In general, the morphological defects have an influence on a material conductivity either by increasing it, acting as dopant on the system itself or by decreasing them, disrupting conjugation and transport. The most commonly occurring doping defects in polymers are solitons, polarons and bipolarons.[7,8]

A soliton is a non-dispersive topological defect due, for instance, to bond creation mismatching over polymerization. This particular defect has a high probability of occurring only when the polymer has a degenerate ground state. Once created it can delocalize over a certain number of carbon atoms. The dimerization confers to the electron high mobility. The soliton generates a new energetic level between valence and conduction bands.

When instead the polymer has a non-degenerate ground state solitons are normally non-stable. In this case polarons (single charged) and bipolarons (double charged) can be formed. These topological defects can be presented as the product of the bond between two solitons. The bond will cause the splitting in energy giving rise to bonding and antibonding states. From a chemical point of view, typical situation in conjugated polymers with no degenerate ground states, as in polythiophene, is to have two different forms named aromatic a quinonic. The two forms have different ground-level potential energies, i.e. the step between aromatic and quinonic forms, potentially allows charge confinement. The effect is a polymer backbone distortion, in order to minimize the effective charge over the carrier, together with generation of new energetic levels.[6]

The formation of these additional energy states, placed in the energy gap, changes the electronic and optical properties of the polymer (Figure 2.1.4).[9]

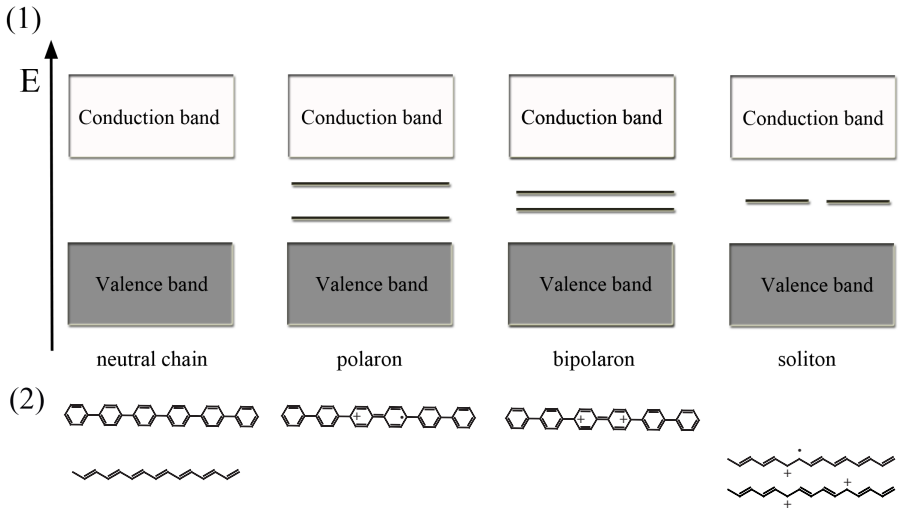

Figure 2.1.4 Energy levels alignment (1) and examples of representative structures (2) for the neutral chain of a polymer having non-degenerate ground state, poly(p-phenylene, and for a polymer having degenerate ground state, polyacetylene. Examples for the corresponding polaron, bipolaron and soliton structures are represented as well.

The overall transport in organic semiconductors can be, thus, explained considering the morphology of the solid, the contribution of band-like and hopping transport and the presence of additional charges as solitons, polarons and bipolarons.

An higher degree of complexity rises when considering the system from an intermolecular point of view. The pi-stacking between conjugated systems as well as the domains boundaries will play an important role. Being highly improbable, in macroscopic junctions, the presence of just one, fully conjugated, polymer chain, it becomes important to introduce models to describe the combination of intramolecular and intermoleculars factors.

2.1.3 Models of Charge transport in organic semiconductors

Three are the main theories that give a mathematical description of transport in organic semiconductors by giving a priority to the different contributions: the small polaron model, the multiple trap and release model and the variable range hopping model.

2.1.3.1 The small polaron model

The small polaron model[10,11] was proposed by Holstein in 1959 and modified to better describe the charge transport in a number of organic materials.

It is based on the formation of polarons when no degenerative ground-state is present, and the consequently generated additional energetic levels in the band-gap.

In this model the electron-electron interactions are neglected so considering a one-dimensional, one-electron transport. The tight-binding approximation is applied assuming that the effect of the potential energy variation is limited to the nearest neighbor sites. The small polaron model predicts band-like transport limited only by scattering when the charge transport occur at a T smaller than a critical one (T_c) and at higher temperature hopping between sites.[10,11] In this last case, the characteristic equations, *i.e.* total lattice energy (2.6), dispersion energy of the electronic flow (2.7), electron phonon coupling (2.8) and mobility (2.9) will be expressed by the following equations:

$$E_L = \sum_{n=1}^{N} \frac{1}{2M}\left(\frac{\hbar}{i}\frac{\partial}{\partial u_n}\right)^2 + \frac{1}{2}M\omega_0^2 u_n^2 \qquad (2.6)$$

$$E_k = E_0 - 2J\cos ka \qquad (2.7)$$

$$\varepsilon_n = -Au_n \qquad (2.8)$$

$$\mu = \sqrt{\frac{\pi}{2}}\frac{ea^2}{\hbar}\frac{J^2}{\sqrt{E_b}}(kT)^{-3/2}e^{-E_b/2kT} \qquad (2.9)$$

Where

N is the total number of the oscillators composing the system

ω_0 is the oscillation frequency, assuming it is the same for each oscillator

u_n is the displacement of the nth molecule

M is the reduced mass of each molecular site

J is the electron transfer energy

a is the lattice constant

A is a constant.

$\mu(0)$ is the mobility at 0 field

β is the Poole-Frenkel factor

F is the magnitude of the electric field

2.1.3.2 The multiple trap and release model

The multiple trap and release model gives an appropriate description of charge transport in ordered materials with thermal activated mobility. In this model is postulated the presence of a distribution of localized levels near the transport band edge, the so-called traps. A trap is a level outside the conduction band of the semiconductor normally due to defects or impurities.

The traps will accumulate with high winning ratio (close to 1), and release with a thermally activated process. The resulting mobility (2.10):

$$\mu_D = \mu_0 \alpha e^{-E_t/kT} \tag{2.10}$$

Where

μ_D is the drifting mobility

μ_0 is the mobility in the delocalized band

α is the ratio between number of states in the edge of the delocalized band and number of localized traps

E_t is the distance in energy between traps and delocalized band edges.

2.1.3.3 The Variable Range Hopping Model

The variable range hopping model, instead, proposed by Mott in 1979, instead considers one of the limits of the multiple trap and realized model, i.e. the spatial dependence of the charge transport. A charge has, in this model, the same probability of hopping to a more distant site or a higher energy level. It is a model best appropriate to describe charge transport in disordered materials. Another way to see it is as a trap mediated transport in which the traps are spread over the entire energy gap. Vissenberg and Matters in 1998 corrected the formulation modifying the probability, i.e. taking into account the elevated number of higher energy states. The final formulation will be Arrhenius-like.

2.2 Interfaces

When two materials characterized by a different electronic structure are placed in contact they interact at the interface, modifying their electronic structure in that region.

At a metal-metal junction the work functions of the two metals will couple and charge carriers will flow from one to the other in order to reach a minimum in the potential energy and thus equilibrium. The equilibrium is reached when the interfacial potential is equal to the differences between the work functions of the two metals (Figure 2.2.1).

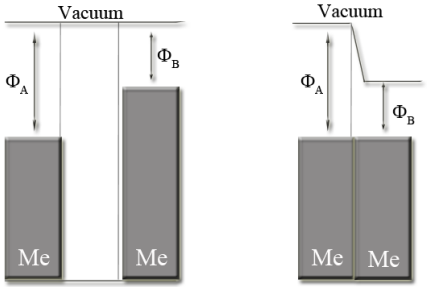

Figure 2.2.1 Schematic representation for the interface between two metals, on the left before forming a junction, on the right after the junction is formed.

In a Metal-Semiconductor junction, on the other hand, depending on the nature of the semiconductor, and on the difference in work function between the materials, two different level alignments might occur.

One of the possible approximations is the Schottky-Mott rule that states that the height of the barrier is equal to the difference between the metal work function and the electron affinity of the semiconductor (Figure 2.2.2).[12]

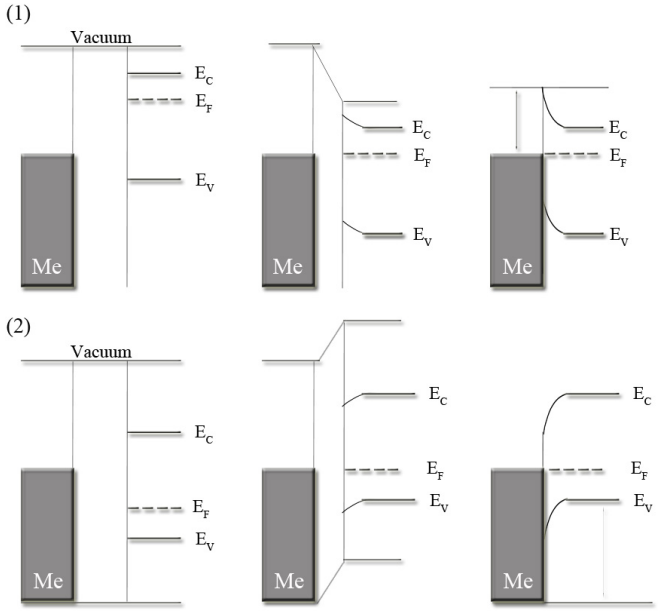

Figure 2.2.2 Level alignment processes for a junction formed by a metal with either p (1) or n (2) – type semiconductors, from left to right: change in the alignment by decreasing the distance between the two materials. Figure adapted from Ref.[13]

By application of a forward or reverse bias to the junction it is possible to tune the direction of transport and increase/decrease the charge carriers density.[13]

In recent years, the Schottky-Mott rule was shown to be an oversimplification since it doesn't take into account the interfacial electronic structure, such as dipole formation and so on, as demonstrated by experimental evidence.[14-16] Nevertheless the overall process holds qualitatively in most cases.

When instead three materials are placed in contact, two interfaces will be formed. One of the most studied cases for technological reasons is the metal-insulator-semiconductor junction. If the insulating layer is between 1 and 3 nm in thickness, a metal-insulator-semiconductor tunnel diode is formed, the device will be characterized by lower current, if compared with metal-semiconductor interfaces, and a non-equilibrium energy state for the semiconductor. Moreover the barrier height will be reduced and a potential will be formed over the interfacial oxide layer. When the thickness of the insulating layer increases, a metal-insulator-semiconductor capacitor will be formed (figure 2.2.3). In the ideal case the insulator has infinite resistivity and the formation of such a junction induces no charge formation in the dielectric but only on the semiconductor, and opposite in sign on the metal. For a p-semiconductor (n-semiconductor) the application of a small negative (positive) bias to

the metal doesn't perturb the Fermi energy of the semiconductor even if charges are allowed to "accumulate". The application of a positive (negative) bias, instead, allows bending of the bands "depleting" the major charge carriers of the semiconductor. By increasing the positive (negative) bias applied allows the minority carriers to be predominant at the surface and "inversion" to occur.[13]

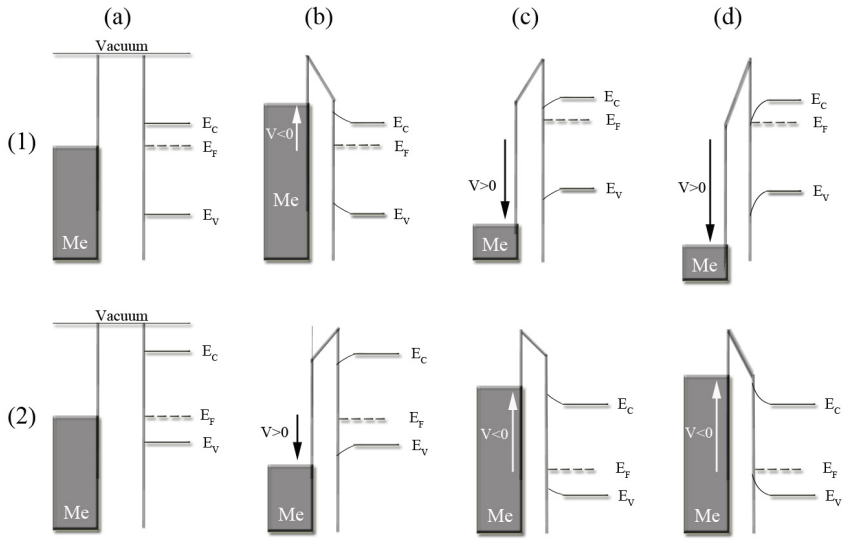

Figure 2.2.3 MIS bands for (1) a p-semiconductor and (2) a n-semiconductor. In (a) the equilibrium, (b) the accumulation, (c) the depletion and (d) the inversion regimes. The biases applied are presented as well. Figure adapted from Ref. [13]

2.2.1 Charge injection models and dependences

When a metal and a not/semi-conducting organic materials are brought close together, the probability of charge injection between the conductor and the semi or not conducting material rises.

The mechanism ruling the charge injection will depend on: the Fermi Energy of the metal, the HOMO or LUMO of the organic material, the presence of electronic and morphological defects, the temperature and the voltage applied and the morphology roughness of the interface. Since in the majority of the cases the metal Fermi energy doesn't match with the HOMO or LUMO levels of the molecule, a contact barrier could rise.

Hence, it is essential to consider the effect of the mismatch between the metal work function and the molecular orbital energies of the molecules and, the height and the thickness of the energetic barrier.

The main possible mechanisms are: direct and Fowler-Nordheim tunneling, thermoionic (Schottky) emission, Frenkel-Pool conduction and hopping (Figure 2.2.4).

	Direct tunneling	Fowler-Nordheim tunneling	Thermoionic emission	Frenkel-Pool conduction	Hopping conduction
Schematic band structure	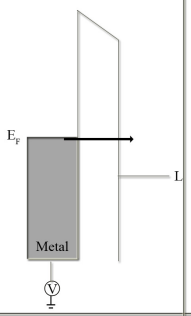	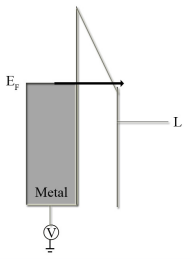	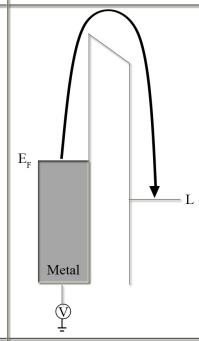	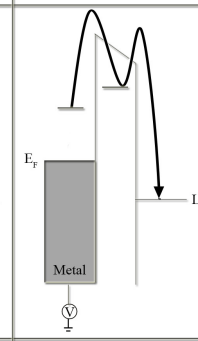	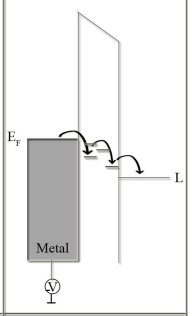
Temperature dependence	none	none	$\sim\frac{1}{T}$	$\sim\frac{1}{T}$	$\sim\frac{1}{T}$
BIas dependence	$\sim V$	$\sim\frac{1}{V}$	$\sim\sqrt{V}$	$\sim\sqrt{V}$	$\sim V$

Figure 2.2.4 Comparison between the main mechanisms of charge injection between a metal and a non-conductive or semiconductive material: a schematic of their band structure in which the process is highlighted is presented; the dependences of their conductivity from temperature and voltage applied are expressed as well. In the table: T is the temperature, V is the bias applied. [Table adapted from Ref.[13]]

2.2.1.1 Direct and Fowler-Nordheim tunneling

The direct tunneling is a quantum mechanical phenomenon. Due to their dual particle/wave nature, the electrons will have a probability higher than zero to overcome an energetic barrier. Fowler-Nordheim tunneling is a special case of direct tunneling, that becomes significant for high barrier thicknesses at high electric fields. Applying a high bias to the metal allows pinning of its work function until the limit in which the felt thickness is small enough to allow tunneling. Both these mechanisms are characterized by a weak temperature dependence of the conductance.

If the energy of the electrons after tunneling exponentially depends on the thichness of the barrier, the regime will be a non-resonant regime (Figure 2.2.5).

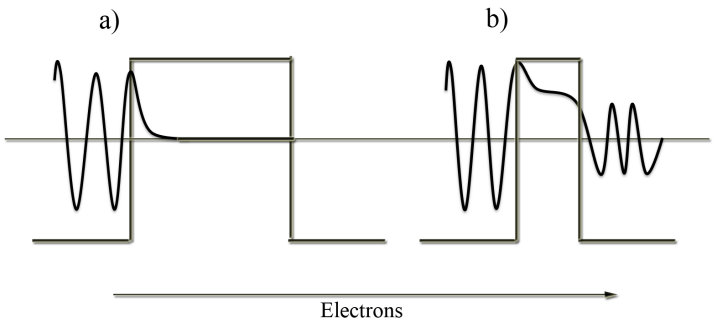

Figure 2.2.5 Typical non-resonant tunneling profile of the energy vs the thickness of the barrier. The electron transport direction follows the arrow. When the barrier thickness overcome a crytical value, no transport through the barrier is allowed a); while for smaller barriers, the transport is allowed but the energy of the elctrons after tunneling is lowed than before b).

Non-resonant direct tunneling represents one of the most common transport mechanisms in single molecule devices. At low bias, *i.e.* in the linear regime, the resistance in a nonresonant tunneling device can be expressed as (2.11):

$$R = R_0 e^{\beta d} , \qquad (2.11)$$

Where R_0 is the effective contact resistance, d is the barrier thichness (length of the molecule in single-molecule junctions) and β is the structure-dependent attenuation factor.

2.2.1.2 Thermoionic, Schottky and Frenkel-Pool emission

The thermoionic emission is the heat-induced flow of charge carriers between an heated electronic conductor and a non conducting space.

The electrons current density, for a thermoionic emission, can be expressed (2.12) as:

$$j = AT^2 e^{-e\phi_W / k_B T} \qquad (2.12)$$

where T is the absolute temperature, A is a constant, ϕ_W is the work function of the metal.

The thermoionic emission depends exponentially on the temperature. If no voltage is applied, a high temperature will be necessary to have a detectable current. Applying an external electric field, a pinning of the metal work function will occur allowing higher current density; this phenomenon is called Schottky emission. At high temperatures and low barrier heights it is likely to be the dominant mechanism.

The Pool-Frenkel conduction can be seen as a special case of the Schottky emission in presence of high density of traps. The resulting expression has, as the main difference if compared with the Schottky one, a lower barrier height that depends on the density of traps. This last mechanism becomes prevalent in presence of an high trap density.

2.2.1.3 Hopping

Hopping is a temperature dependent charge transport mechanism. The charges are localized and, if electron-phonon coupling is relatively weak, *i.e.* it is possible to neglect the polaronic transport, the carriers will hop in a regular array of available sites, randomly distributed in space. It is a phonon-assisted mechanism. Increasing the temperature, phonons will excite and help electrons to hop to available sites.

The characteristic equation is:

$$\sigma = \sigma_0 e^{\left(-T_0/T\right)^{\gamma}} \tag{2.13}$$

$$\gamma = \frac{1}{1+d} \tag{2.14}$$

in which d is the dimensionality of the system, for a 3D system $\gamma = 1/4$, giving Mott's law.[17]

When the organic material is thick, with low crystallinity and low density of thermally generated free-carriers, hopping becomes the prevalent mechanism.

2.3 Nanojunctions

A nanojunction is a junction involving nanoscale components, *i.e.* nanoscale electrodes with spacing between a few angstroms to a few nanometers. Nanojunctions are essential to obtain information on a material at the nanoscale and are normally utilized to get single molecule conductivities.

Three are the main methodologies to create nanojunctions, two of them can be considered *in situ* techniques while the third is *ex situ.* The *in situ* procedures are either based on the manipulation of nano-objects in order to place them in physical contact or in the growing of branched nanostructures synthetically.[18] Examples of *ex situ* nanojunctions are the mechanically controllable break junctions[19], e-beam prepared nano-gap electrodes[20], electromigration[21] or junctions created by SAM functionalization of a planar surface or a metallic nanoparticle measured by the nanoscale tips of a Scanning Tunneling Microscope (STM) or an Atomic Force one (AFM).[22]

2.3.1 Conduction in nanojunctions

When considering nanojunctions from an electronic standpoint, the main factors that need to be considered are: the charge transfer mechanism, the dependence on the temperature, staircase, and contact effects.

As a first approximation, to get insights into the processes involved, it is possible to consider a nanodevice with only one molecule in the gap and no defects.

Of the charge transfer mechanisms mentioned in section 2.2.1, in this nanodevice the predominants will be: thermoionic emission, direct tunneling, and defect-mediated transports. As both the thermoionic emission and the Pool-Frenkel conduction depend on temperature, working at lower temperatures the prevailing mechanism will be direct tunneling.

The temperature can essentially act in two ways, *i.e.* increasing the disorder in the system allowing competition between different mechanisms or by amplifying selectively phonon modes. The latter can also be caused by the bias applied. It is worth mentioning that, by increasing the bias applied in a nanojunction, an increase in the local temperature between the electrodes will arise causing molecular vibrations. The Current-Voltage (IV) characteristics will show a slight staircase effect, better

visible when plotting the first or second derivative in which every discontinuity is assignable to a phonon mode.[23,24] Another, and more pronounced, staircase behavior happens at low temperatures, in the case of single electron transport. In this case, the IV characteristics don't show a linear behavior but for certain, discrete, applied voltages. These energetic gaps are both due to Coulomb blockade and to size quantization effects. The first is due to the electrons' need of a critical bias amplitude in order to overcome the level displacement and allow conduction at low temperatures.

Below a critical temperature electrons need a bias high enough to overcome the level displacement, no conductance before the threshold bias is observed. The second is due to the possibility for electrons to occupy unoccupied orbitals, when this happens an additional energetic barrier will be shown.

Another factor that needs to be considered is the contact effect. Since at low temperatures, in the non-resonant tunneling regime, the resistance exponentially increases with the distance; having a covalent bond, an electrostatic interaction or no-contact between the electrodes and the molecule will show three apparently different conductivities. For instance the difference in contact resistance between a covalently bonded molecule and a non-covalently bonded gives typically higher values for the second, by one order of magnitude.[25,26] The contact resistance in any case doesn't only vary with the contact but with the metal work function and the tip bias applied when measuring with AFM or STM.

One of the biggest issues in nanojuction characterization is statistics and the time required for a single measurement. To overcome this issues the creation of a Self Assembled Monolayer (SAM) of molecules has been in most cases employed, being an easy technique that allows formation of an ordered single monolayer on the surface. Unfortunately, when working with SAMs some of the phenomena, such as the Coulomb blockade, are much harder to be observed. This has been attributed to the influence of the local environment around the junction.[27] Recently, nanojunctions allowing single molecule contact and statistics have been fabricated, a step forward over molecular characterization.[20,28]

2.4 Self-Assembled Monolayers (SAMs)

Surfaces have been described as a fourth state of matter for their unique properties that are highly dependent on the chemical and physical environment.

Bare metallic or metal oxide surfaces easily interact with organic molecules since the adsorbates lower the free energy of the interface between them and the ambient environment. Molecules adsorbed on a surface: alter interfacial properties, act as a physical or electrostatic barrier against aggregation, decrease the reactivity of the surface atoms,[29] modulate the metal work function[30] and control the wettability of the surface. The chemical adsorption of an ordered organic monolayer allows tuning of all the listed properties. However, being able to tune the properties at the surface means both understanding the surface and carefully choosing the molecules to adsorb. Self-assembled monolayers are organic, crystalline or semicrystalline, assemblies of molecules that spontaneously form a regular array on the surface.[29,31]

The self-assembly process can be easily described, from a bonding formation point of view, through the correlate Lennard-Jones potential.[32] In general, the process can be represented as in Figure 2.4.1.

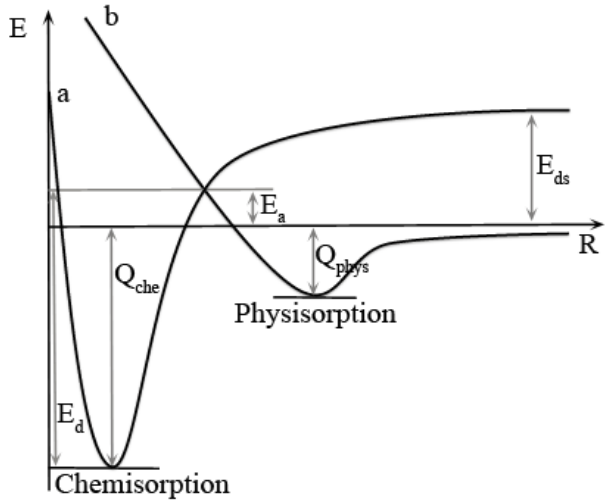

Figure 2.4.1 Lennard-Jones Potential description of the self-assembly process. a and b are respectively the potential energy curves associated to chemisorption and physisorption. Here Q = -ΔH, and represents the chemical or physical heat of absorption. E_a is the activation energy for the intercrossing between physisporption and chemisorption. E_{ds} is the dissociation energy.

The following steps can describe the general process.

When the molecule is approaching the surface at first physisorption takes place. The potential energy diagram associated with physisorption shows a shallow minimum at a relatively large distance from the surface, before the high increase in potential energy due to the strong repulsive forces resulted by electron density overlap.

In physisorption between no charged systems no barrier is present to prevent atoms of molecules to approach the surface: no activation energy is required and the kinetic is invariably fast. If the molecules are able to form a chemical bond with the substrate, a deeper minimum at smaller distances will appear, due to chemisorption. In this case the two potential energy curves shown in figure will linearly combine to a potential energy curve having all the displayed characteristics. The depth of the chemisorption potential well depends on the binding energy at the surface, whilst its distance from the surface represents the equilibrium distance for the adsorbed molecules on this surface. There is, of course a significant barrier for the reverse process. When considering the two processes, while the interaction energy in physisorption is in the order of 10-100 meV, in chemisorption is at least 5 times bigger and it anyway dramatically depend on the studied system. If the molecules need to dissociate before chemisorption to be able to create a bond, it is important to consider the dissociation energy (E_{ds}). The kinetics of SAM formation from a liquid solution is represented in Figure 2.4.2.

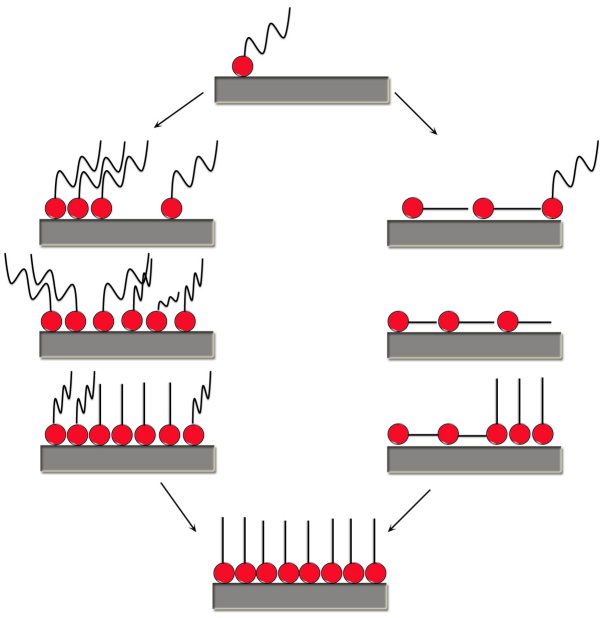

Figure 2.4.2 Cartoon of the typical sequences of SAM growth from a liquid. The intermediate phase can be disordered, lying down, etc. Adapted from ref.[33]

The process, as showed by the Lennard-Jones potentials, passes through a physisorption state (ordered or not) to then arrive to chemisorption first of small islands and then of the overall surface. In situ AFM images of growing SAMs have demonstrated a process based on initial island formation, then growth and creation of new islands, followed by an expanding step, finally the number of islands decreases due to the merging of neighboring islands.[34,35]

The final SAM has defects that depend on the structure of the underlayer substrate, as the crystalline structure of the metal, presence of vacancies and so on. Figure 2.4.3. shows a realistic example of a self assembled monolayer on a surface.

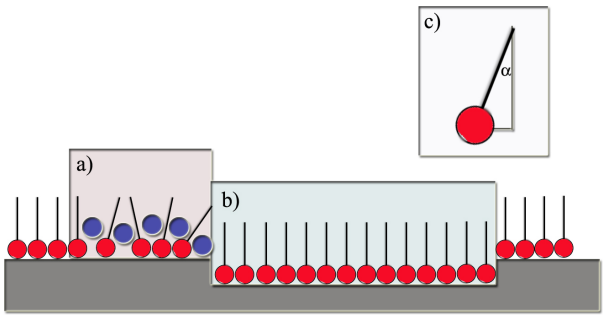

Figure 2.4.3 Representative image of a SAM structure and possible defects: a) non-regular self assembly due to impurities in the SAM or on the metal surface, b) defects due to the substrate morphology such as defects at gold grain boundaries and step edges, c) the realistic tilted angle formed by most SAMs on the surface.

When studying the SAM's growth from a solution, one should consider the concentration of the solution, solvent effects, chain length, adsorption energies, cleanliness of both the substrate and the solution, the crystal structure of the substrate and temperature.[29,31,33,36,37] A control over all the parameters needs to be achieved in order to obtain a SAM. As an example, a double logarithmic relation has been shown to exist between time constant and concentration needed to form a SAM.[33] The concentration versus time relationship was found anyway valid only until a certain value[38] that depends on the molecule. On the other hand, the chain length and composition have an effect on the barrier for the activation of the S-H bond.[39]

One of the most studied systems is the one involving the adsorption of alkanethiolate molecules on gold. In this case the resulting S-Au bond is very strong, i.e. an homolitic bond strength equal to 40 kcal/mol.[40] The process of bond formation is not properly understood yet, but an hypothesis consists in the following reaction[36]:

$$R - S - H + Au_n^0 \rightarrow R - S^- Au^+ \cdot Au_n^0 + \frac{1}{2} H_2 \qquad (2.15)$$

The process is highly probable if working in UHV conditions. On the other hand, when in solution, other competitive reactions can occur as, for example, oxidation to water is possible as well. Until now, anyway, no universal explanation has been formulated.

When adsorbing on gold, a thiolated SAM show a tilt angle respect to the surface that depend on composition and length of the tail of the molecule.

2.5 Nanoparticles

Nanoparticles can be defined as materials in which at least one dimension varies between 1 and 100 nm. Importantly, the properties of a certain chemical compound radically differ when it has nanoscale dimensions.

2.5.1 Physical properties of nanostructured materials

To derive a detailed description of the electronic structure in low-dimensional solids it is necessary to define the quantum confinement of charge carriers in a solid depending on its size. (Figure 2.5.1) Quantum confinement occurs if the wavelength of a particle in the system is comparable with the system's size. When this happens the system is best described by quantum mechanics and it is possible to obtain all the information about it by solving the associated Schrödinger's equation. Here, the confined carrier will behave as a particle in a potential box. The solutions of the Schrodinger equation will be standing waves having defined energetic values.

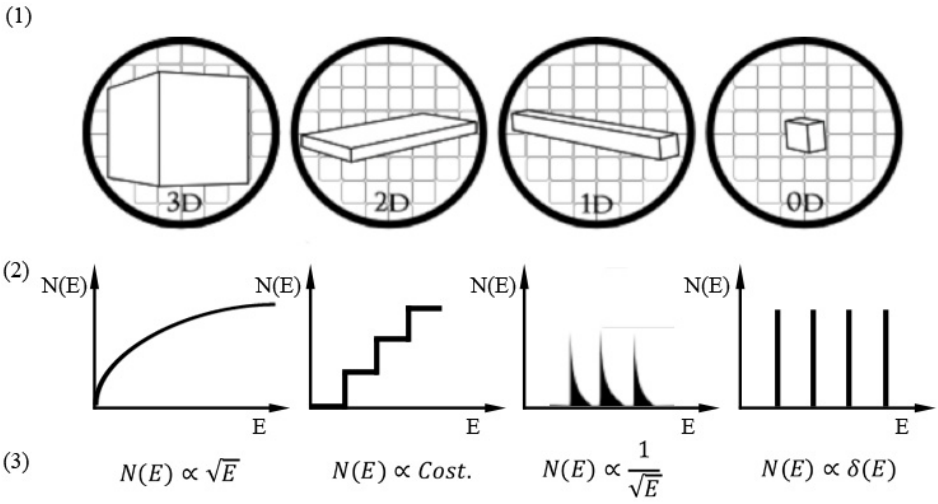

Figure 2.5.1 Representation of the quantum confinement effect on the distribution and density of the energetic levels depending on the size of the object: from left to right a 3D object characterized by no size-confinement; a 2D object characterized by size confinement in only one dimension; a 1D object characterized by size confinement in two dimensions and a 0D object in which the size confinement act in all three dimensions. A sketch of the object is first presented (1); then the behavior of the density of stated versus the energy (2) and the associated characteristic equation (3).

The strength of the effect of quantum confinement in a system doesn't depend only on its size but also on the electrical characteristics of the system as well, for instance whether it is a metal or a semiconductor.

In general, having discrete electronic levels allows evaluation of an average spacing between consecutive levels, called Kubo gap (δ). δ inversely varies with the number of atoms forming the cluster/nanoparticle (Equation 2.16).

$$\delta = \frac{E_F}{N} \tag{2.16}$$

where E_F is the Fermi Energy for the considered material and N the number of atoms composing the system. The energy levels will vary with the Kubo gap (Figure 2.5.2).

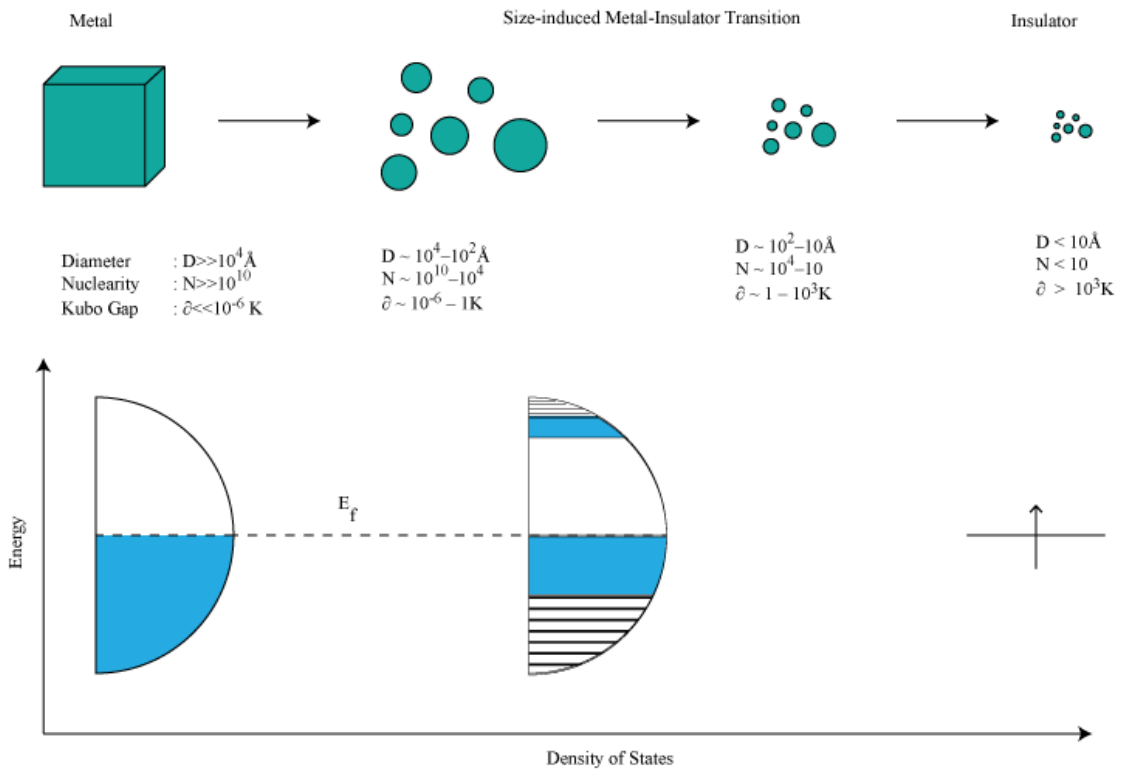

Figure 2.5.2 Variation of the levels varying the number of atoms. Adapted from reference[41].

2.5.2 The Surface Plasmon Resonance (SPR)

When overcoming the critical size for the quantum confinement to take place, and the material is a metal it is possible to have surface effects such as the surface plasmon resonance (SPR). Conducting quasi-particles confined on the interface between a

metal and an insulator are called surface plasmons. Their properties strongly depend on the properties of both the metal and the insulator.

When an incident radiation has a frequency resonant with the one of the surface plasmon states, it will induce a resonant oscillation, called surface plasmon resonance. If the metal is nanometer-sized the SPR will be localized and so called localized surface plasmon resonance.

The first theoretical rationalization was done by Mie[42] in 1908, he quantitatively described the resonances by solving Maxwell's equations for the systems.

The SPR, being an optical surface property will drastically depend on the refractive index of the embedding material as well as the presence of a SAM or any other coating layer on the surface. SPRs of many metals can be detected by UV-Vis spectroscopy, an absorption peak will appear at the wavelengths in resonance. Moreover, the interaction of two or more nanoparticles will produce a variation in the collective oscillation of the plasmons, *i.e.* in the SPR, modifying both the maximum absorption wavelength and the intensity of the UV-Vis spectrum.[43]

The mathematical dependences are can be written as presented in equations 2.17, 2.18, 2.19:

$$\sigma_{ext} = \frac{9V\epsilon_m^{3/2}\omega\epsilon_2(\omega)}{c\cdot(\epsilon_1(\omega)+2\epsilon_m)^2+\epsilon_2(\omega)^2} \quad (2.17)$$

$$C_{ext}(\lambda) = \frac{24\pi^2R^3\epsilon_m^{3/2}}{\lambda}\frac{\epsilon''(\lambda)}{(\epsilon'(\lambda)+2\epsilon_m)+\epsilon''(\lambda)^2} \quad (2.18)$$

$$\epsilon(\lambda) = \epsilon'(\lambda) + i\epsilon''(\lambda) \quad (2.19)$$

Where $C_{ext}(\lambda)$ is the energy losses in the direction of propagation of the incident light due to scattering and absorption, $\epsilon(\lambda)$ is the dielectric function of the metal, ϵ_m is the dielectric constant of the medium, R is the radius of the particle, $and\ \lambda$ is the wavelength of incident light.

2.5.3 In depth treatment of the physics and chemistry of gold nanoparticles (AuNPs)

When facing gold nanoparticles, it is first necessary to remind that bulk gold adopts a face centered cubic (fcc) crystal structure with the most thermodynamically stable surfaces being the (111) and (100). The lattice constant is 4.08 Å. The electronic structure is characterized by a wide sp band with a narrow d band and the Fermi level is situated just over the d band, the reason for its high electronic mobility.

2.5.3.1 Properties of gold nanoparticles

When lowering the dimensions, gold nanoparticles show a different morphology depending on the number of gold (N) atom forming the cluster. For an $N \leq 7$ the structure is planar, when reaching N = 20 a tetrahedron is formed. Then, for up to 100 gold atoms an icosahedric structure will be more stable, followed until 500 atoms by a decahedron. For even higher number of gold the fcc Wulff polyhedral takes over.[44-46]

Particularly stable are the gold nanocrystal formed by "magic numbers" of atoms that allow complete closure of successive shells in a cubic arrangement (shell 1=13 atoms, shell 2=55 atoms, shell 3 = 147 atoms, etc.).[47] Another way to see the "magic numbers" is related to the numbers of valence electrons in the cluster. Having the number of valence electrons in a cluster equal to (or approximately equal to) 2, 8, 18, 32, … means having filled the *s*, *p*, *d*, … orbitals of atoms, *i.e.* a particularly stable electronic situation.[48]

Quantum confinement effects are present in gold nanoparticles, with the critical size for metallic behavior being ~3nm. This also represents the critical size for SPR in gold nanostructured materials.

To avoid coalescence, when the nanoparticle size increases, stabilization methods need to be employed. The main two stabilization possibilities are electrostatic and steric. The electrostatic stabilization occurs when the coating layer has a dipole moment strong enough to be able to form an electrical double layer around the nanoparticles (or is charged). In this case it is not only the presence of a molecule on the surface but, most importantly, the electrical potential associated with the double layer, which through coulombic repulsion, avoids coalescence.

Nevertheless, a change in the dielectric constant of the solvent or adding other molecules can disrupt the coating layer, allowing particles agglomeration.

The steric stabilization occurs instead when a molecule or a polymer strongly acts as a surfactant, for instance creating stable bonds with the metal surface. In the field of the steric stabilization, the most well known technique is through adsorption of a SAM of molecules on the surface. In the Au case, due to the strong S-Au bond, one of the most employed techniques is through adsorption of a thiolated SAM as the nanoparticle's coating layer.

To evaluate the number of gold atoms and the number of coating molecules the easiest way is assuming the AuNP as a spherical object. In this case the characteristics of both the core and the surface can be calculated as presented in table 1.1

Amines and polymers represent alternatives to the thiol as nanoparticles surfactants.

Table1.1 Statistics for AuNPs.[49]

Au atomic volume	16.9×10^{-3} nm^3
Number of Au atoms in a spherical AuNP	$31d^3$
Number of thiols on the surface of a spherical AuNP	$14.7\ d^2$

2.5.3.2 Synthesis of gold nanoparticles

Numerous synthetic methodologies have been developed both at the solid, liquid and gas states. The most studied are the liquid phase ones since they allow better control over the different variables involved. Liquid phase synthesis has been achieved using a variety of methods, as thermolytic, sonolytic and photolytic procedures to decomposition of a metal precursor. The general process is based on the following steps: nucleation of single neutral atoms through collision and particle growth (influenced by concentration, stabilizing agent and solvent) until equilibrium.

The nucleation step mostly depends on the concentration of the neutral metal atom (derived by the ratio between precursor and reducing agent), on the surface energy of the corresponding metal and on the presence of a surfactant. The surface energy of a cluster depends on its size, decreasing the size the surface energy increase. There is, in fact a critical size for the nucleation process. The interfacial energy becomes one of the determining factors in the growth step as well.

The particle growth is based on two competing processes: attraction in order to minimize the superficial energy, towards size increasing, and diffusion, towards lower collisions and hence smaller probability of size increasing. Varying the relative concentrations of the precursors involved in the process it is possible to control these two factors. Late stages of nanoparticles' growth are subjected to Ostwald ripening, *i.e.* bigger particles grow from small particles coalescence on their surface. The Ostwald ripening is the main reason for the broad size distribution in nanoparticles' synthesis. The presence of a surfactant limits this process by stabilizing the nanoparticles and preventing their aggregation.

Heating a polydisperse solution of gold nanoparticles in presence of an excess of surfactant allows the, so-called, digestive ripening in which the bigger nanoparticles decrease in size while the smaller increase. Digestive ripening is a post-processing technique that allows control over the size distribution.

The most used technique for the synthesis of AuNPs is salt reduction in solution, in which a metal salt is reduced in presence of a surfactant.

2.5.3.3 Transport through gold nanoparticles and their role in devices[50]

Even if charge transport through nanoparticles is an evolving field, a number of phenomena have been discovered to be particularly interesting. The phenomena include tunneling, single electron charging, varying the wavefunction overlap, metal-insulator transition, non-Arrhenius behavior and electrochemical activity in general. A brief overview is presented here.

About tunneling, measurements of metal-molecule-NPs and in NP assemblies gave for the considered molecule a non-resonant tunneling decay factor, β, comparable with measurements done with macro electrodes, demonstrating the

possibility of having tunneling through a molecule when nanoparticles are involved even if the nanoparticles had sizes below the critical one.

Single electron charging is instead related to the possibility of nanoparticles charging (if smaller than the critical size) when an electron tunnels into them.

Below a critical temperature, electrons need a bias high enough to overcome the levels displacing, no conductance before the threshold bias is shown. This behavior is called Coulomb blockade. Increasing the temperature over a critical one, gives electrons enough energy to overcome the barrier and an Ohmic behavior in the current-voltage (IV) characteristics will then be observed. If more electrons are present, a multi-electron charging can occur giving a Coulomb staircase behavior (Figure 2.5.3)

Both these phenomena have been observed both on single-molecule junctions and in nanoparticle assemblies.

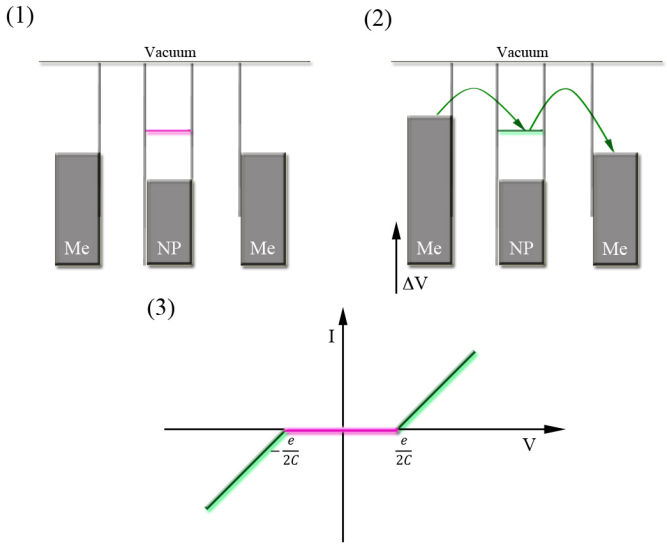

Figure 2.5.3 Single electron tunneling through a nanoparticle. No current can tunnel from the biased electrode to the nanoparticle (1) until a large enough bias applied allows tunneling then current is shown (2). The IV characteristics relative to the two regimes are presented as well (3). (In e/2C, C is the capacitance of the junction).

Higher-level delocalization occurs when the wave function between the nanoparticles becomes sufficiently strong. Decrease the inter-particles spacing, for instance, will allow increasing of the coupling between the nanoparticles. This process has been optically observed: well defined band structure via UV-Vis spectroscopy when the nanoparticles were well separated and instead continuous, broadband absorption was observed when the distance was lowered.

The transition between insulating and metallic behavior in nanoparticle assemblies can occur when the bandgap is small enough to allow conduction or by percolation through the nanoparticles network. If both these phenomena are satisfied, metallic behavior will occur. Nevertheless, conduction of nanoparticle assemblies is always lower if compared to the bulk metal material.

Finally, nanoparticles can show non-Arrhenius behavior. The relationship between conductance and temperature can be expressed ad in equation 2.20.

$$\sigma \approx e^{-\left({}^{T_0}/_{T}\right)^{\upsilon}} \qquad (2.20)$$

Where υ can assume values between 0 and 1. If the value is 1, the assembly shows an Arrhenius behavior. It has been frequently shown in nanoparticle assemblies a υ equal to ½.[50]

To explain this behavior various models have been used as the VRH (variable range hopping model) co-tunneling, quasi-localized hopping and network of random resistances. The VRH model holds theoretically but becomes quite unrealistic under experimentally observed conditions. The prediction of having a sufficiently large hopping distance to allow tunneling over a certain number of grains, for instance, doesn't consider the rapid decay of the wave-function in insulating media. To allow this long-range process to occur a possibility is a co-tunneling mechanism in which while an electron tunnels to the nanoparticle, another one tunnels away from it. The co-tunneling can be elastic or inelastic, meaning that the energy to tunnel in will be the same or different respectively than the one to tunnel out (Figure 2.5.4).

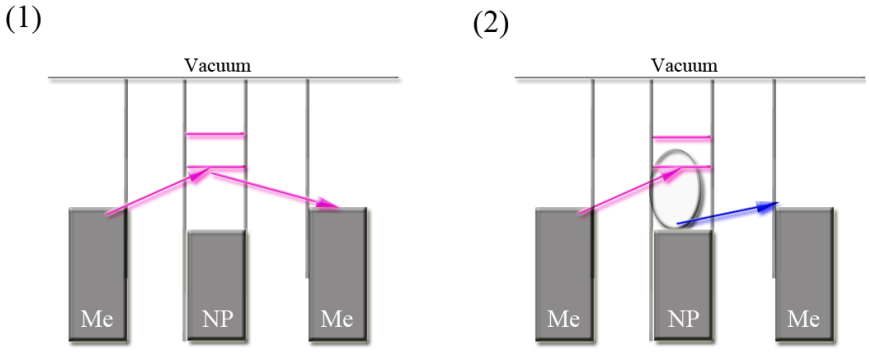

Figure 2.5.4 Co-tunneling mechanisms, elastic (1) and inelastic (2). Adapted from Ref.[50]

Another proposed mechanism is the quasi-localized hopping in which the energy barrier to extract an electron from a metal cluster as well as the scattering due to defects on the NPs are taken into account. Two competing parameters are involved in the charge transfer: a cluster charging energy barrier, that is inversely proportional to the cluster size and an exponential drop of the conductance with the cluster size.

Another way to model the non-Arrhenius behavior is to imagine a nanoparticles assembly as a network of random resistances. The resistance between two nanoparticles will be dependent on the separation between them as well as on the activation energy for the transfer to occur.

Nevertheless, even if no single conduction theory for single nanoparticles and nanoparticle assemblies has been formulated, most of the phenomena visible in these junctions are describable by one or a combination of the theories here presented.

2.6 Organic Field-Effect Transistors (OFETs)

An OFET is a three terminal device in which the current between two of the terminals is tuned by the third one and, at least one between dielectric and semiconductor is an organic molecule/polymer. In order to focus the attention on the working principles, an OFET can be compared to a capacitor. Under this prospective, one of the plates is a conducting channel between two Ohmic contacts, and the other plate of the capacitor can be used to generate charges, tuning the current.[51] (Figure 2.6.1)

The two electrodes having Ohmic contact are called Source and Drain while the second plate of the capacitor, used to generate charges is called Gate.

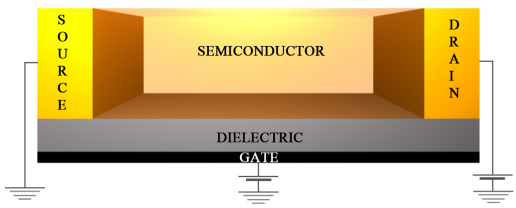

Figure 2.6.1 Sketch of an OFET.

Upon application of a bias through the gate electrode charges are generated at the semiconductor/dielectric interface and the channel is created (see accumulation

regime in MIS interfaces paragraph 2.3). The application of a bias between source and drain, grounded electrodes, allows the motion of the charges inside the channel, therefore permitting the determination of the amount of charges and their mobilities through the channel. In an organic semiconductor not all the charges are necessarily generated by the bias; the contribution of thermally generated ones is non-trascurable, consequently, a current when the device is in off-state can be measured. As in capacitors, the number of generated charges will directly depend on the bias applied through the gate.

A notable difference between OFETs and the inorganic counterparts (FET) is that FET operates in inversion regime; being aware of such approximation the devices equations derived for inorganic systems can be applied to OFETs as well, and will be discussed in Chapter 3.

Four main configurations (Figure 2.6.2) are used with OFETs. The gate and the electrodes, in fact, can be deposited on top or on the bottom respect to the semiconductor, always keeping the capacitor characteristics of the device.

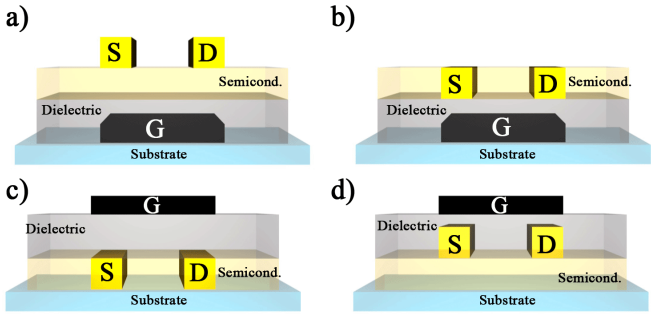

Figure 2.6.2 Possible OFETs geometries: a) top contact-bottom gate, b) bottom contact-bottom gate, c) bottom contact-top gate and d) top contact-top gate.

The choice of the geometry directly depends on the materials used. If the aim is studying the semiconductor's properties, the use of bottom gate inorganic Si^{n++}/SiO_2 is a common choice, being commercially available with high quality. Another possibility is the use of organic dielectric in the top gate configuration, since carefully choosing the system it is possible to deposit the dielectric without destroying the underlying semiconductor. Choosing an n, p or an ambipolar semiconductor will affect the behavior of the device (Figure 2.6.3) when a bias is applied.

The case of ambipolar semiconductor is slightly more complicate, because it's behavior depends on the sign of the voltage applied. It will, in fact, work as a p-type under negative bias, and as an n-type when positive bias is applied.

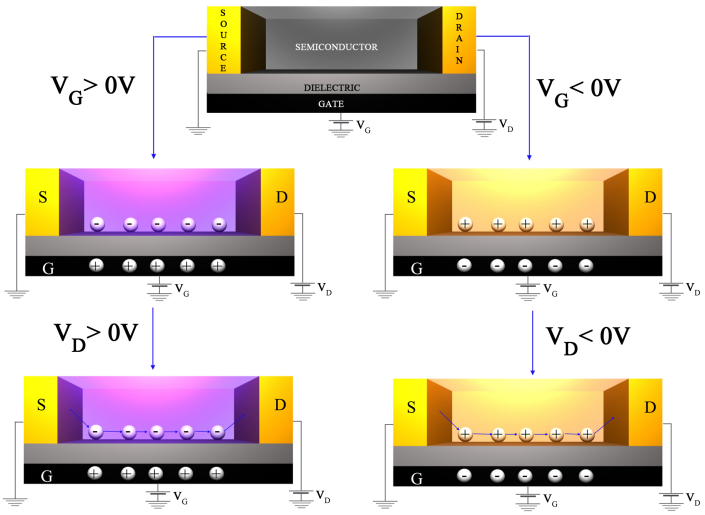

Figure 2.6.3 Operating-mode for an n or p semiconductor. On the left, n-type: a positive voltage through the gate generates negative charges in the channel. The application of a higher positive bias between the contacts will allow charge transport in the channel. On the right side, a p-type semiconductor. Both the generation of (positive) charges and the charge transport will be controlled by application of a negative voltage.

The main three characteristics of an OFET are the threshold voltage, the charge carrier mobility and the ON/OFF current ratio in the channel.

The threshold voltage represents the lowest voltage to apply to induce a current in the channel, whereas the charge carrier mobility can be defined as moving rate of the charge carriers when a bias is applied; finally, the ON/OFF current ratio is a measure of the sensitivity of the device to the applied bias.

When using organic materials instead of inorganic ones it is important to understand which factors will influence the behavior of the devices.

From a semiconductor point of view, not only the accessibility of HOMO (or LUMO) by the metal when a voltage is applied, the overlap of the frontier orbitals, the purity of the material (impurities act as charge traps) will play a role, but also the crystallinity and in general the organization of the molecules one respect to the others:[52] to higher crystallinity, usually corresponds a better overlapping between molecular orbitals, therefore, often a better charge transport.

The choice of the dielectric too, has extreme importance, since it affects the charge induced in the semiconductor: charges will be directly proportional to the permittivity of free space of the material, the area, the voltage applied, and inversely proportional to the distance between the electrodes. It is possible to reduce the voltage

needed to generate charges in the semiconductor by either increasing the dielectric constant or reducing the thickness. Clearly, the thickness of a dielectric can be decreased only until a certain value; below such threshold the charges will be able to tunnel through the material and leakage will be shown. A complementary approach is to change the dielectric by employing a material having higher dielectric constant, for example organic molecules or polymers. In this case, again the morphology of the film plays an important role, but, the higher the disorder, the higher is the effective dielectric constant.[19,53]

In general, due to the geometry and working characteristics of OFETs, the charge transport will be highly influenced by the optimization of two interfaces: contacts/ semiconductor, in order to increase the charge injection, and semiconductor/dielectrics, to increase the charge transport through the device.[54]

In the contacts/semiconductor interface, two are the main factors playing a role: the morphology and the coupling of the electronic structures of metal and semiconductor.

In a transistor, being the channel length much bigger than the contact area is morphology the prevalent factor. Accordingly, top contact devices have been shown to perform better in term of threshold voltage and mobility than the bottom contact counterpart.[55] To decrease the contact resistance one of the most used methods is through chemical adsorption of a SAM on the surface. Careful choice of the SAM allows to simultaneously tuning the interface morphology, by varying the hydrophobicity of the surface, and its electronics by varying the metal work function.[56]

Being the first nanometers over the semiconductor/dielectric interface the ones that mostly participate in the charge transport, the organization of the molecules on the surface play again a relevant role; it is necessary to tune the surface pursuing the best packing of the semiconductor.[57] Adsorbing a SAM on the dielectric surface can as well help the organization of the semiconductor in the channel and minimize the effects of the surface defects on the charge carriers transport in the channel.

A particular case is represented by multi-functional transistors, in which the properties of the materials composing them allow tuning of the devices performances responding to external stimuli. In this way novel typologies of sensors, switches and memories can be fabricated. These devices show the same dependences from the

interfaces, the work functions and the morphologies of the not-multifunctional ones but their electrical properties can be tuned through external stimuli as well.

2.7 Organic photochromic systems and azobenzenes

Organic photochromic systems are molecular structures, either molecules or polymers, able to react to an incident electromagnetic radiation by changing their molecular structure[58,59] and/or their shape[60,61] and/or their physico-chemical properties.[62]

The science that studies the behavior of such systems is the organic photochemistry and deals with the processes involved when light interact with organic molecules/polymers changing their physical properties. This is done by studying the structures, energies and dynamics of the reagents, intermediate states (when present) and products. All the physical parameters involved in chemical reactions, as temperature, pressure, physical state of the reagents, etc. will play a role in these systems as well, and they hence need to be considered.[63]

Nevertheless, having the possibility of dealing with molecules that undergo a well defined change under specific, and easy to achieve, conditions opens new ways to downscale devices. Particularly interesting from both a scientific and technological point of view are molecules able to switch and/or to perform a molecular motion when subjected to an external stimulus.

If the reaction is reversible, it is moreover possible to actually employ such systems as light-mediated switches between two physically different states. Evaluating the practical efficiency, *i.e.* the photostationary state, of the transition becomes, then, one of the key concepts. Where the photostationary state represents a steady state between the species involved in the case in which light have been adsorbed by at least one of them.

One of these systems is the azobenzene. Azobenzenes are diazene derivatives bearing two phenyl rings as substituents of the hydrogens. They are well known photochromic systems. They are able to undergo reversible photoisomerization between a *trans* (E) and a *cis* (Z) forms. This photoisomerization occur by irradiation in the UV spectral region when isomerizing from *trans* to *cis* and in the visible one for the back reaction. Normally, the *cis* form is less stable than the t*rans* and the

reversible reaction can also take place by thermal relaxation. From a spectroscopic point of view, the two states present different UV-Vis, Raman, IR, ^{1}H-NMR spectra.

The photoisomerization mechanisms in these systems have been proposed to occur mainly through: rotation, inversion, concerted inversion and inversion-assisted rotation. The prevalent mechanism, the yield of photoisomerization, the precise wavelengths of irradiation and the rate of each forward and back reactions depends drastically on the substituents, on the temperature, on the physical state of the system and if in solution, on the solvent.[64]

The particular molecule studied in this thesis is an acetylated thiol biphenyl azobenzene (AZO) (Figure 2.7.1).

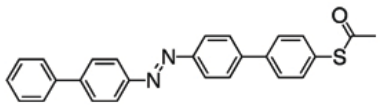

Figure 2.7.1 Chemical formula of [(1,1'-byphenyl)-4-yl]diazene, *i.e.* AZO.

The thiolated, not acetylated, form of the AZO molecule has been the subject of numerous studies from our group and others. The main characteristics are, when in a $CHCl_3$ solution, a maximum absorption for the *trans* form at 370 nm and for the *cis* at 450 nm. The isomerization process is not complete; the forward reaction allows isomerization of AZO until a maximum of 84±6% of the *cis* form. The kinetic constant of the reverse reaction in solution was estimated to be $8.55\times10^{-4} \pm 0.30\times10^{-4}$ s^{-1}.[65] When adsorbed as mono-component SAM on gold it showed higher yield of the reaction with an estimation of maximum 94±6% of *cis* isomer after irradiation and roughly four times smaller kinetic constant for the reverse isomerization, *i.e.* $2.21\times10^{-4} \pm 0.05\times10^{-4}$ s^{-1}.

The STM characterization of the surface revealed a tightly packed assembly of the AZO molecules on the surface both just after absorption in dark, as *trans* isomers, and after irradiation, hence after isomerization to the *cis* state. The STM features showed different profiles for the two isomers, compatible with the two isomers.[65,66] It is particularly interesting to notice that this is the first documented case of azobenzene isomerization in a tightly packed mono-component SAM. To allow isomerization, that is bending at the N=N double bond, a high degree of freedom is necessary. When an azobenzene is chemisorbed as SAM on the surface in its *trans* configuration, it is likely to form a packed self-assembly, in which the system does not have enough

degrees of freedom to isomerize to the *cis* form. To explain this particular behavior of AZO, has been proposed a cooperative and unidirectional isomerization mechanism based on the pi-stacking between the azobenzene moieties.[66] Theoretical calculations based on the structure of the molecule in the gas phase and on experimental STM images predict the angle between the two biphenyls in a molecule equal to 82° when in gas phase and 117°.[56] This result is in accordance with the lost degree of freedom for the bending when the molecule form a tightly packed SAM on gold.

The AZO SAMs have also been embedded in vertical nanojunctions formed with Hg-drop electrodes[67] and conductive-AFM[68] in order to estimate the β factor for nonresonant tunneling. The extracted values were respectively $0.5\pm0.1 Å^{-1}$ and $0.45\pm0.10 Å^{-1}$, essentially no difference was revealed even if the dimension of the nanojunction was markedly greater in the first case. In the Hg-drop case another unexpected property was revealed: reversible isomerization within the active contact region of the Hg-drop. This means that the AZO SAM was able to lift a cargo. Calculations of the contact force for unit/area revealed a total equal to at least 1.0×10^5 Nm^{-2}.

The photoinduced work function changes of gold surface featuring AZO SAM undergoing isomerization have been monitored via kelvin probe, kelvin probe microscopy, ultraviolet photoelectron spectroscopy, and electroabsorption. Theoretical predictions have also been exploited in order to get an in depth understanding of the system. Experimental results showed a variation equal to 70–125 meV.[56]

Eventually the SAM was utilized to photo-modulate the change injection in an OFET. A variation in current of roughly 20% was achieved over irradiation. This variation was accompanied by a variation in V_{TH} due to the tuned contact resistance.[69]

2.8 Generalities on Molecular Spectroscopy

The molecular spectroscopy is the science that studies the interactions light-matter to get structural information on the molecular systems.

In first instance, to understand molecular spectroscopy it is necessary to understand both the properties of the electromagnetic radiation and of the matter. Maxwell's electromagnetic theory defines the electromagnetic radiation as a radiating energy propagating in the space as sinusoidal wave, propagating in a direction normal to the electric and magnetic field.

Assuming the wave/particle duality of the electromagnetic radiation, the generalization of the quantic theory allowed definition of quantization for every microscopic physical system. A system's energy variation is allowed, following, only between two defined energetic levels characterized by two different quanta's numbers.

Considering a two levels system (Figure 2.8.1) one can assume to have a system prepared with energy equal to the level E_1. It is then possible to promote the system to the level E_2 increasing its energy of an amount equals to the difference E_2-E_1.

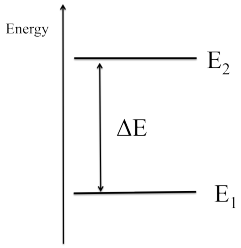

Figure 2.8.1 Schematic representation of a 2 energetic levels system.

$$E = h\nu \tag{2.20}$$

$$\Delta E = E_2 - E_1 \tag{2.21}$$

$$\nu = \frac{(E_2 - E_1)}{h} \tag{2.22}$$

A way to provide that energy is through an electromagnetic radiation that will couple with the molecular system and exchange energy.

Irradiating the example system with a large frequency range of electromagnetic waves, *e.g.* white light, and measuring all the frequency transmitted through the sample, an Absorbance spectrum is acquired, and a decreasing of intensity for the frequency $(E_2-E_1)/h$ will be observed.

If the system were prepared in the higher energy state, the coupling with the radiation will promote the emission of energy, allowing to record an emission spectrum.

If we consider systems such as atoms, or molecules, the energy required for an electronic or nuclear spin inversion is much higher than the one required to rotate a molecule, which is higher than the one required to promote chemical bonds stretching, or bending of molecular angles. Even higher is the energy generally required to promote an electron to an excited electronic state.

The rules that describe which material system interacts with the light, are the selection rules and are dependent on the symmetry of the eigenfunctions (by extension riconducible to the atomic and molecular orbitals), and on the frequency and polarization of the incident electromagnetic radiation considered.

A molecule can be defined as a stable aggregate of nuclei and electrons. This system has multiple degrees of freedom, therefore, to first approximation, neglecting any external potentials, its Hamiltonian will be composed by term relative to:

- Translational movement (movement of a molecule as a single object, barycenter motion)
- Rotational (rigid motion of the molecule as a single object without displacement of the barycenter)
- Vibrational (oscillation of atoms around the equilibrium position without movement of the barycenter)
- Electrons-nuclei interactions.

Except the translational movements (that can be separated from the others), all the others terms will interact one with the other, making really complex the dynamic study of a molecule. The adoption of an approximation such as Born-Oppenheimer, allows the nuclear and electronic motions to be separated, simplifying the analysis.

2.8.1 UV-Vis Spectroscopy

Is the spectroscopy that studies the electronic transitions within a molecule. The wavelengths of the radiation, which generally activate these transitions ranges in the hundreds of nanometers, i.e. 200-800nm. .

The electronic transitions can be treated according to the molecular orbital theory. Each transition has in fact enough energy to promote one or more electrons from either a bonding or non-bonding (n) molecular orbital to an antibonding one. Considering two bonding possibilities, i.e. σ and π, it is possible to have (Figure 2.8.2):

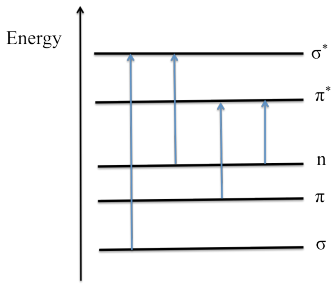

Figure 2.8.2 Schematic level's representation of the possible electronic transitions.

Where in figure:

$\sigma \rightarrow \sigma^*$ represents the promotion of an electron from the σ bonding state to the σ^* antibonding state.

$n \rightarrow \sigma^*$ represents the promotion of a non-bonding electron to an antibonding state

$\pi \rightarrow \pi^*$ represents the promotion of a pi-electron to the pi-antibonding state

$n \rightarrow \pi^*$ represents the promotion of a non-bonding electron to an antibonding state

Being every vibrational level degenerate in a certain number of rotational levels and not being any of those level selection rules forbidden it is possible to have excitation to all the level physically possible in the roto-vibrational spectrum (Figure 2.8.3). This is one of the aspects that justify the typical appearance of UV-Vis absorption spectra, which usually shows broad features, therefore called bands.

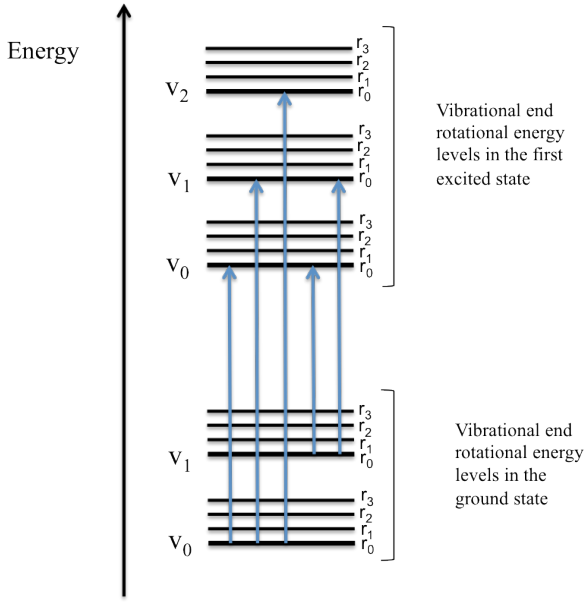

Figure 2.8.3 Schematic representation of rotovibrational modes

2.8.2 Raman Spectroscopy

When an electromagnetic radiation meets a molecule the light is in part transmitted, in part reflected and in part scattered. The photons can be scattered elastically or inelastically. Using a high-intensity, monochromatic radiation (as a LASER) it is possible to observe whether the photons are scattered elastically (providing exactly the same electromagnetic radiation) or before interact with the material and are then be emitted with an higher (anti-Stokes) or lower (Stokes) energy.[70]

According to the quantum theory and considering a radiation having frequency υ constituted by photons having energy hν it is possible to explain the Raman Effect. The photons will collide with the molecule. If the collision is perfectly elastic the photons will be reflected and collected by a detector. If instead an energy exchange between the electromagnetic light and the molecule happens, the collision is called inelastic. The molecules are able to increase or decrease their energy only according with the quantic theory. This means that the difference in energy between the emitted radiation and the detected one will equal the difference between two states of the molecule. The molecular modes that are active in the particular spectral range considered are the vibrations and rotations.

According to the classical theory instead, a molecule subjected to a static electric field will undergo deformation due to the different polarities of nucleus and electrons. A dipole moment will be induced and the molecule will be polarized.
The induced dipole moment depends on the intensity of the applied electric field and on the polarizzability of the considered molecule.

$$\mu = \alpha \mathrm{E} \tag{2.23}$$

When a molecule is subjected to a radiation having frequency ν, the incoming electric field will vary according to:

$$E = E_0 \sin 2\pi\nu\, t \tag{2.24}$$

This induced dipole will produce oscillations having frequency ν

$$\mu = \alpha \mathrm{E} = \alpha E_0 \sin 2\pi\nu\, t \tag{2.25}$$

In this way an oscillating dipole will emit a radiation having the same frequency of the radiation. This is the expression for the Rayleigh diffusion.
If vibrations or rotations get moved by the radiation the polarizzability will be altered by the radiation and a oscillating dipole will be created.

The effect of the vibrations is underlined here:

$$\alpha = \alpha_0 + \beta \sin 2\pi\nu_{vib}\, t \tag{2.26}$$

$$\mu = \alpha \mathrm{E} = (\alpha_0 + \beta \sin 2\pi\nu_{vib}\, t) E_0 \sin 2\pi\nu\, t \tag{2.27}$$

$$\mu = \alpha_0 E_0 \sin 2\pi\nu\, t + \tfrac{1}{2}\beta E_0 [\cos 2\pi(\nu - \nu_{vib})t - \cos 2\pi(\nu + \nu_{vib})t] \tag{2.28}$$

giving a Raman Shift equal to ν_{vib} in the case of a diatomic molecule.
The effect of rotations instead:

$$\alpha = \alpha_0 + \beta' \sin 2\pi(2\nu_{rot})\, t \qquad (2.29)$$

where $2\nu_{rot}$ has been used due to the intrinsic symmetry of the rotational operation. Substituting:

$$\mu = \alpha_0 E_0 \sin 2\pi\nu\, t + \beta' E_0 \sin 2\pi\upsilon t \sin 4\pi\upsilon_{rot}\, t \qquad (2.30)$$

$$\mu = \alpha_0 E_0 \sin 2\pi\nu\, t + \frac{1}{2}\beta' E_0[\cos 2\pi(\nu - 2\nu_{rot})t - \cos 2\pi(\nu + 2\nu_{rot})t] \qquad (2.31)$$

giving a Raman Shift equal to $2\nu_{rot}$ in the case of a diatomic molecule.
Moreover, if both β and β′ are equal to zero, the molecules doesn't polarize and the dipole oscillates only at the frequence of the incident radiation, i.e. the molecule isn't Raman active.
These are the equations for stokes and antistokes radiations. (Figure 2.8.4)

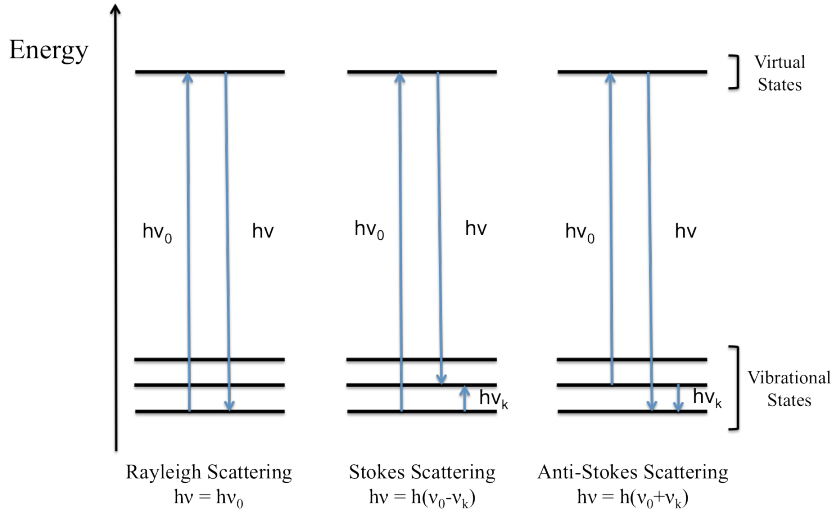

Figure 2.8.4 Representative energetic levels for Rayleigh, Stokes and Anti-Stokes scatterings.

The Raman technique is a particularly interesting since the intensity approximately scales as λ^4 and the spectrum is, as for infrared spectroscopy, dependent on the molecular symmetry. By defining the symmetry group for the studied molecules it possible to define which modes will be IR and which ones Raman active. In general, when the symmetry of a particular mode corresponds to a fundamental transition that

mode will be IR active, when corresponding to a product of two fundamental transitions will be Raman active.

2.8.3 Surface enhanced Raman Spectroscopy (SERS)

The Surface Enhanced Raman effect was firstly discovered in 1974 by Martin Fleischmann and co-workers as an unexpectedly strong Raman signal registered for pyridine adsorbed on rough silver electrodes.[71]

The SERS Spectroscopy became particularly studied because of the discoveries of an enhancement equal to 14 orders of magnitude allowing single-molecule detection.

A large number of books and reviews report the specifics of this particular effect.[72-75]

The power of the Raman signal in SERS can be expressed as:

$$P_{SERS} \propto (\mu_{ind})^2 \tag{2.32}$$

$$\mu_{ind} = \alpha \cdot E_0 \tag{2.33}$$

and, more specifically:

$$P_{SERS} \propto N \cdot I_L \cdot |A(\nu_L)|^2 \cdot |A(\nu_S)|^2 \cdot \sigma_{ads}^R \tag{2.34}$$

where:

P_{SERS} , Power of the Raman signal

μ_{ind}, Induced dipole moment

N, Number of molecules

I_L, Laser intensity

$A(\nu_L)$, Magnification of the laser-excitation

$A(\nu_S)$, Magnification of the scattered fields

σ_{ads}^R, Effective Raman cross section of the adsorbed molecules

No complete understanding of the SERS mechanism has been yet achieved even

if theoretical model to describe and understand the experimental results have been created. There are mainly two ways to explain the SERS enhancement: the electromagnetic enhancement and the electronic or chemical enhancement. Electromagnetic enhancement is the field enhancement due to the surface plasmon resonance (SPR) in the metal, which are able to resonantly interact with the incident radiation. When the laser light couples in a resonant way with the SPR of the metal an enhancement of the local electromagnetic field will take place via radiation from the metal of its own dipolar field E_{sp}. The magnitude of E_{sp} felt bye nearby molecule depends on the metal's sphere radius, the distance (d) from the molecule considered, the metal dielectric constant ε and the incident electric field's intensity E_0.

$$E_{\text{sp}} = \frac{\varepsilon - \varepsilon_0}{\varepsilon + 2\varepsilon_0}\left(\frac{r}{r+d}\right)^3 E_0 \qquad (2.35)$$

Naming the total field felt by the considered molecule E_M, we'll have:

$$E_M = E_0 + E_{sp} \qquad (2.36)$$

and the normalized field enhancement:

$$A(\nu) = \frac{E_M}{E_0} \qquad (2.37)$$

Experimentally, the field enhancement depends on the type of metal and its roughness, the shapes of the cluster formed on the surface and the incident light. In particular the signal increase when decreasing the nanoparticles sizes.

Highest enhancement was found when both laser and scattered fields are in resonance with the SPR.

The second way relies on electronic or chemical enhancement. It has been found that some molecules give higher enhancement compared with others.

The presence of a metal can shift and broadens the existing electronic levels of a molecule adsorbed on its surface and in some cases induce creation of new levels also altering the polarization of the molecules.

One of the models proposed to explain the different enhancement given by different molecules on an identical surface is based on ballistic electrons and holes. These electrons and holes are excited in the metal and couple with the electrons of the molecule. According to the model these ballistic electrons can tunnel to the LOMO of the adsorbed molecule. When the electron returns to its initial state in the metal emits a Raman shifted proton.

From an experimental point of view, the factors that need to be considered when doing a SERS experiments are: the polarization and size of the studied molecules, the possible shift in the electronic levels by adsorption on a metal surface, the distance between the nanoparticles considered, their size, the metal they are composed of, and the SERS wavelength dependence.

$A(\nu)$ can be experimentally measured, considering:

$$A(\nu) = \frac{(I_{SERS}/N_{surf})}{(I_{NRS}/N_{vol})} \tag{2.38}$$

where

I_{SERS}, Surface enhanced Raman scattering intensity

N_{surf}, Number of molecule bounded to the metallic surface

I_{NRS}, Normal Raman intensity

N_{vol}, Number of molecules in the excitation volume

Another important factor that needs to be considered is the dependence on the distance. The field enhancement around a small metal sphere decays with r^{-3}, assuming the E^4 approximation of the Raman signal and the increased surface area, that approximately scales with r^2, therefore the global field enhancement should scale as r^{-10}.

2.9 Atomic force microscopy (AFM)

It is part of the family of the scanning probe microscopies (SPM) together with the scanning tunneling microscopy (STM), the kelvin-probe force microscopy (KPFM) and the scanning near-field optical microscopy (SNOM).

These techniques enable direct correlation of physico-chemical properties with the composition and morphology of the surface. The AFM allows detection of the surface topography at the nm-scale.

In particular, the AFM, generates a topographical map of a surface by recording attractive and repulsive short-range forces between the tip and the sample. When in tapping, *i.e.* intermitting contact, mode a bias applied to the cantilever in order to excite it at about its resonance frequency, hence enabling its oscillation over the surface.

A conical probe, of dimensions around 10nm, is mounted at an extremity of the cantilever, which is in turn connected to a piezoelectric actuator having sub-nanometer precision in the x, y and z axes.

To monitor the position of the probe, a laser is focused on the cantilever and a CCD photo-detects its reflection (Figure 2.9.1).

When the cantilever is subjected to a bias, its intensity of oscillation depends on the spring-constant of the cantilever itself and on the entity of bias applied but is normally in the order of a few nanometers. When approaching the surface the attractive and repulsive forces between the tip and the sample will start to play a role by increasing or decreasing the oscillation modulus. The piezoelectric actuator will adjust the position of the cantilever in order to either keeping the same distance from the surface or the same deflection. The obtained data will be, in the first case, about the z-position, in the second about the cantilever deflection.

The interaction between the tip and the surface can be described with a Lenard-Jones potential, having attractive forces playing a role at medium distances and strong repulsive forces when approaching the surface.

While acquiring the topographical image it is also possible to monitor the phase-shift of the oscillation of the tip. A variation in the phase is mainly attributable to a different chemical composition of the sample, to dramatic change in height in the sample. This further characterization allows better interpretation of the height results.

A particular case of AFM technique is the conducting-AFM (c-AFM). A conducting tip is used instead of a non-conducting one and a bias is applied between the tip and the sample. an external loop provided with an ammeter records the variation in current between the two. The sensitivity of the probe varies between pico and milliamp.

First of all the tip is in contact with the sample and the force applied to the tip can be monitored and tuned. Height, phase and current maps of the sample are acquirable simultaneously allowing determination both of the structures and their relative conductivities at a certain bias applied. It is moreover possible to acquire full IVs in certain pre-determined points in order to achieve information not only on the conductivity at a certain bias but of the electrical behavior of the structure.

Both sample and tip can be grounded; the choice depends on the measurements and on the sample.

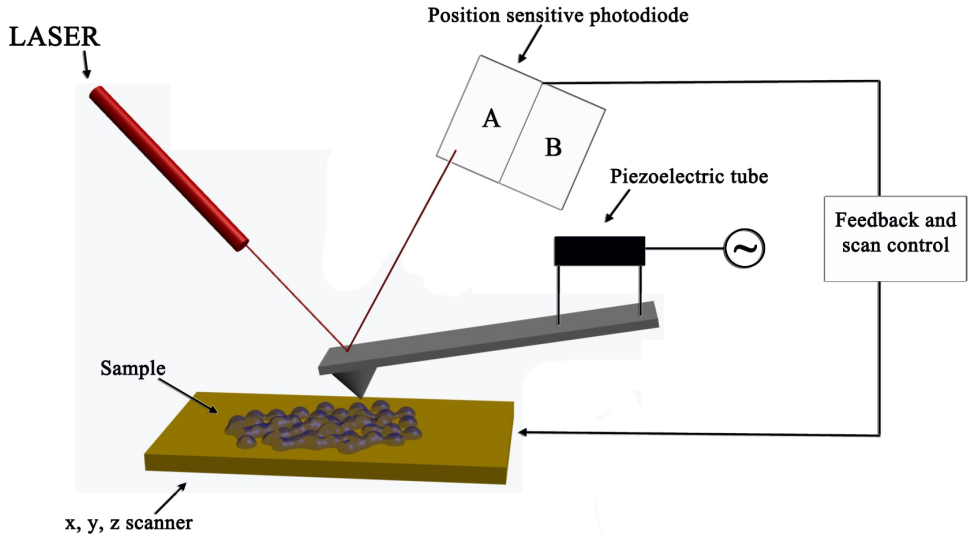

Figure 2.9.1 Sketch of an atomic force microscope.

References

1 Kagoshima, S., Kanoda, K. & Mori, T. Special Topics: Organic conductors - Preface. *Journal of the Physical Society of Japan* **75** (2006).

2 Mori, T. Requirements for Zero-Gap States in Organic Conductors. *Journal of the Physical Society of Japan* **79** (2010).

3 Mori, T., Terasaki, I. & Mori, H. New aspects of nonlinear conductivity in organic charge-transfer salts. *Journal of Material Chemistry* **17**, 4343-4347 (2007).

4 Mori, T. & Kawamoto, T. Organic conductors—from fundamentals to nonlinear conductivity. *Annual Reports Section C* **103**, 134-172 (2007).

5 Kronig, R. d. L. & Penney, W. G. Quantum Mechanics of Electrons in Crystal Lattices. *Proceedings of the Royal Society A* **130**, 499-513 (1931).

6 Pope, M. & Swenberg, C. E. Electronic Processes in Organic Crystals and Polymers. *Oxford University Press* (1999).

7 Bredas, J. L. & Street, G. B. Polarons, Bipolarons, and Solitons in Conducting Polymers. *Accounts of Chemical Research* **18**, 309-315 (1985).

8 Heeger, A. J. Charge Storage and Charge Transport in Conducting Polymers - Solitons, Polarons and Bipolarons. *Philosophical Transactions of the Royal Society A* **314**, 17-35 (1985).

9 Roth, S. & Carrol, D. One-Dimensional Metals. *Wiley-VCH Verlag GmbH & Co. KGaA, Weinheim* (2004).

10 Holstein, T. Studies of polaron motion Part I. The molecular-crystal model *Annals of Physics* **8**, 325-342 (1959).

11 Holstein, T. Studies of polaron motion Part II. The "small" polaron *Annals of Physics* **8**, 343-389 (1959).

12 Mott, N. F. The Theory of Crystal Rectifiers. *Proceedings of the Royal Society of London Series A* **171**, 27-38 (1939).

13 Sze, S. M. & Ng, K. k. Physics of Semiconductors Devices, third edition. *John Wiley & Sons, Inc., Hoboken, New Jersey* (2007).

14 Kahn, A., Koch, N. & Gao, W. Y. Electronic structure and electrical properties of interfaces between metals and pi-conjugated molecular films. *Journal of the Polymer Science Part B: Polymer Physics* **41**, 2529-2548 (2003).

15 Ivanco, J., Netzer, F. P. & Ramsey, M. G. On validity of the Schottky-Mott rule in organic semiconductors: Sexithiophene on various substrates. *Journal of Applied Physics* **101**, 103712/1-6 (2007).

16 Lu, C. Z. & Mohammad, S. N. Validity/invalidity of Schottky-Mott rules for Schottky contacts to III-V nitride semiconductor heterostructures. *Applied Physics Letters* **89**, 162111/1-3 (2006).

17 Mott, N. F. & E.A.Davis. Electronic Processes in Non-Crystalline Materials. *Clarendon Press, Oxford* (1979).

18 Lim, B. & Xia, Y. N. Metal Nanocrystals with Highly Branched Morphologies. *Angewandte Chemie International Edition* **50**, 76-85 (2011).

19 Wu, S. M. *et al.* Molecular junctions based on aromatic coupling. *Nature Nanotechnology* **3**, 569-574, (2008).

20 Luber, S. M. *et al.* High-aspect-ratio nanogap electrodes for averaging molecular conductance measurements. *Small* **3**, 285-289 (2007).

21 Mahapatro, A. K., Ghosh, S. & Janes, D. B. Nanometer scale electrode separation (nanogap) using electromigration at room temperature. *Ieee Transactions on Nanotechnology* **5**, 232-236 (2006).

22 Guo, S. W. The creation of nanojunctions. *Nanoscale* **2**, 2521-2529 (2010).

23 Cuniberti, G., Fagas, G. & Richter, K. Introducing Molecular Electronics. *Springer-Verlag Berlin Heidelberg* (2005).

24 Chen, Y. C., Zwolak, M. & Di Ventra, M. Inelastic current-voltage characteristics of atomic and molecular junctions. *Nano Letters* **4**, 1709-1712 (2004).

25 Engelkes, V. B., Beebe, J. M. & Frisbie, C. D. Length-dependent transport in molecular junctions based on SAMs of alkanethiols and alkanedithiols: Effect of metal work function and applied bias on tunneling efficiency and contact resistance. *Journal of the American Chemical Society* **126**, 14287-14296 (2004).

26 Chen, W. B. *et al.* Highly Conducting pi-Conjugated Molecular Junctions Covalently Bonded to Gold Electrodes. *Journal of the American Chemical Society* **133**, 17160-17163 (2011).

27 Selzer, Y. *et al.* Effect of local environment on molecular conduction: Isolated molecule versus self-assembled monolayer. *Nano Letters* **5**, 61-65 (2005).

28 Cohen, R., Stokbro, K., Martin, J. M. L. & Ratner, M. A. Charge transport in conjugated aromatic molecular junctions: Molecular conjugation and molecule-electrode coupling. *Journal of Physical Chemistry C* **111**, 14893-14902 (2007).

29 Love, J. C., Estroff, L. A., Kriebel, J. K., Nuzzo, R. G. & Whitesides, G. M. Self-assembled monolayers of thiolates on metals as a form of nanotechnology. *Chemical Reviews* **105**, 1103-1169 (2005).

30 Liscio, A., Palermo, V. & Samori, P. Nanoscale Quantitative Measurement of the Potential of Charged Nanostructures by Electrostatic and Kelvin Probe Force

Microscopy: Unraveling Electronic Processes in Complex Materials. *Accounts of Chemical Research* **43**, 541-550 (2010).

31 Love, J. C. *et al.* Formation and structure of self-assembled monolayers of alkanethiolates on palladium. *Journal of the American Chemical Society* **125**, 2597-2609 (2003).

32 Lennard-Jones, J. E. Cohesion. *The Proceedings of the Physical Society* **43**, 461-482 (1931).

33 Schwartz, D. K. Mechanisms and kinetics of self-assembled monolayer formation. *Annual Review of Physical Chemistry* **52**, 107-137 (2001).

34 Doudevski, I., Hayes, W. A. & Schwartz, D. K. Submonolayer island nucleation and growth kinetics during self-assembled monolayer formation. *Physical Review Letters* **81**, 4927-4930 (1998).

35 Schwartz, D. K., Hayes, W. A., Doudevski, I. & Woodward, J. T. Growth mechanisms of self-assembled monolayers. *Abstract of Papers of the American Chemical Society* **216**, U770-U770 (1998).

36 Ulman, A. Formation and structure of self-assembled monolayers. *Chemical Reviews* **96**, 1533-1554 (1996).

37 Schreiber, F. Structure and growth of self-assembling monolayers. *Progress in Surface Science* **65**, 151-256 (2000).

38 Karpovich, D. S. & Blanchard, G. J. Direct Measurement of the Adsorption-Kinetics of Alkanethiolate Self-Assembled Monolayers on a Microcrystalline Gold Surface. *Langmuir* **10**, 3315-3322 (1994).

39 Dubois, L. H., Zegarski, B. R. & Nuzzo, R. G. Molecular Ordering of Organosulfur Compounds on Au(111) and Au(100) - Adsorption from Solution and in Ultrahigh-Vacuum. *Journal of Chemical Physics* **98**, 678-688 (1993).

40 Dubois, L. H. & Nuzzo, R. G. Synthesis, Structure, and Properties of Model Organic-Surfaces. *Annual Review of Physical Chemistry* **43**, 437-463 (1992).

41 Rao, C. N. R., Kulkarni, G. U., Thomas, P. J. & Edwards, P. P. Metal nanoparticles and their assemblies. *Chem Soc Rev* **29**, 27-35 (2000).

42 Mie, G. *Annals of Physics-New York* **25**, 377-445 (1908).

43 Rechberger, W. *et al.* Optical properties of two interacting gold nanoparticles. *Optics Communications* **220**, 137-141 (2003).

44 Baletto, F. & Ferrando, R. Structural properties of nanoclusters: Energetic, thermodynamic, and kinetic effects. *Review of Modern Physics* **77**, 371-423 (2005).

45 G.Wulff. *Krystallographie* **34**, 449-530 (1901).

46 Hering, C. Some theorems on the free energies of crystal surfaces. *Physical Review* **82**, 87-93 (1951).

47 Nicolais, L. & Carotenuto, G. Metal-polymer nanocomposites. *John Wiley & Sons, Inc.* (2005).

48 Pyykko, P. Structural properties - Magic nanoclusters of gold. *Nature Nanotechnology* **2**, 273-274, doi:Doi 10.1038/Nnano.2007.119 (2007).

49 Sorensen, C. M., Klabunde, K. J. & Richards, R. M. Particles as Molecules. *Nanoscale Materials in Chemistry*, 37-69 (2009).

50 Zabet-Khosousi, A. & Dhirani, A. A. Charge transport in nanoparticle assemblies. *Chemical Reviews* **108**, 4072-4124 (2008).

51 H Horowitz, G. Organic field-effect transistors. *Advanced Materials* **10**, 365-377 (1998).

52 Facchetti, A. Semiconductors for organic transistors. *Materials Today* **10**, 28-37 (2007).

53 Ortiz, R. P., Facchetti, A. & Marks, T. J. High-k Organic, Inorganic, and Hybrid Dielectrics for Low-Voltage Organic Field-Effect Transistors. *Chemical Reviews* **110**, 205-239 (2010).

54 Horowitz, G. Interfaces in Organic Field-Effect Transistors. *Organic Electronics* **223**, 113-153 (2010).

55 Necliudov, P. V., Shur, M. S., Gundlach, D. J. & Jackson, T. N. Contact resistance extraction in pentacene thin film transistors. *Solid State Electronics* **47**, 259-262 (2003).

56 Crivillers, N. *et al.* Photoinduced work function changes by isomerization of a densely packed azobenzene-based SAM on Au: a joint experimental and theoretical study. *Physical Chemistry Chemical Physics* **13**, 14302-14310 (2011).

57 Bao, Z. & Locklin, J. Organic Field-Effect Transistors. *CRC Press* (2007).

58 Irie, M., Eriguchi, T., Takada, T. & Uchida, K. Photochromism of diarylethenes having thiophene oligomers as the aryl groups. *Tetrahedron* **53**, 12263-12271 (1997).

59 Luo, Q. F., Cheng, H. & Tian, H. Recent progress on photochromic diarylethene polymers. *Polymer Chemistry* **2**, 2435-2443 (2011).

60 Kobatake, S., Takami, S., Muto, H., Ishikawa, T. & Irie, M. Rapid and reversible shape changes of molecular crystals on photoirradiation. *Nature* **446**, 778-781 (2007).

61 Irie, M. Photochromism and molecular mechanical devices. *Bulletin of the Chemical Society of Japan* **81**, 917-926 (2008).

62 Balzani, V., Credi, A. & Venturi, M. Molecular Devices and Machines. *Wiley-VCH Verlag GmbH & Co. KGaA, Weinheim* (2004).

63 Turro, N. J., Ramamurthy, V. & Scaiano, J. C. Principle of Molecular Photochemistry. *University Science Books* (2009).

64 Bandara, H. M. D. & Burdette, S. C. Photoisomerization in different classes of azobenzene. *Chemical Society Reviews* **41**, 1809-1825 (2012).

65 Elbing, M. *et al.* Single Component Self-Assembled Monolayers of Aromatic Azo-Biphenyl: Influence of the Packing Tightness on the SAM Structure and Light-Induced Molecular Movements. *Advanced Functional Materials* **18**, 2972-2983 (2008).

66 Pace, G. *et al.* Cooperative light-induced molecular movements of highly ordered azobenzene self-assembled monolayers. *Proceedings of the National Academy of Sciences* **104**, 9937-9942 (2007).

67 Ferri, V. *et al.* Light-powered electrical switch based on cargo-lifting azobenzene monolayers. *Angewandte Chemie International Edition* **47**, 3407-3409 (2008).

68 Mativetsky, J. M. *et al.* Azobenzenes as light-controlled molecular electronic switches in nanoscale metal-molecule-metal junctions. *Journal of the American Chemical Society* **130**, 9192-9193 (2008).

69 Crivillers, N., Orgiu, E., Reinders, F., Mayor, M. & Samori, P. Optical Modulation of the Charge Injection in an Organic Field-Effect Transistor Based on Photochromic Self-Assembled-Monolayer-Functionalized Electrodes. *Advanced Materials* **23**, 1447-1452 (2011).

70 Raman, C. V. & Krishnan, K. S. A new type of secondary radiation. *Nature* **121**, 501-502 (1928).

71 Fleischmann, M., Hendra, P. J. & McQuillan, A. J. Raman spectra of pyridine adsorbed at a silver electrode. *Chemical Physics Letters* **26**, 163-166 (1974).

72 Garrell, R. L. Surface-Enhanced Raman-Spectroscopy. *Anal Chem* **61**, A401 (1989).

73 Haynes, C. L., McFarland, A. D. & Van Duyne, R. P. Surface-enhanced Raman spectroscopy. *Analytical Chemistry* **77**, 338A-346A (2005).

74 Nie, S. M. & Emery, S. R. Probing single molecules and single nanoparticles by surface-enhanced Raman scattering. *Science* **275**, 1102-1106 (1997).

75 Moskovits, M. Surface-enhanced Raman spectroscopy: a brief retrospective. *Journal of Raman Spectroscopy* **36**, 485-496 (2005).

Chapter 3. Methods and Experimental Techniques

The following section will provide an overview of the techniques that were employed during the thesis. First, the SAM procedure on Au surfaces will be presented for both free and acetylated thiols, followed by the synthesis of the nanoparticles, their basic physico-chemical characterization and the ligand-exchange reaction. The nanotrenches used to perform electrical characterization at the nanoscale will then be presented from a fabrication point of view as well as their basic properties discussed. Finally the basic characteristics of the patterned-test for OFETs together with the chosen way to extract all the characteristic data shall be covered.

The materials and instrumental specifications used are listed in the Appendix, at the end on this chapter.

3.1 Self-Assembled monolayer formation

The Au substrates were either freshly evaporated or cleaned (see section 3.5 and 3.6 for empirical procedure) and incubated (24 – 48 hours) in a N_2 degassed solution of AZO molecules having a terminal acetylated thiol group to prevent disulfide formation, for either 24 or 48 hours. Final concentration was 0.5 mM in aqueous NaOH : ethanol : chloroform : toluene (1:20:7:30 v/v) to allow complete

miscibility of the solvents[1] and deprotection via basic hydrolysis of the acetylthiol group.[2] The chloroform used was passed over basic alumina prior to use to remove any acidic impurities. Finally, the substrates were rinsed 3 – 10 times with chloroform and dried under a stream of N_2. An identical procedure was carried out for OPE molecules.

Self-assembly was carried out without deprotection *in-situ* but with incubation for over 72 h. The two procedures yielded similar results. All the SAMs of thiolated molecules were instead simply prepared by incubation (24 – 48 hours) in a solution 1 – 10mM in EtOH.[3,4] (Figure 3.1.1).

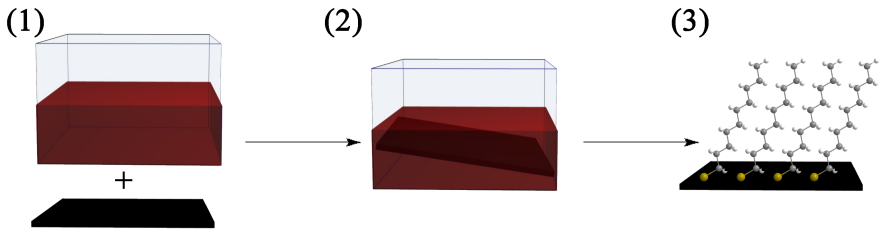

Figure 3.1.1 Cartoon of the SAM formation technique employed. Preparation of the solution and cleaning of the substrate (1), followed by incubation of the substrate in the solution (2), that leads to the formation of the SAM (3).

3.2 Nanoparticles synthesis and ligand exchange reaction and characterization

AuNPs (1 – 30 nm) featuring alkylamines[5] [(3.1a), (3.1b)] or citrate[6,7] coating layers were synthesized according to literature procedures, but varying the relative amounts and typology of reagents in order to tune the sizes.[8-10] A ligand exchange reaction was then performed to obtain alkylthiol, AZO and mixed SAMs AZO-alkylthiol and OPE- alkylthiol coating layers.

$$\mathrm{mAuCl_{4(aq.)}^{-}} + \mathrm{mN(C_8H_{17})_4^{+}{}_{(toluene)}} \rightarrow \mathrm{m[N(C_8H_{17})_4^{+}AuCl_4^{-}]_{(toluene)}} \qquad (3.1a)$$

$$m[N(C_8H_{17})_4^{+}AuCl_4^{-}]_{(tol.)} + n(alkylamine)_{(tol.)} + 3me^{-} \rightarrow$$
$$\rightarrow 4mCl_{(aq.)}^{-} + (Au_m)(alkylamine)_{(n-x)(tol.)} + x(alkylamine)_{(tol.)} + \mathrm{mN(C_8H_{17})_4^{+}{}_{(tol.:aq)}} \qquad (3.1b)$$

3.2.1 General procedure for the synthesis and purification of alkylamine coated gold nanoparticles (3-25 nm in size) in toluene[5,8-10]

1 equivalent of $HAuCl_4$ was dissolved in MilliQ water (Concentration(C) ~ 15mM). 3 equivalents of tetraoctylammonium bromide (TOAB) were dissolved in toluene (C ~ 45mM). The two solutions were mixed in flask and stirred approximately 30 minutes, until the water (bottom in the flask) solution became colorless.

"x" equivalents of alkylamina in toluene were fast added to the solution and left stirring approximately 5 minutes to assure complete homogeneity.

"y" equivalents of $NaBH_4$ dissolved in water, and prepare maximum 5 minutes before using, were added to the solution.

The solution was stirred for 12-24 hours to allow completing of the reaction.

The values of "x", "y" and the alkylamina used depended on the targeted nanoparticles size, following Table 3.2.1.

Table 3.2.1 Values of x, y, and chosen alkylamina for the synthesis of the different nanoparticles.

	x	*y*	*Chosen alkylamina*
3 nm	50	10	Octadecylamina
15 nm	20	10	Hexylamina
25 nm	10	10	Hexylamina

Purification of the nanoparticles synthesized was achieved by extraction 3 times with water of the toluenic solution.

3.2.2 General procedure for the synthesis of ~1nm AuNPs coated with AZO in toluene (AZOAuNPs)

1 equivalent of $HAuCl_4$ was dissolved in MilliQ water (Concentration(C) ~ 15mM). 3 equivalents of tetraoctylammonium bromide (TOAB) were dissolved in toluene (C ~ 45mM). The two solutions were mixed in flask and stirred approximately 30 minutes, until the water (bottom in the flask) solution became colorless.

50 equivalents of alkylamina in toluene were fast added to the solution and left stirring approximately 5 minutes to assure complete homogeneity.

20 equivalents of $NaBH_4$ dissolved in water, and prepare maximum 5 minutes before using, were added to the solution that was left stirring for 10 minutes.

The toluene solution was separated from the aqueous one and 10 equivalents of AZO dissolved in chloroform:ethanol:aqueous NaOH were added to the solution.

The solution was stirred for 72 hours to allow completing of the reaction.

The aqueous phase was separated and discarded. The organic phase was reduced in volume by rotary evaporation and adding an excess of EtOH (where the AZO molecules are soluble) and cooling to 4°C for 12 hours. The solution was removed and the solid rinsed three times with ethanol. The solid was resospended in toluene and further purified via centrifugation resospension 7 – 10 times with EtOH. After evaporation of the solvent via rotary evaporation the nanoparticles were resospended in toluene.

3.2.3 General procedure for the synthesis of citrate coated gold nanoparticles (15 nm in size) in water[6,7]

1 equivalent of $HAuCl_4$ was dissolved in MilliQ water, the solution was stirred while heating until reaching of the boiling point (T ~ 100 °C). 30 equivalents of trysodium citrate were added to the boiling solution and left stirring at the same temperature for 1hour. The solution was then slowly cooled down while stirring for a total of 12 hours.

3.2.4 General procedure for the Ligand-exchange reaction with a monocomponent SAM[11]

10 equivalents of acetylated ligand (AZO or OPE) were dissolved in a mixture of aqueous NaOH:ethanol:chloroform:toluene (1:20:7:30 volumes equivalents),[1] added to 1 equivalent of alkylamina coated AuNPs in toluene and stirred for 24 hours. The aqueous phase was separated and discarded. The organic phase was reduced in volume by rotary evaporation and adding an excess of EtOH (where both the AZO and OPE molecules are quite soluble) and cooling to 4°C for 12 hours. The solution was removed and the solid rinsed three times with ethanol. The solid was resospended in toluene and further purified via centrifugation resospension 7 – 10 times with EtOH.

After evaporation of the solvent via rotary evaporation the nanoparticles were resospended in toluene.

Similar results, although less reproducible, were obtained when following a reported hydrolysis-free synthetic route. [12]

3.2.5 General procedure for the Ligand-exchange reaction with a bicomponent SAM.[11]

10 equivalents of dodecanethiol were dissolved in EtOH and added to 1 equivalent of alkylamine coated AuNPs. The solution was stirred for 12 hours.

The organic colloidal solution was reduced in volume by rotary evaporation and adding an excess of EtOH and cooling to 4°C for 12 hours. The solution was removed and the solid rinsed three times with ethanol. The solid was resospended in toluene and further purified via centrifugation resospension 7 – 10 times with EtOH. After evaporation of the solvent via rotary evaporation the nanoparticles were resospended in toluene. 10 equivalents of acetylated ligand (AZO or OPE) were in a mixture of aqueous NaOH:ethanol:chloroform:toluene (1:20:7:30 volumes equivalents),[1] added to 1 equivalent of alkylamina coated AuNPs in toluene and stirred for ~100 hours. The aqueous phase was separated and discarded. The organic phase was reduced in volume by rotary evaporation and adding an excess of EtOH (where the AZO molecules are soluble) and cooling to 4°C for 12 hours. The solution was removed and the solid rinsed three times with ethanol. The solid was resospended in toluene and further purified via centrifugation resospension 7 – 10 times with EtOH. After evaporation of the solvent via rotary evaporation the nanoparticles were resospended in toluene.

3.2.6 Physico-Chemical Characterization

^{1}H-NMR and UV-Vis Spectroscopy were respectively used to assess purity and size of the nanoparticles. Both techniques were used as well to determine the isomerization state and morphology of the SAM in the AZOAuNPs case (see Chapter IV).

The size determination was based on the SPR of the metal, well-known technique, as explained in Chapter I. This technique is nevertheless dependent on the

particular chemical environment studied. Therefore, representative samples for solvent, SPR maximum and coating layer were investigated by micrographic techniques as well (TEM, STEM and AFM) in order to confirm the UV-Vis determination of the nanoparticles size. As an example, Figure 3.2.1 shows representative ^{1}H-NMR and UV-Vis spectra for the 3, 15, 25 nm sizes of NPs. The UV-Vis spectra refer to the precursor nanoparticles while the ^{1}H-NMR to AZO molecules in toluene solution and when coating AuNPs. Due to aggregation issues the UV-Vis spectra of the AZO system are not shown (see Chapter IV).

The dodecanethiol and the mixed layer coated AuNPs showed similar SPR before and after ligand-exchange reaction, which confirmed the reaction completion without aggregation. The colloidal solutions of alkylamine-coated AuNPs obtained by synthesis in toluene had a λ_{MAX} = 510 nm for the 3 nm in size, λ_{MAX} = 525 nm for the 15 nm in size and λ_{MAX} = 530 nm for the 25 nm in size. No SPR was shown for the 1 nm gold nanoparticles.

All the ^{1}H-NMR spectra were acquired in toluene-d_8. The spectrum of AZO in toluene was recorded as well for comparison reasons with the AZOAuNPs spectra. Peaks were assigned based on COSY experiments for the molecule in solution. No COSY experiment was possible for the nanoparticles samples since the intensity of the spectra wasn't enough to define the protons' couplings and due to the close vicinity of the solvents peaks. In the AZO molecule spectra, different peaks between 6.5 and 8.5 ppm were present before and after irradiation. Spectra acquired before irradiation and after storing in dark an irradiated solution were identical. The different peaks in the irradiated samples were thus attributed to the *cis*-form of the AZO molecule. The lower definition of the ^{1}H-NMR spectra in the NPs samples when compared with the molecule can be explained by the rather low concentration of organic molecules on the nanoparticles sufaces, on the low solubility and on the intrinsic difficulties in acquiring a ^{1}H-NMR spectrum when nanoparticles are involved. The NPs size dependence of the AZO protons shift should be underlined. For bigger nanoparticles the most affected protons are the ones near the sulphur atom that covalently interacts with the NPs. One can hypothesize that both the SPR and the interaction between neighboring molecules have an effect on the chemical shifts of the aromatic protons. This last factor could explain the difference in spectra between the considered moieties.

It was not possible to unequivocally assign all the AZO peaks and only the peaks at higher chemical shift could be ascribed to the protons the least affected by the SPR, i.e. situated far away from the gold nanoparticle. The peak at 1.9 ppm was attributed to the methyl unit of the acetyl moiety. The combined analysis of the two signals provided direct information on the stoichiometry of AZOAuNP and AZO ratio in the solution, allowing determination of the AZO coverage of the nanoparticles surface.

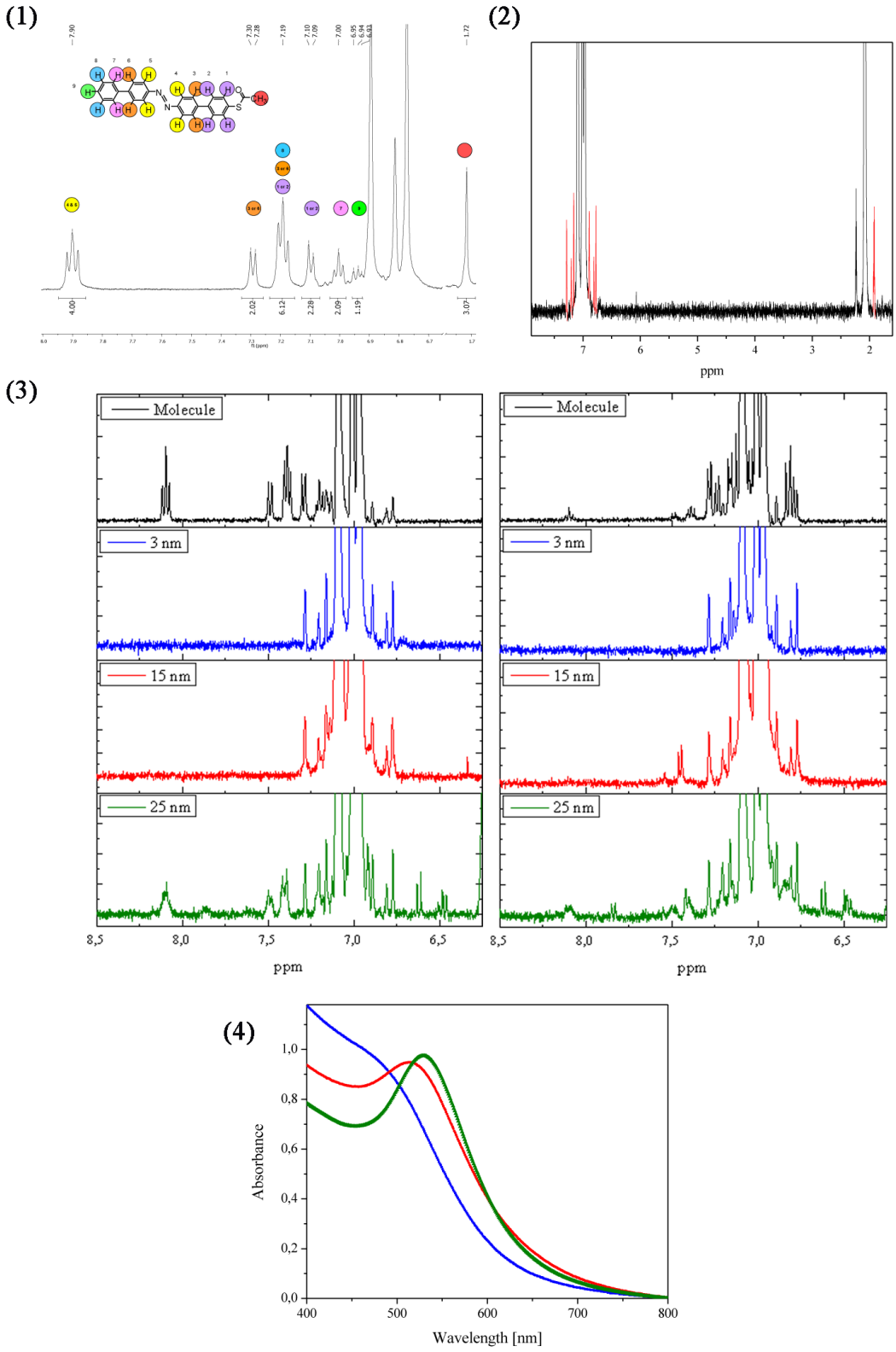

Figure 3.2.1 Physico-chemical analysis of the nanoparticles. 1) ^{1}H-NMR spectrum of azobenzene molecule in toluene with peaks assignment done by a COSY experiment, 2) ^{1}H-NMR spectrum of azobenzene coated 3 nm gold nanoparticles in toluene full range for sample's purity determination reasons, 3) ^{1}H-NMR spectra of the aromatic region (between 8.5 and 6.25 ppm) of, from top to bottom, azobenzene molecule, 3 nm size AZOAuNP, 15 nm size AZOAuNP, 25 nm size AZOAuNP, on the

left before UV irradiation, on the left after UV irradiation; 4) UV-Vis spectra of the precursor nanoparticles presented in 3).

3.3 100 nm gap nanotrench electrode fabrication, patterning and electrical characterization

To achieve higher aspect ratio (HAR) with a gap size down to 20 nm, elevate reproducibility and to avoid the use of e-beam lithography that implies greater instrumentation costs and reliability issues when an HAR is desired, a simple and new technique was designed and employed by our collaborator Professor Bernard Doudin (at I.P.C.M.S., in Strasbourg) (Figure 3.3.1).

Overall, the nanotrench fabrication process is composed of two general steps: the first optical lithography step followed by the first evaporation and a lift-off process, and the second optical lithography step followed by the "tilted-evaporation" and the final lift-off process.

In particular:

- First optical lithography:
  - Substrate cleaning by sonication and acetone-isopropanol washing.
  - Oxygen plasma treatment for resistor's protecting layer residues removal (100 Watts O_2 plasma for 20 minutes).
  - Photoresist's spin-coating at 4000 rpm for 30 s (1.4 μm thick layer).
  - Prebaking for 2 min at 120 ℃ on a hotplate.
  - Mask positioning.
  - Exposure time 2.5 s under 365 nm UV illumination. (calculated from the UV illumination intensity in order to get the optimum dose for the used photoresist).
  - Backing for 1.5 min at 120 ℃.
  - Resist's image reversal through flood exposure for 30 s.
  - Development, in AZ®726 MIF photoresist developer for 25 s, followed by extensive rinsing with distilled water, and N_2 blow down.
- First electrode (5 nm Ti followed by 25 nm Ni and 30 nm Au) evaporation
- Lift-off steps:
  - Acetone for 30 min over mild agitation
  - Acetone and isopropanol rinsing

- Nitrogen-flow drying

- Oxygen plasma treatment to ensure full collar resist removal.
- Second optical lithography process (equivalent to the first one)
- Tilted-angle evaporation

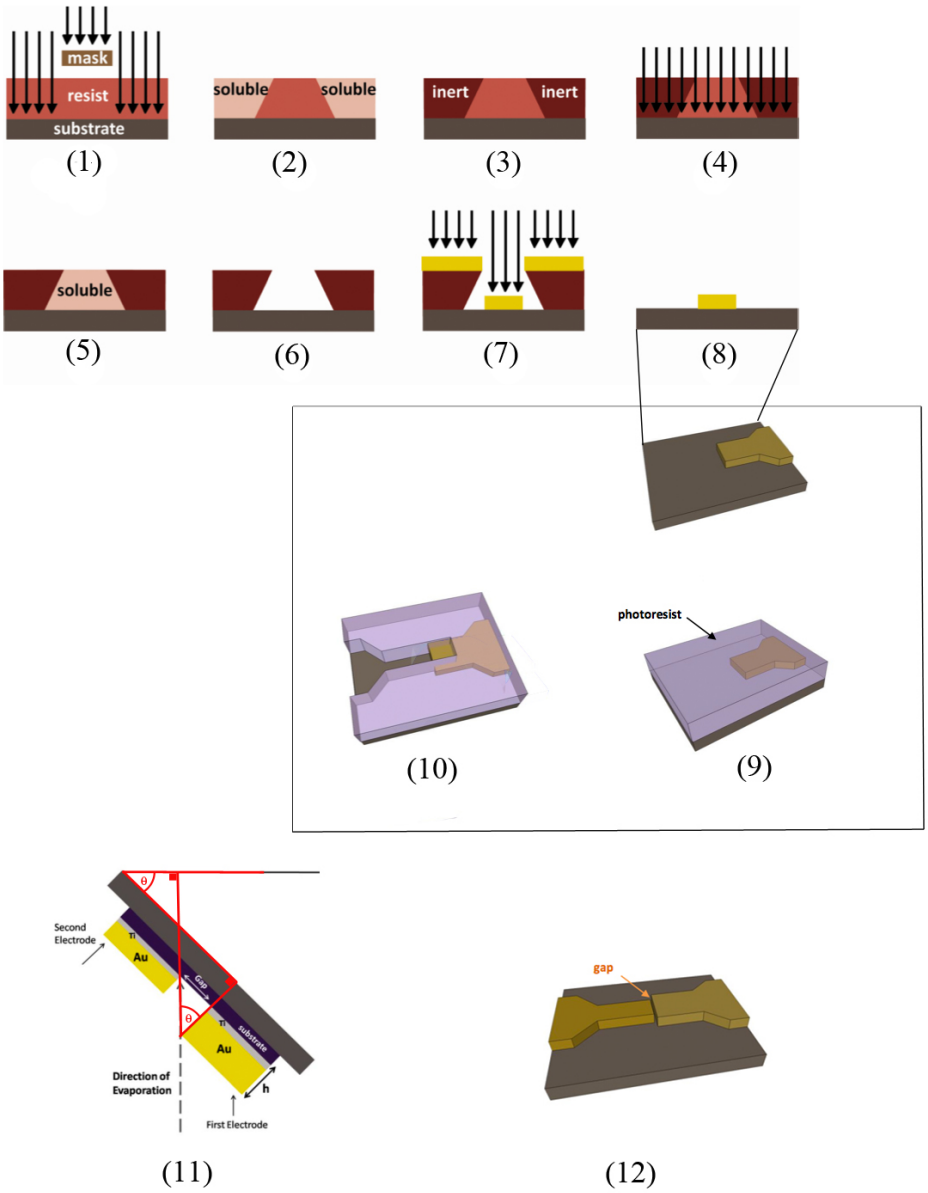

Figure 3.3.1 Microfabrication using optical lithography (employing image reversal process followed by lift off) and edge mediated shadow mask lithography process, (1) light-exposure through a positive mask, (2) sketch of different water solubilities depending on light-exposure, (3) reversal baking that allows crosslinking of the exposed area when the unexposed remains photoactive, (4) second light-exposure without mask, (5) the unexposed area becomes soluble, (6) developing, (7) metallic film evaporation, (8) lift-off, (9) and (10) patterning of the second layer using the same optical lithography process used for the first, (11) schematic edge mediated shadow mask lithography process in which the length of the gap is set by the height h of the first electrode and the angle Θ of the tilted sample following $L = h \times tg(\Theta)$, (12) final electrode.

One of the crucial validation steps is the acquisition of SEM images of the produced nanotrenches because it allows to immediately see short-circuits and to have a blank for the following tests. (Fig. 3.3.2)

Open gaps nanotrenches with significantly high reproducibility were obtained up to 90% success rate.

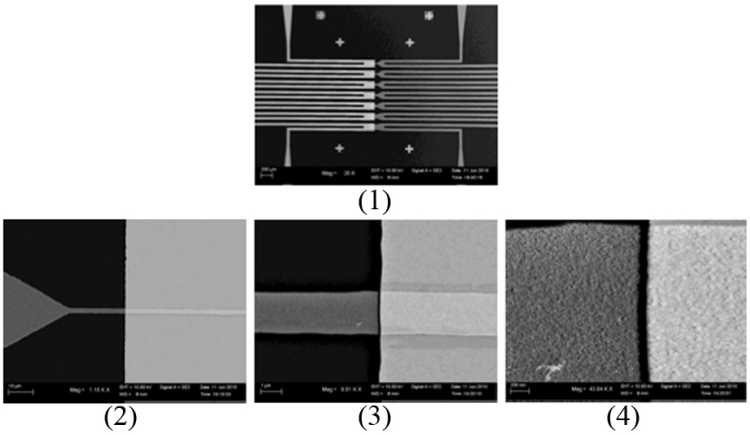

Figure 3.3.2 SEM images of (1) an example of a nanotrench, (2), (3) and (4) three different magnifications of 3μm long × 80nm wide gaps.

A proper electrical characterization is crucial because a minimal leakage current is required to have a robust measurement tool. Almost no photoresist contamination was found on the devices obtained, allowing high electrical stability and reliability of the electrical contacts.

Considering a maximum current-leakage criterion, it was estimated that 90% of the samples showed a leakage current below 10 pA under 1V stress voltage and for 30% of them the value was below 1 pA. (Figure 3.3.3)

In-depth treating on the nanotrenches fabrication technique is reported in the J-F Dayen's paper titled "*Nanotrench for nano and microparticle electrical interconnects*"[13].

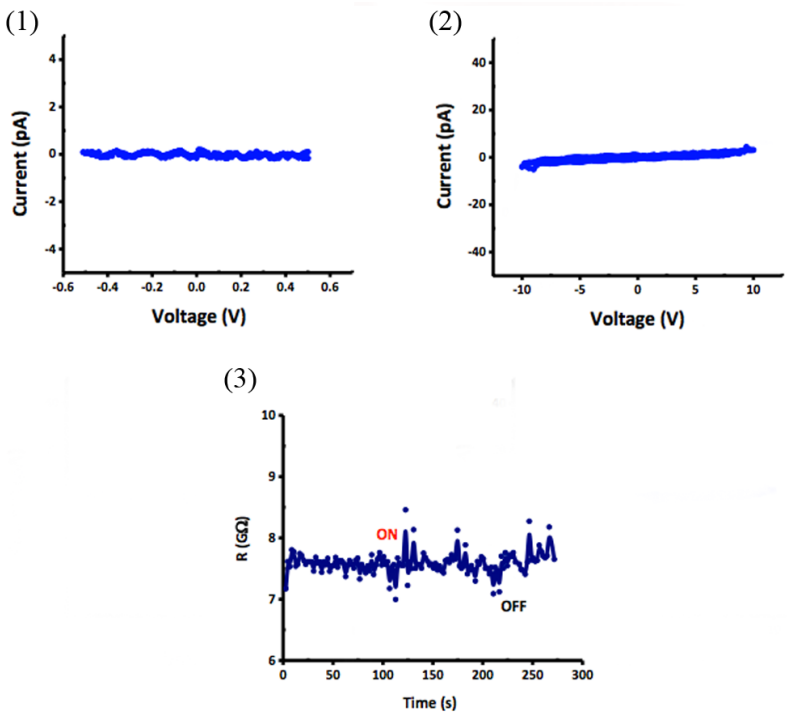

Figure 3.3.3 Current-Voltage characteristics of empty nanotrench electrodes electrodes in ambient conditions, a) 500mV range, b) 1V range, c) 5V range, d) 10V range, e) Monitoring the leakage current of an empty trench, in the presence of 7.4 W luminous intensity and 110℃ temperature, Voltage = 1V=cte.

3.3.1 Preparation of half-metal coated silica microspheres

Starting material was Sicastar®Monodisperse silica Microspheres with mean diameter ranging from 100 nm to 1.00 µm (Micromod) and Polystyrene monodisperese microspheres (Polysciences) mean diameter 1.00 µm that was diluted and washed in distilled water using a dispersion/ centrifugation technique.

Microscope coverslips were cleaned with acetone and ethanol, dried under a flow of nitrogen and exposed to oxygen plasma to render them hydrophilic.[14]

The miscrospheres dispersed in aqueous solution were then drop casted into the slides. Once the solvent evaporated, metal evaporation via e-beam of Ti/Ni/Au was performed on the spheres. Soft sonication in ethanol was then performed allowing detachment of the microspheres. The microspheres were cleaned using centrifugation followed by resuspension in ethanol.[15]

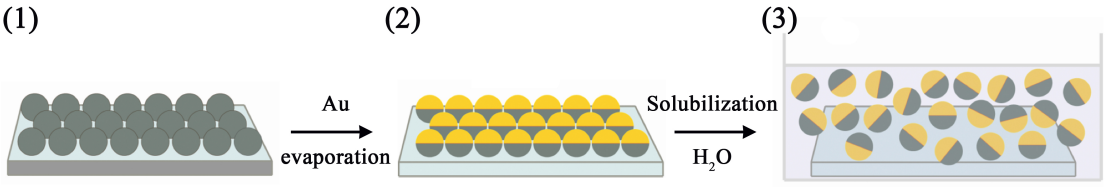

Figure 3.3.4 Schematic representation of preparation of half-metal-coated microspheres: drop casting on a surface (1), metal evaporation (2), and suspension in EtOH via sonication (3).

3.3.2 Magnetic trapping of microspheres

To close the circuit it was decided to use an approach developed by Long et al.,[16] based on the magnetic trapping of micrometer sized particles on gap-spaced electrodes. First, the electrodes were magnetized thanks to the ferromagnetic properties of the Ni layer, second the microspheres were trapped by immersion of the electrodes in a solution containing half-coated, 1 μm in diameter, polystyrene spheres. The spheres were coated with the same metals allowing a response to the magnetic field and so the trapping in the nanogaps. (Figure 3.3.5) Important to this technique are the high efficiency of the microspheres trapping and the possibility of using any substrate.

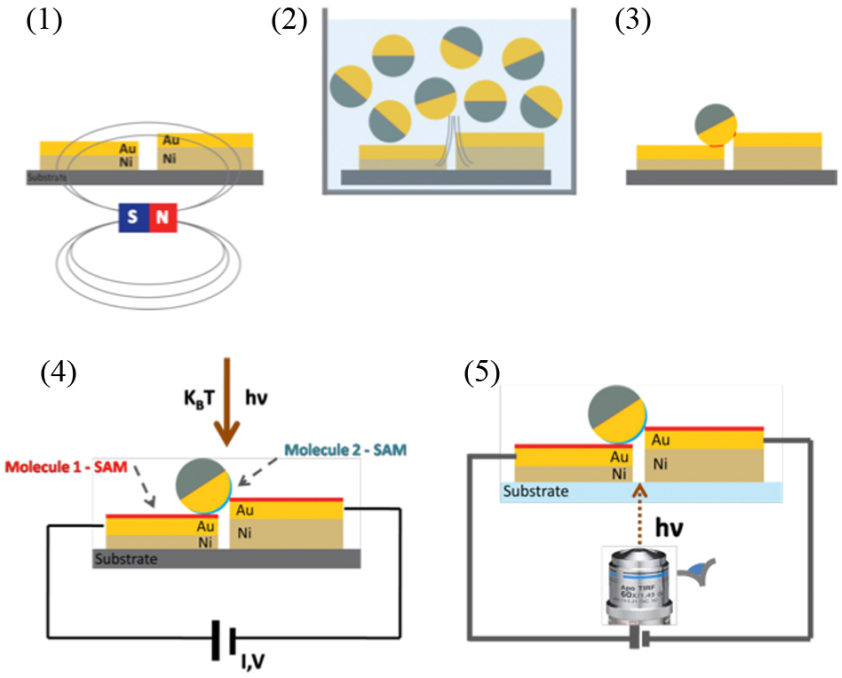

Figure 3.3.5 Magnetic trapping steps: 1) magnetization of the ferromagnetic layer (Ni) perpendicular to the nanotrench width to allow formation of a magnetic field gradient in the trench area using a permanent magnet of Ni-N52 (D = 10 mm, L=10 mm, inside magnetic flux = 1.43T and outside magnetix flux = 5600 G); 2) immersion of the substrate in a solution containing half- coated (5nm Ti

covered with 30 nm Ni and 20 nm Au) polystyrene microsphere (Polysciences, 1 μm diameter) followed by soft agitation for 20 minutes; 3) rinsing and drying to form a solid array of microspheres on the trench area, due to the nanotrench fabrication technique the output will be asymmetric as shown in the figure (superimposition of two evaporated layers on one side and only one in the other); 4) microsphere molecular junction on an opaque substrate (Si wafer covered by 550 nm SiO_2); 5) microsphere molecular junctions on a transparent substrate (130-170 μm thick microscope coverglass/quartz compatible with reflection spectroscopy).

The electrical characterization was performed before and after trapping showing mA currents in presence of the particle. Typical IV characteristics and SEM images of the trench after trapping are reported in Figure 3.3.6.

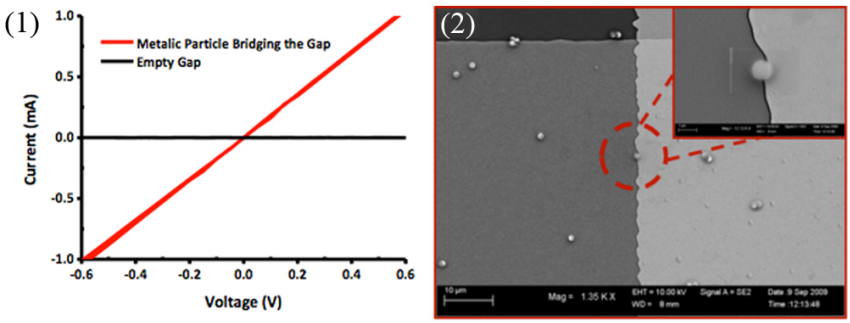

Figure 3.3.6 1) IV characteristics over a 600 mV range before (black) and after (red) magnetic trapping of 1 μm coated sphere. 2) SEM micrograph of a 100 μm wide trench after 1 μm sphere trapping.

3.3.3 Electrical Connection Scheme.

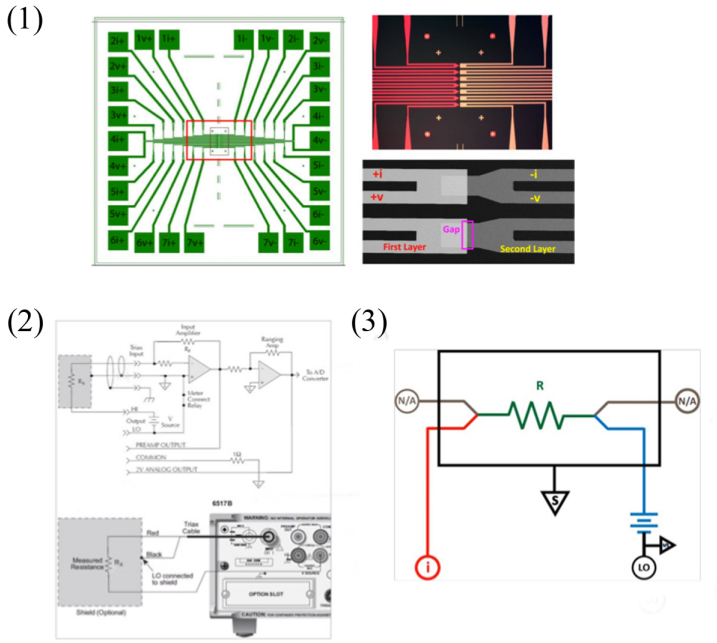

Figure 3.3.7 (1) Left: Sketch of the Optical lithography mask used fin the nanotrenches patterning on a 25 mm^2 substrate, the red rectangle marked area is zoomed in the top right image, containing seven

nanotrenches in parallel, and showing two nanotrenches in an SEM micrograph with a more zoomed image (bottom-right image). (2) electrical circuit and connection guide for the Keithley 6517B electrometer, with floating ground system, (3) the connection circuit for two point measurements where one side of the sample is connected to current reading and the other side to the voltage source, applying a voltage regarding the shield (S).

3.4 Preparation 50 nm gold electrodes

50 nm gap electrodes were designed to get an interdigitated large gap area (Figure 3.4.1.)

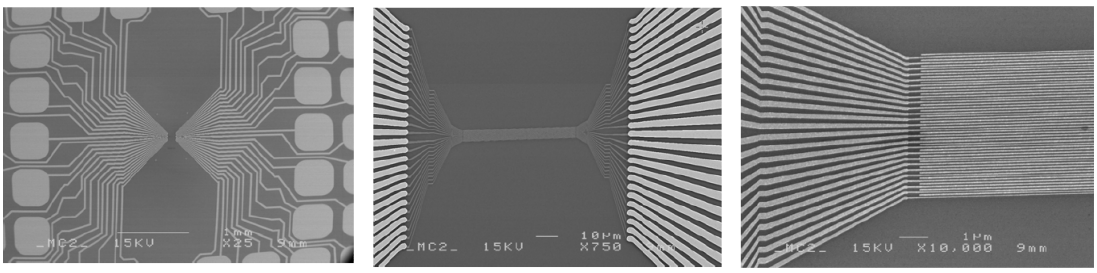

Fig.3.4.1 Images of the 50 nanometers gap electrodes. Left and right electrodes interdigit in the central path for a length of 5um. Every single sample has 52 electrodes and 51 gaps to be tested.

The electrodes preparation consisted in a two step process involving optical lithography to obtain the main features (large contact pads and intermediate contacts) followed by e-beam lithography for the nanometer scale features. (Figure 3.4.2)
For the nm-scale features, e-beam lithography was used instead of optical lithography, the only difference being that the sample is exposed to an e-beam instead of UV-light. The devices obtained are transistors, composed of three electrodes with a dielectric layer.

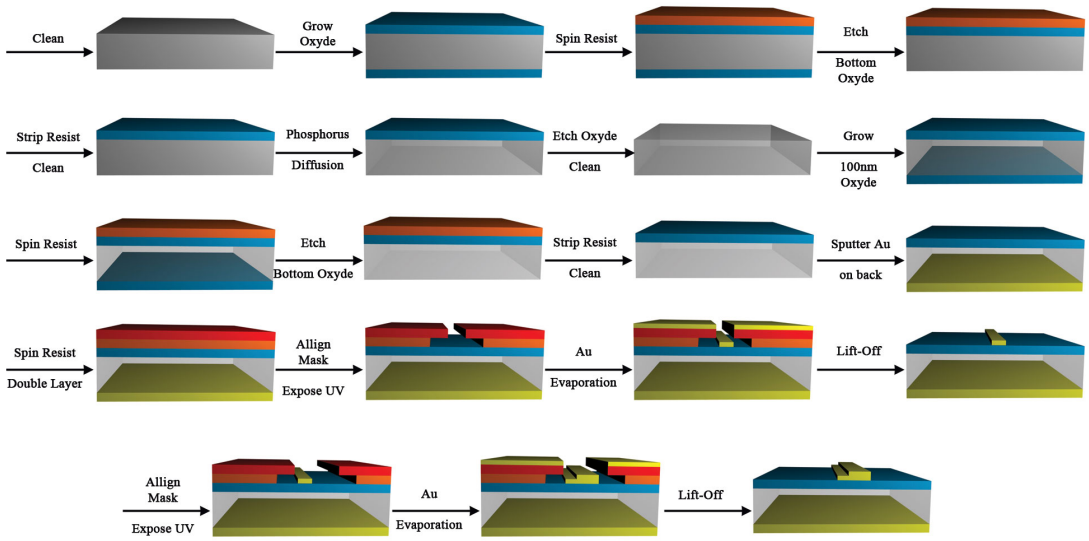

Fig. 3.4.2 Steps of the optical lithography process used for this porpoise. The masks geometry follows the one reported in figure 3.1.1.

3.4.1 Nanoparticles deposition and Circuit

In order to utilize the previously described transistors as horizontal electrodes, six steps were necessary: (Figure 3.4.3)

1. Cleaning the protecting resist layer on top of the junctions.
2. SAM functionalization of the electrodes
3. Hitching of the electrode over a magnet using tape to insulate the bottom third electrode and connect the device to a magnetic substrate, allowing stabilization over C-AFM measurements.
4. Connection via silver-paste of every other electrode obtaining a device composed of every other electrode connected, while the middle electrodes are left unconnected. (see Figure 3.3.2, 1) for the picture of the result).
5. Deposition of 80 nm gold nanoparticles on the nanogaps via drop casting.
6. Electrical measurements.

(The nanoparticles' characteristics are presented in Annex I.)

The fifth step in the characterization process was done as follows:

- drop casting of 10 µL of the AuNPs on top of the substrate functionalized with a SAM
- 6 h physisorption and drop casting on top of 100 µL of milliQ water

- after 18 h the sample was abundantely rinsed with milliQ water, and dried under a light N_2 flow.

The three step deposition process was necessary to get the proper concentration of NPs on the substrate, avoiding formation of aggregates. Importantly, the citrate electrostatically stabilizes the NPs and thus, no real bond is formed between the citrate coating layer and the NPs. For this reason, it can easily be substituted with other molecules. When an electrostatic ligand coats the NPs, can easily reorganize, making the NPs act as nude objects.

The same NPs have already been used to perform studies of conductivity over nanogap-electrodes[17] and, even in this precise case, the presence of citrate did not influence the actual measurements because it was easily replaced by the other studied molecules.

From a device's structure point of view (Figure 3.4.3 1)), the insulation of the bottom electrode allows use of the structure as a planar nanogap electrode in horizontal configuration. Since the electrodes constituting the device are interdigitated, it is possible to connect one side having one out of two connected electrodes, depositing the NPs to close the circuit and measure (Figure 3.4.3 2)). Two sets of measurements were performed: one in smaller scale, by employment of a C-AFM and the second on larger scale employing an electrometer.

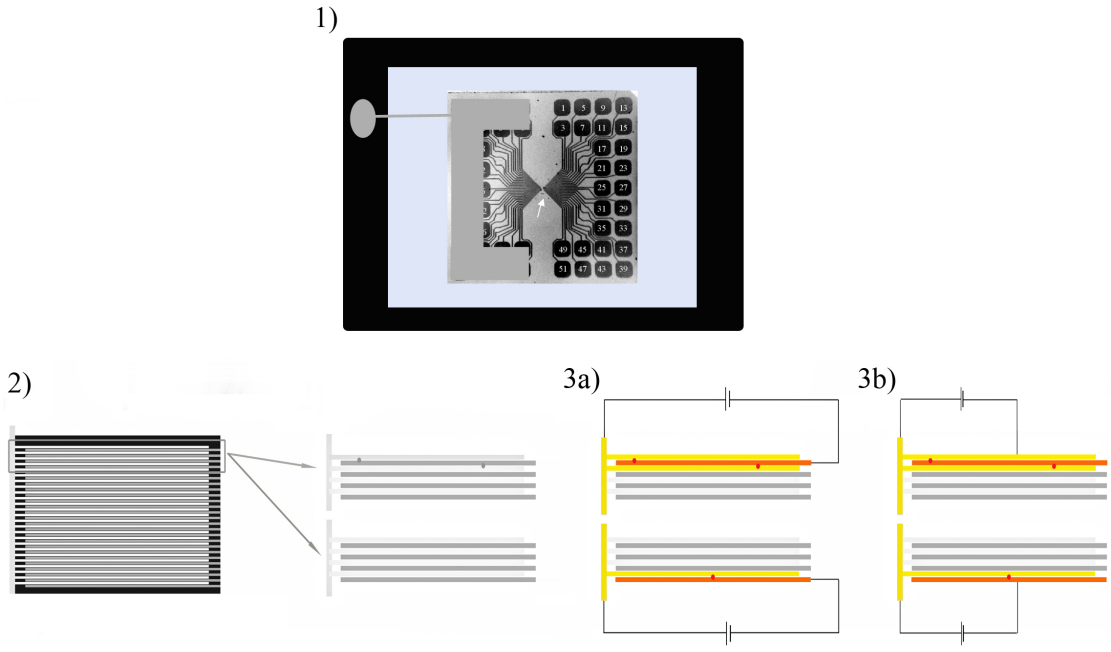

Figure 3.4.3 50nm gap electrodes. 1) Sketch of the electrode's preparation. The electrode was glued over a magnet to insulate the gate electrode and allow stabilization for C-AFM measurements. The left

side of the electrode was connected with silver paste and then on the magnet to allow bias application through that electrode. The electrodes in the devices were interdigitated and connected through nanoparticles. 2) Scheme of the interdigitated electrodes. 3a) and 4) Schematic representation of the circuit when using an electrometer to apply the bias and fingers junction to measure and when using C-AFM instead.

A series of measurements were carried out to test the reliability of the device. The characterizations allowing reliability tests of the system were morphological, to identify possible defects, as well as electrical, to evaluate the current sensitivity of the system. From a morphological stand point, the first issue faced was a fabrication issue (Figure 3.4.4). Accordingly, since the nanofabrication gave rise to defects, one of the prerequisites became the systematic check of all the electrodes before and after SAM functionalization and subsequent choice of the test-electrodes.

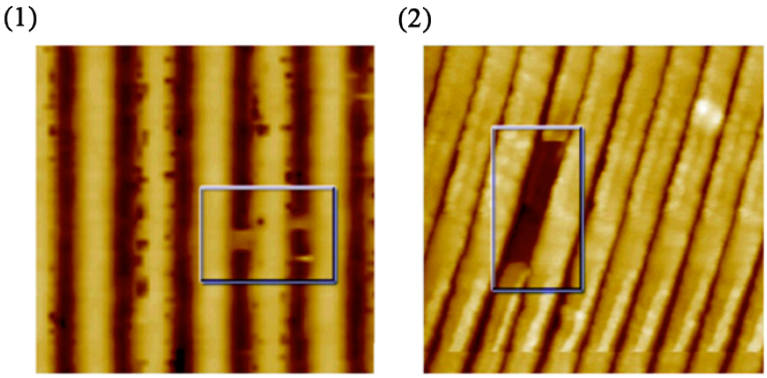

Figure 3.4.4 Two AFM images in height channel, acquired in intermitting contact mode, of two possible defects present in the nanojunctions arising from the nanojunction's fabrication. The defects are underlined by mean of a square. (1) 600 nm × 600 nm image, (2) 1 μm × 1 μm image.

From an electric point of view the leakage current of the nanojunction was tested giving a femtoamperic current in the open-gap case (Figure 3.4.5).

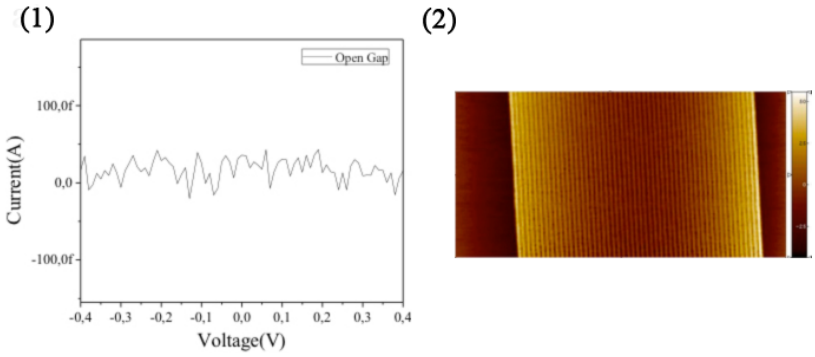

Figure 3.4.5 1) IV measurements (leakage current evaluation) and 2) AFM images of the studied nanojunctions before nanoparticles deposition, 7μm length in the x direction.

3.5 OFETs preparation and data extraction

A definition and the main physical characteristics involved in an OFET were presented in Chapter I, in the following section the preparation and data extraction will be covered. The substrates used to prepare all the OFETs presented in this thesis work were in the bottom-gate bottom-contact configuration, (Fraunhofer Institut Photonische Mikrosysteme). The gate electrode was made of n-doped silicon featuring a thermally grown 230±10 nm SiO_2 layer ($1.5x10^{-8}$ F/cm^2) and exposing pre-patterned interdigitated gold source and drain electrodes.

Each actual substrate, 15 x 15 mm^2 in size, had 16 electrodes:

4 transistors L = 2.5 µm, W = 10 mm

4 transistors L = 5 µm, W = 10 mm

4 transistors L = 10 µm, W = 10 mm

4 transistors L = 20 µm, W = 10 mm

The transistors showed a resist protection layer (AZ7217 (soluble in AZ-Thinner or acetone)) (Figure 3.5.1).

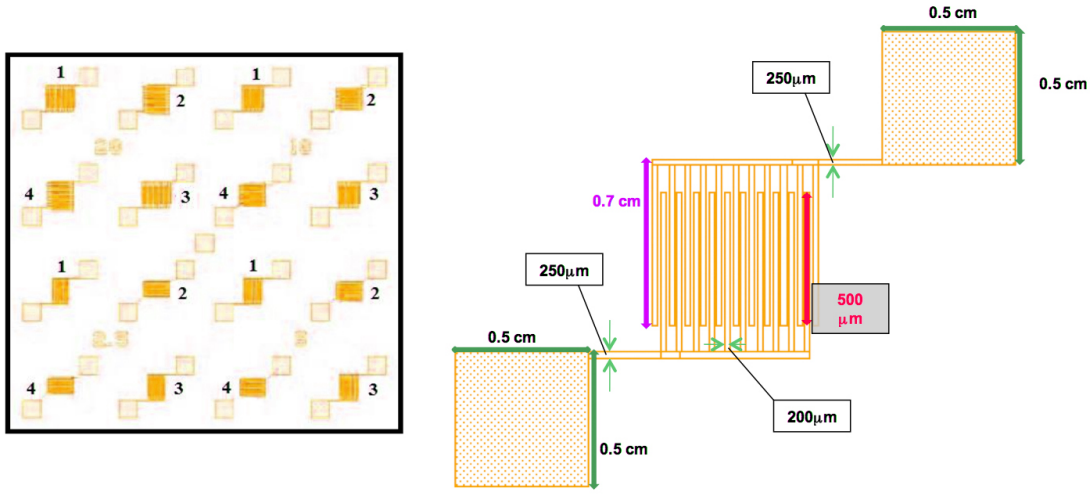

Figure 3.5.1 Left: general top view of the franunhofer patterned test electrodes, right: a single transistor layout, having a channel width of 10 mm and a channel length (length between neighbors electrodes) which varies each for electrodes.

The preparation of the OFETs was based on the following steps:

- cleaning of the protecting resistor layer via rinsing with acetone then 15 minutes in acetone in ultrasonic bath at room temperature and 15 minutes in isopropanol
- drying under nitrogen flow
- spin coating in glovebox of an homogeneous solution of semiconductor
- thermal annealing to evaporate the solvent
- measurement

For the general aspects of the measurements, such as choice of the voltages applied and steps, output and transfer characteristics and ways to extract mobility, threshold voltage and ratio between on and off current, the guidelines proposed by IEEE Computer Society were followed.[18] For the more specific characterizations of traps and photoresponsivity we relied on the available literature.

The characteristics measured were: output and transfer curves, time dependent behavior at a particular gate and drain voltage, back and forth transfer characteristics. The voltages applied were chosen considering the use of a p-type semiconductor and depending on the bias stress characteristics of the studied system. The output characteristics were obtained by sweeping the drain voltage while applying a constant gate voltage, the transfer characteristics were instead obtained by sweeping the gate while keeping the drain constant.

In the output characteristics it is possible to define three different "regimes", the linear, the non-linear and the saturation regime (Figure 3.5.2). The voltages applied to measure the transfer characteristics were chosen based on the values found in the output characteristics for each regime. Two are the drain voltages chosen and kept constant, *i.e.* one in the linear and one in the saturation regime.

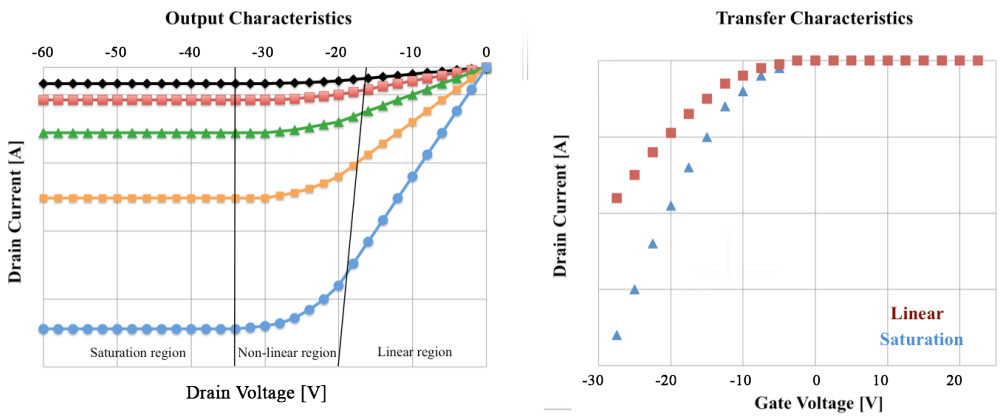

Fig. 3.5.2 Output and Transfer Characteristics for a p-type semiconductor.

The knowledge of the geometry of the device employed made it possible to extract the charge carriers mobility, the threshold voltage and the Ion/off ratio. These three physical quantities are, in the field of OFETs, interdependent through equations [18] 3.2 and 3.3, each of depends on the chosen regime.

$$I_{DS} = \mu_{LIN} \cdot C_i \cdot \frac{W}{L}[(V_{GS} - V_{TH})V_{DS}], \qquad V_{DS} \leq (V_{GS} - V_{TH}) \qquad (3.2)$$

$$I_{DS} = \frac{1}{2}\mu_{SAT} \cdot C_i \cdot \frac{W}{L}(V_{GS} - V_{TH})^2, \qquad V_{DS} \geq (V_{GS} - V_{TH}) \qquad (3.3)$$

where

I_{DS} is the corrent measured between source and drain electrodes

μ_{LIN} is the charge carriers mobility in the linear region

μ_{SAT} is the charge carriers mobility in the saturation reagion

C_i is the capacitance of the insulator/dielectric

W is width of the transistor's channel

L is the length of the transistor's channel

V_{GS} is the voltage applied between source and gate electrodes

V_{TH} is the threshold voltage

V_{DS} is the voltage applied between source and drain electrodes

To get an insight over each parameter: the IEEE Standard definitions are here presented together with the equations/ methodology to extract the different parameters.

3.5.1 Field-effect mobility

IEEE Standards[18] define the field effect mobility as the majority carrier mobility of semiconductor material derived through transfer curve measurement of the fabricated device, expressed in units cm^2/Vs. The field-effect mobility is usually derived from either saturation or linear approximations." Equations (3.4) and (3.5) present the dependences of the mobilities, in saturation and linear regime, from the device's geometry and the voltages applied.

$$\mu_{LIN,p} = \left(\frac{\partial I_D}{\partial V_G}\right)_{V_D} \cdot \left(\frac{L}{W}\right) \cdot \left(\frac{1}{C_i}\right) \cdot \left(\frac{1}{V_{DS}}\right) \qquad V_{DS} \leq (V_{GS} - V_{TH}) \qquad (3.4)$$

$$\left(\frac{\partial \sqrt{|I_{D,SAT}|}}{\partial V_G}\right)^2 = \frac{1}{2}\mu_{SAT,p} C_i \frac{W}{L} \qquad V_{DS} \geq (V_{GS} - V_{TH}) \qquad (3.5)$$

3.5.2 Threshold Voltage

IEEE Standards define the threshold voltage as the minimum gate voltage required to induce the channel. This value is obtained from a transfer (I_{DS} vs. V_{GS}) measurement.[18] It can be derived from both the linear and saturation regimes, and for a trap-free material V_{TH}, for definition, is zero.

The extraction of the V_{TH} can be done via both linear and saturation regimes. For the linear regime it is necessary to plot the $I_D V_G$ curves (Figure 3.5.3) while for the saturation regime the square root of the saturation current is plotted vs the gate current. From a theoretical point of view the behavior should be linear but since in OFETs the mobility is bias dependent and contact resistance plays a role, the output will not be linear.[19]

The scientific community has then chosen to use a linear regression of the curve centering it in the inflection point.

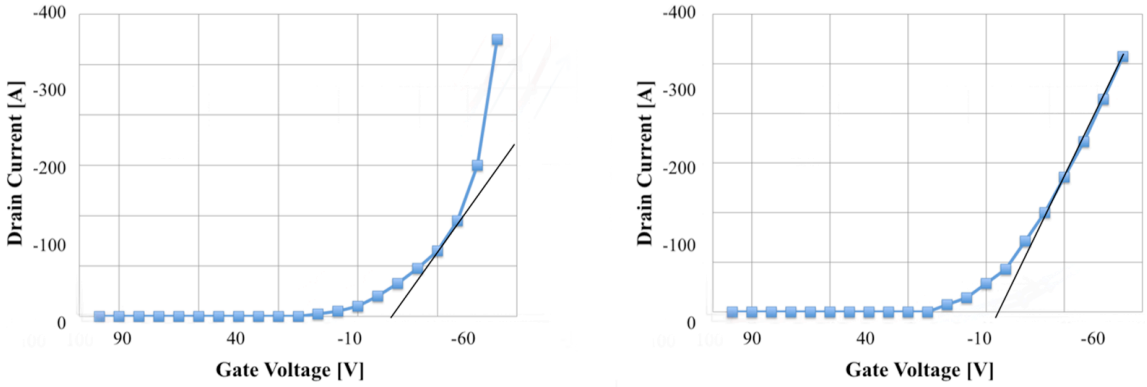

Figure 3.5.3 Two examples of transfer curves in the linear regime from which V_{TH} has to be extracted. While the extraction by interpolation of the linear zone is fairly straightforward in the right example, a really high error in the left curve might be done.

3.5.3 I_{ON}/I_{OFF} ratio

IEEE Standards[18] defines the on/off ratio as the maximum *(on)* I_{DS} value divided by the minimum *(off)* I_{DS} value, obtained from a transfer (I_{DS} vs. V_{GS}) measurement. This ratio characterizes the ability of the device to switch a signal *on* and *off* (Figure 3.5.4).

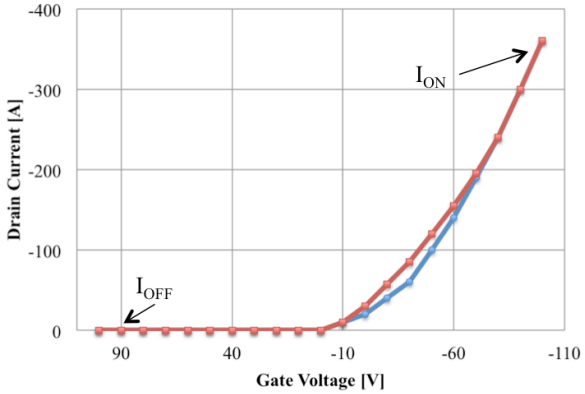

Figure 3.5.4 Example of transfer characteristics form which it is possible to extract the I_{ON}/I_{OFF} ratio.

The I_{ON}/I_{OFF} ratio can be extracted both from the output and the transfer characteristics. An inconvenient in using the output characteristics is that it is necessary to define it for a given threshold voltage and since V_{TH} can vary during measurement, it is necessary to properly define it. If the V_{TH} is instead extracted from the transfer characteristics, it is necessary to define at which voltage and in which regime the measurements were done.

3.5.4 Contacts effect

One of the most important characteristics of a device is its actual ability to inject charges between two different surfaces (for Fermi's energy, composition, etc.), which usually are a metal and a semiconductor. The contacts effect can be simply modeled as series of resistances or Schottky barriers (Figure 3.5.5.).

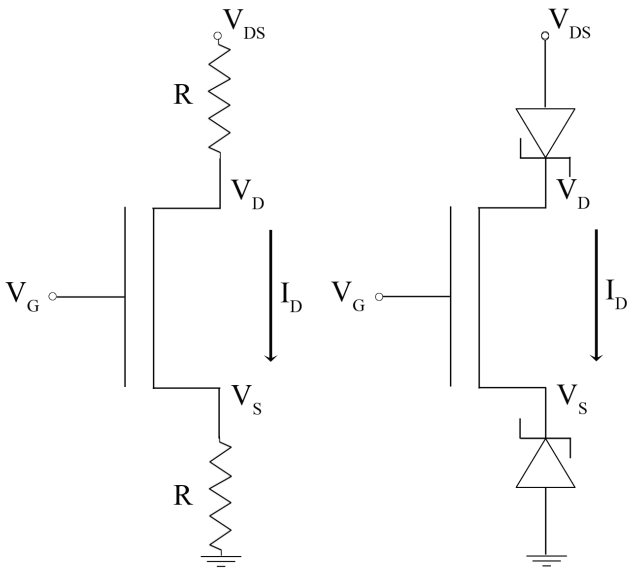

Figure 3.5.5 Sketch two of the possibilities to represent the contact effect in an OFET. Left: Series of Resistances, Right: Schottky barriers (as in diodes).

The contacts effect will get stronger as the channel length of the device gets smaller. Measuring devices with different channel length allows computing the contact effects. The most common way is the Transmission Line Method (TLM). For a certain contact width:

$$R_{tot} = R_{channel} + R_c$$

where

R_{tot} is the total resistance measured in the device

$R_{channel}$ is the Channel resistance

R_C is the contact resistance.

By plotting the width-normalized resistance versus the channel length, a linear behavior can be shown. The value at channel length equals to 0 will give the value of the contact resistance. Being the contact resistance V_G dependent it is necessary to extract for comparison at the same bias applied.

The TLM method is based on the assumption of having ohmic contacts and is not applicable if the contact resistance don't show a linear behavior. In this case the four-point probe needs to be used.[19]

3.5.5 Back&Forward I_DV_GS

A way to evaluate the amount of charges trapped in the channel is to perform transfer curves acquisition in cyclic ways, *i.e.* swiping the gate voltage from a positive maximum to a negative minimum and vice versa without stop (for p-type semiconductors). (Figure 3.5.6)

The trapping of a charge in the semiconductor will lead to an hysteresis between the back and forward curves. The hysteresis amplitude is proportional to the amount of charges trapped. The charge trapping will also influence the V_{TH} and, thus, all the others transistor's characteristics.[20]

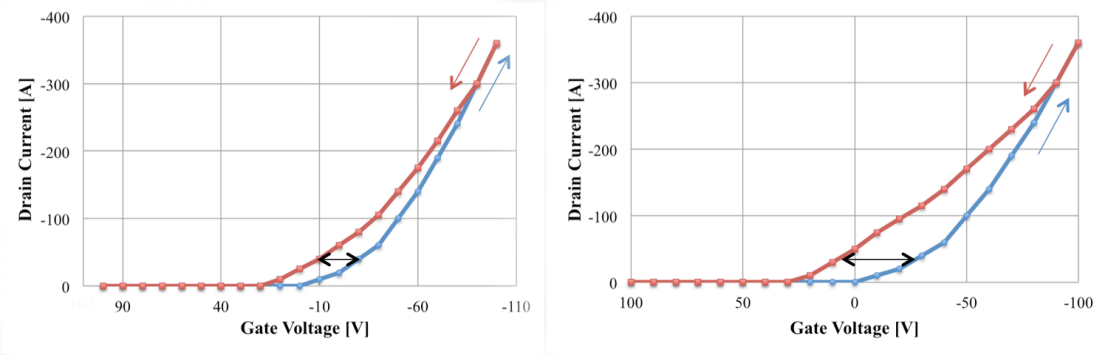

Figure 3.5.6 Back&Forward I_DV_GS for two samples having different charge trapping.

If charge trapping occurs, further characterization of the device needs to be donein order to de-trap by application, for example, of an inversed bias.

3.5.6 Time dependent acquisitions

Another interesting characterization, for instance to evaluate the bias stress (variation in measured current while applying a bias) in a device is the measurement done by applying constant bias and measuring the variation of them over time. The time-dependent acquisitions results are particularly important when applying a further impulse to modulate the charge transport or injection in the channel, for example in photoswitching (Figure 3.5.7)

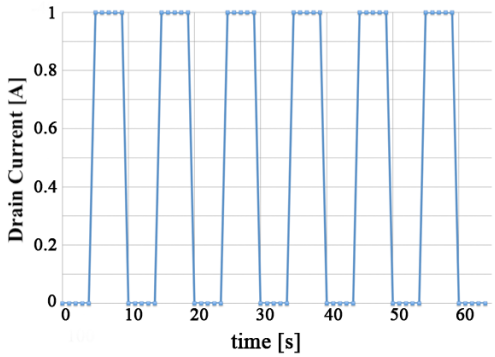

Figure 3.5.7 Time dependent Characterization of a device switching between two states 0 and 1 thanks to an external stimulus. The device is switched ON and OFF. Performing cycles of irradiation and dark allows determination of the responsivity of the system in terms of time and reliability over cycles of measurements.

Appendix

All the reagents, solvents included, except water, were purchased from Aldrich. The MilliQ water was provided in our laboratory using a MQ water filter (Millipore-Direct Q 3). The UV-Vis spectra were recorded with a Spectrophotometer UV-Vis-NIR (Shimadzu UV-3600). The irradiation lamp was a UV lamp with λ_{max} of emission centered around 366 nm (Benda NU-8 KL) 87 $\mu W/cm^2$. All the images were acquired with a FIB (model FEI Dual Beam Strata 235) equipped with a STEM detector (TEM module, FEI).

For the preparation of the 100 nm gap nanotrenches electrodes, a class 1000 cleanroom (class 100 for the lithography section) equipped with an MJB4 (SUSS MicroTec) mask aligner, an electron beam evaporator, MEB 550S (PLASSYS), for metallic deposition and several optical microscopes for inspection, was used.

Oxidized silicon wafer were bought from *Si-Mat*[2] while glass and quartz substrates from *Emsdiasum*[21]. For the preparation of the 50 nm gap nanoelectrodes a Class 10-100 cleanroom equipped with an e-beam evaporator was employed for all the process.

The 80 nm gold nanoparticles were bought from Sigma-Aldrich and featured a citrate coating layer and a concentration equals to 7.9E9 particles/mL.

The half-coated microspheres were prepared starting with Sicastar®Monodisperse silica Microspheres with mean diameter ranging from 100 nm to 1.00 μm (Micromod) and Polystyrene monodisperese microspheres (Polysciences) mean diameter 1.00 μm.

^{1}H-NMR spectra were recorded on Bruker Advance 400 (400.14 MHz).

The substrates used to prepare all the OFETs presented in this thesis work were in the bottom-gate bottom-contact configuration, (Fraunhofer Institut Photonische Mikrosysteme). The gate electrode was made of n-doped silicon featuring a thermally grown 230±10 nm SiO_2 layer ($1.5x10^{-8}$ F/cm^2) and exposing pre-patterned interdigitated gold source and drain electrodes.

A Keithley 2536 electrometer interfaced by in-house developed software was employed for the electrical measurements.

All the AFM images were acquired in intermittent-contact (tapping) mode under ambient conditions by employing a Digital Instruments Dimension 3100 AFM equipped with a Nanoscope IV controller. The chosen cantilevers were standard silicon with a nominal force constant of 40N/m (Veeco MPP-11120).

The glovebox employed had water and oxygen levels below 10ppm.

References

1 Ruiz, F., Prats, D. & Gomis, V. Quaternary liquid-liquid equilibrium: water-ethanol-chloroform-toluene at 25.degree.C. Experimental determination and graphical and analytical correlation of equilibrium data. *Journal of Chemical & Engineering Data* **30**, 412-416 (1985).

2 Tarbell, D. S. & Harnish, D. P. Cleavage of the Carbon-Sulfur Bond in Divalent Sulfur Compounds. *Chemical Reviews* **49**, 1-90 (1951).

3 Schreiber, F. Structure and growth of self-assembling monolayers. *Progress in Surface Science* **65**, 151-256 (2000).

4 Love, J. C., Estroff, L. A., Kriebel, J. K., Nuzzo, R. G. & Whitesides, G. M. Self-assembled monolayers of thiolates on metals as a form of nanotechnology. *Chemical Reviews* **105**, 1103-1169 (2005).

5 Leff, D. V., Brandt, L. & Heath, J. R. Synthesis and characterization of hydrophobic, organically-soluble gold nanocrystals functionalized with primary amines. *Langmuir* **12**, 4723-4730 (1996).

6 Kimling, J. *et al.* Turkevich method for gold nanoparticle synthesis revisited. *Journal of Physical Chemistry B* **110**, 15700-15707 (2006).

7 Turkevich, J., Stevenson, P. C. & Hillier, J. A study of the nucleation and growth processes in the synthesis of colloidal gold *Discussion of the Faraday Society* **11**, 55-75 (1951).

8 Bauer, C. A., Stellacci, F. & Perry, J. W. Relationship between structure and solubility of thiol-protected silver nanoparticles and assemblies. *Topics in Catalysis* **47**, 32-41 (2008).

9 Roldan, M. V., Scaffardi, L. B., de Sanctis, O. & Pellegri, N. Optical properties and extinction spectroscopy to characterize the synthesis of amine capped silver nanoparticles. *Materials Chemistry and Physics* **112**, 984-990 (2008).

10 Yong, K. T., Swihart, M. T., Ding, H. & Prasad, P. N. Preparation of Gold Nanoparticles and their Applications in Anisotropic Nanoparticle Synthesis and Bioimaging. *Plasmonics* **4**, 79-93 (2009).

11 Kassam, A., Bremner, G., Clark, B., Ulibarri, G. & Lennox, R. B. Place exchange reactions of alkyl thiols on gold nanoparticles. *Journal of the American Chemical Society* **128**, 3476-3477 (2006).

12 Ohyama, J., Hitomi, Y., Higuchi, Y. & Tanaka, T. Size Controlled Synthesis of Gold Nanoparticles by Porphyrin with Four Sulfur Atoms. *Topics in Catalysis* **52**, 852-859 (2009).

13 Dayen, J. F. *et al.* Nanotrench for nano and microparticle electrical interconnects. *Nanotechnology* **21** (2010).

14 Cho, J. H. *et al.* Printable ion-gel gate dielectrics for low-voltage polymer thin-film transistors on plastic. *Nature Materials* **7**, 900-906 (2008).

15 Love, J. C., Gates, B. D., Wolfe, D. B., Paul, K. E. & Whitesides, G. M. Fabrication and wetting properties of metallic half-shells with submicron diameters. *Nano Letters* **2**, 891-894 (2002).

16 Long, D. P. *et al.* Magnetic directed assembly of molecular junctions. *Applied Physics Letters* **8** (2005).

17 Chu, C. W., Na, J. S. & Parsons, G. N. Conductivity in alkylamine/gold and alkanethiol/gold molecular junctions measured in molecule/nanoparticle/molecule bridges and conducting probe structures. *Journal of the American Chemical Society* **129**, 2287-2296 (2007).

18 Board, I. S. IEEE Standard for Test Methods for the Characterization of Organic Transistors and Materials. *IEEE Standards* (2008).

19 Bao, Z. & Locklin, J. Organic Field-Effect Transistors. *CRC Press* (2007).

20 Singh, B., Marjanovic, N., Sariciftci, N. S., Schwodiauer, R. & Bauer, S. Electrical characteristics of metal-insulator-semiconductor diodes and transistors with space charge electret insulators: Towards nonvolatile organic memories. *Ieee Transactions on Dielectrics and Electrical Insulation* **13**, 1082-1086 (2006).

21 http://emsdiasum.com.

Chapter 4. NP aggregation, kinetics and SERS

4.1.1 Reversible solvation of nanoparticles– aim of the project and experimental evidence

The aim of the project was to build the means to couple the photoswitching properties of azobenzene moieties with the size-dependent properties of noble metal nanoparticles (synthesized as presented in Chapter 3).

Studying the system it was possible to achieve reversible modulation of the nanoparticles' solubility in an organic medium (toluene) via application of photochemical stimulus.

Three different azobenzene-modified nanoparticle sizes were prepared in order to explore the size-dependent properties and elect the best system: 3, 15 and 25 nm in diameter (named AZOAuNP1, AZOAuNP2 and AZOAuNP3, respectively).

The nanoparticles, when suspended in toluene solution were found to be tunable between two different physical states, one featuring large aggregation and a second one exhibiting a colloidal dispersion. This modulation was found to be dependent on the isomerization of the azobenzene, i.e. when irradiating with UV light the *trans*-azobenzene isomerized to the *cis*-form, and the nanoparticles were dispersed in the toluene solution. When the solution was kept in dark so that the azobenzenes

thermally isomerized back to the *trans*-configuration, large precipitates formed once more. Figure 4.1.1 shows a toluene solution of AZOAuNP3 following 366 nm or 450 nm irradiation.

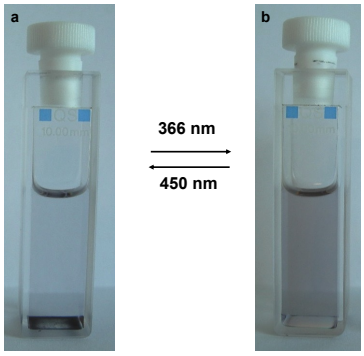

Fig. 4.1.1 Photo-modulated transition of AZOAuNP3 from (a) solid precipitate to (b) a colloidal solution in toluene.

By successive stepwise irradiation with UV and visible light (or dark) a cyclable solvation-precipitation phenomenon was demonstrated.

To gain insight into the mechanism of the solvation-precipitation process, UV-Vis and ^{1}H-NMR spectra of the nanoparticles before and after substitution were acquired.

The UV-Vis spectra were acquired between 290 and 850nm, with 1nm resolution for a total acquisition time of 40 seconds to avoid significant changes in precipitation during measurement. Figure 4.1.2 shows the spectra of the nanoparticles before and after substitution with azobenzene, the main differences being a strong redshift of the SPR, evidence of nanoparticle aggregation, and an increase in absorption around 365nm due to the presence of azobenzene moieties.

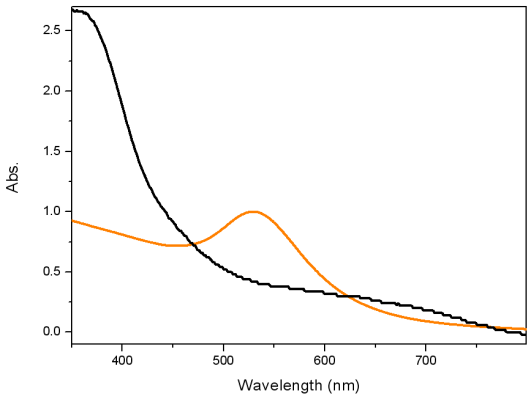

Figure 4.1.2 UV-Vis spectra of AuNP3 before (orange line) and after (black line) substitution with azobenzene (AZOAuNP3).

To understand the mechanism behind and prove the reversibility of the process, UV-Vis spectra were acquired before and after irradiation.

Figure 4.1.3, for example, shows the spectra of AZOAuNP3 over an irradiation cycle: in the acquired spectra, there were two main differences before and after irradiation at 365 nm: a decrease of the band around 365nm and a blue-shift of the surface plasmon resonance of the nanoparticles.

Small peaks in the near IR region, i.e. around 800 nm, are also visible but cannot be unambiguously ascribed to any specific species except the presence of a distribution of aggregates.

Typically, a decrease of the UV-Vis signal at around 365nm is indicative of *trans*- to *cis*- isomerisation in azobenzenes systems while a red-shift of the SPR band of nanoparticles indicates aggregation and the subsequent coupling of SPRs on different nanoparticles.[1-10]

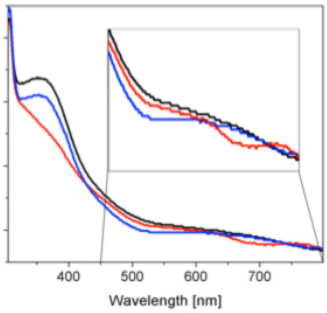

Fig. 4.1.3 UV-Vis spectra of the AZONP3 sample upon irradiation: *black line*, before irradiation; *red line*, after irradiation with UV light at 366 nm; *blue line*, after irradiation with visible light at 450 nm.

The same experiments were performed for AZOAuNP1 and AZOAuNP2, with similar results as for AZOAuNP3, (with shifts in the spectra depending on the NP size). Figure 4.1.4 shows the spectra obtained for the other nanoparticles samples under the same conditions as Figure 4.1.3. For the smaller sized NPs, the evidence of the aggregation-solvation process is less pronounced, maybe due to lower efficiency of SPR coupling between adjacent nanoparticles because of dimensionality issues. The coupling depends not only on the distance between the nanoparticles but also on their size.[11] The different UV-Vis behaviour of AZOAuNP2 was attributed to the fact that it was then only sample which precursor (before ligand exchange reaction) was in water. It was then decided to synthesize all the nanoparticles in the same solvent, *i.e.* toluene.

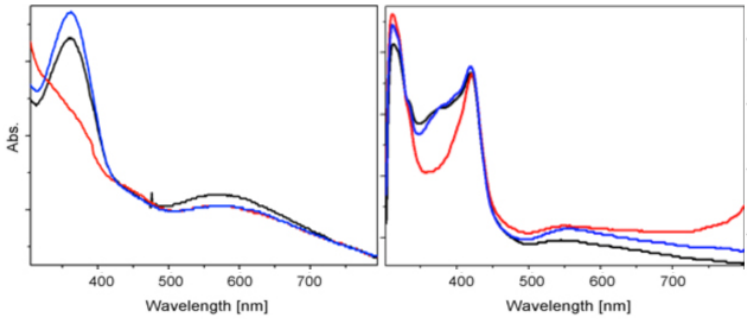

Fig. 4.1.4 UV-Vis spectra of the AZONPs sample upon irradiation: *black line*, before irradiation; *red line*, after irradiation with UV light at 366 nm; *blue line*, after irradiation with visible light at 450 nm. a) AZOAuNP1, b) AZOAuNP2.

Evidence of both the quasi-monodisperse nature of the gold nanoparticles that have been synthesised (Fig. 4.1.5 a), and of the aggregation change as a result of photo-isomerization were obtained by electron microscopy imaging (Fig. 4.1.5b,c) for the 25 nm NP sample. A STEM microscope was employed to take images of the nanoparticles before and after the ligand-exchange reaction and UV irradiation. These measurements provided direct and unambiguous evidence for the monodisperse character of the as-synthesized AuNPs (Fig. 4.1.4a), and for the photo-triggered aggregation-solvation (Fig. 4.1.4b and 4.1.4c, respectively). On the several tens of microns scale the films obtained by spin-coating AZOAuNP3 in the *trans* form are very inhomogeneous, exhibiting uncoated areas and large 3D aggregates (see Fig. 4.1.4b). Conversely, on the same scale the naked AuNP3 (Fig. 4.1.4a) and the films of *cis*-AZOAuNP3 are homogeneous. These differences cannot be ascribed to the concentration of the solution applied to the substrate, which was identical.

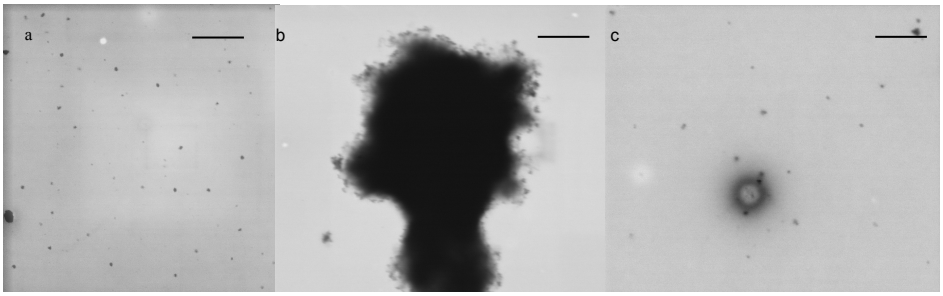

Fig. 4.1.5 STEM images of the AuNP3 (a) before substitution with AZO molecules. AZOAuNP3 (b) in the *trans*-form, (c) in the *cis*-form as obtained upon UV-light irradiation of the sample in (b). The scale bar in the pictures corresponds to 1μm length.

The general applicability of this light modulated aggregation-solvation was established by TEM studies of the smaller sized gold nanoparticles, i.e. AZOAuNP1 and AZOAuNP2. Figure 4.1.6 shows the TEM images for smaller nanoparticles as proof that even if the spectroscopic evidence for photo-triggered aggregation-solvation was less pronounced for the smaller NPs, it certainly still occurs.

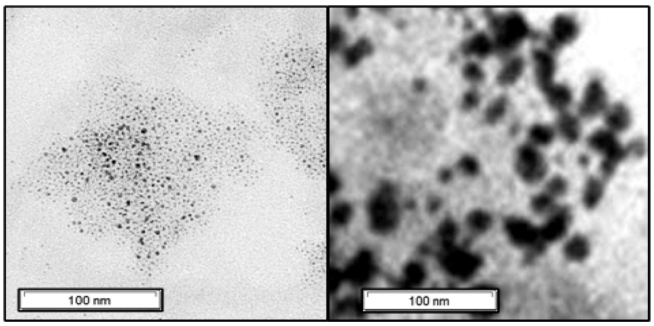

Fig. 4.1.6 TEM images of the AZOAuNP1 in the *cis*-form on the left, as obtained upon UV-light irradiation of the sample in the *trans*-form, showed at the right in the picture.

It was proposed that interdigitation of the NP surface-bound AZO units when in their *trans*-form drives the light-induced aggregation-solvation behaviour.

4.1.2 Conclusions and Remarks

In summary, isomerization of fully conjugated azobenzenes directly absorbed on gold nanoparticles was achieved and optical and reversible modulation of the solvation and precipitation of Au nanoparticles was shown.

The first discovery is particularly important since many recent works report the non-switchability of azobenzene when absorbed on gold nanoparticles without spacing units.[12] The explanation usually given is that the excited states of azobenzene are quenched, resulting in no photoisomerization.

The second discovery is similar to that reported by Grzybowski *et al* in which the light modulated aggregation of metallic nanoparticles coated with a mixed SAM of a dodecylamine and azobenzenes (functionalized with a thiol anchoring group at the end of a flexible undecanoxy side-chain) was shown to be reversible. In that case however, it was the *cis*-isomer that formed aggregates through dipole-dipole interactions.[13]

In order to gain a deeper understanding of the aggregation-solvation behavior in the AZOAuNP systems, a thorough analysis of the kinetics of the process was undertaken as presented in the next section.

4.2.1 Kinetic treatment of nanoparticle aggregation – Aims and presentation of the system

The two main goals of this project were: gaining a deeper understanding of both the aggregation process[14] and of the four-fold higher thermal stability of the *cis* isomer when absorbed as a SAM on a substrate rather than in solution.[15] It has been proposed that the higher stability of the SAM is due to collective behavior of neighboring azobenzene moieties when pi-stacked.[15] Chapters 1 and 3 present a summary of the work involving AZO molecules to date.

Grzybowski *et al* recently reported controlling SAM properties by controlling the nanoparticles size, i.e. the curvature of the surface.[16] Unfortunately our case is more complicated since the fully conjugated nature of the AZO SAM and the shorter size of the molecules means they are better able to follow the real nanoparticle surface by forming a tightly packed SAM.

The first challenge was the determination of a model that could properly describe the real geometry of the SAM. It was chosen to employ two different sizes of nanoparticles, 3 and 15nm (synthesized as presented in Chapter 3). The employed nanoparticles will be called AZOAuNP1 and AZOAuNP2 and will be synthesized starting from alkylamine precursors of the stated size then substituted with AZO and dispersed in toluene.

As reported by several groups and due to the nanoparticles' growth mechanism (explained in Chapter 2), the real geometric shape of the nanoparticles is not spherical.[17-19]

Figure 4.2.1 presents a sketch of the nanoparticles used in this study coated with AZO molecules, the assembly of the moieties and the areas of the domains is pictured dependent on the NPs size as confirmed by the underlying structure of the nanoparticle and the ^{1}H-NMR analysis (Figure 4.2.2). In fact a variation in the chemical shift of azobenzenes coating different nanoparticles sizes confirm the dissimilar chemical environments, i.e. the different packing.

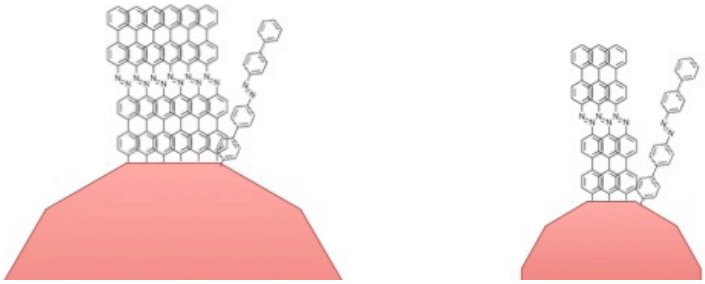

Figure 4.2.1 Sketch of the shape of the nanoparticles employed in kinetic studies. At the left 15 nm gold nanoparticles and at the right 3 nm gold nanoparticles.

Both the nanoparticle samples show different features in the aromatic region when compared with the pure molecules most probably due to the adsorption on the nanoparticles. The difference is already visible in the NMR spectra for the *trans*-form with the presence of three additional peaks, but better insight is gained after irradiating the samples (Figure 4.2. (b)). New peaks appear for the *cis*-form proving the isomerization of AZO when absorbed on AuNPs.

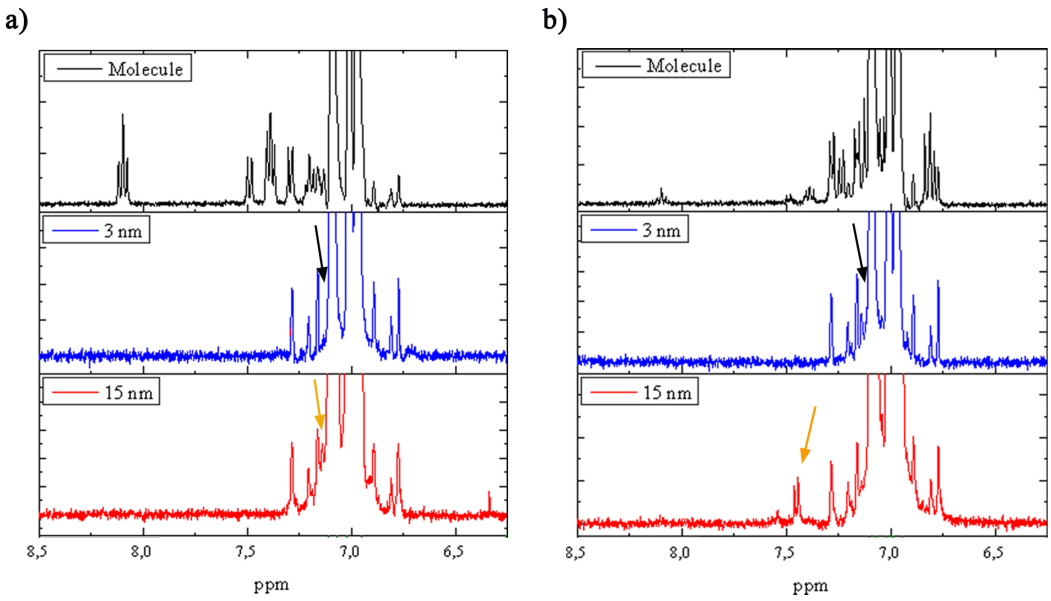

Figure 4.2.2 ^{1}H-NMR spectra of the azobenzene molecules and the nanoparticles employed in kinetic studies. From top to bottom: azobenzene, 3 nm particles (AZOAuNP1) and 15 nm particles (AZOAuNP2). *Trans* isomer (a) and *cis* isomer (b). The arrows indicate peaks shifting by tuning the nanoparticles size.

While for the azobenzene molecules clear peak assignment is possible (as presented in Chapter 3), for the nanoparticles it is only possible to state that the peaks

visible in the aromatic region are ascribable to the aromatic hydrogens of the azobenzene adsorbed on the nanoparticles.

To perform a kinetic study of reversible solvation, a concrete normalization model to obtain reliable results needs to be carefully studied.

It is possible to postulate, from the data obtained from the aggregation/solvation process of the nanoparticles, that the overall reaction is describable as in equation 4.1.

$$Trans \underset{\leftarrow}{\overset{\rightarrow}{}} Intermediate \underset{\leftarrow}{\overset{\rightarrow}{}} Cis \qquad (4.1)$$

Where: *Trans* is the *trans* isomer after synthesis, in solid physical state, and *cis* is the *cis* isomer after irradiation, with colloidal solution as physical state. The presence of an intermediate state is postulated as a first approximation. During isomerization, in fact, three spectra components with characteristics peaks were found in every case: one ascribable to the *trans*, one to the *cis* and one to a third state.

Following this approximation a kinetic treatment for consecutive and reversible reactions need to be employed.[20]

The project involved nanoparticles that were fully aggregated after synthesis; consequently one of the initial challenges was to evaluate the starting concentrations of the samples. As pi-stacking between azobenzene moieties is tunable with temperature (T), it was decided to first increase the T to 95-100°C to ensure complete dissolution of the as-synthesized *trans*-AZOAuNPs. Then, to aid comparisons in the same concentration range, the samples were diluted to get the absorbance at 365nm equal between them.

Figure 4.2.3 presents AZOAuNP1 UV-Vis spectra at different temperatures. AZOAuNP2 samples behaved in the same way.

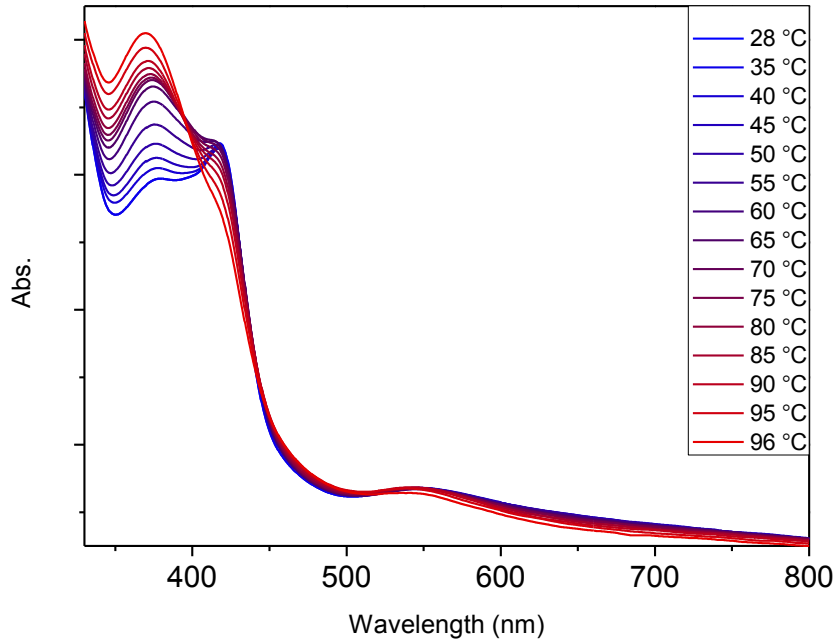

Fig. 4.2.3 General UV-Vis Spectrum obtained by increasing the T between 28 and 96°C. Absorbance scale is not displayed because it depends on the particular sample and concentration considered.

Both ^{1}H-NMR and UV-Vis techniques were employed in kinetic studies. The UV- Vis technique allows one to monitor the NP SPR while irradiating, but information regarding the AZO moieties is less straightforward since the peaks ascribable to the AZO in the *trans* and *cis* configuration overlap. On the other hand, the ^{1}H-NMR technique allows (at least for the molecules in solution) the monitoring of the AZO isomers separately but cannot give information on the NP SPR. As seen in Figure 4.2.2, however, the spectra of the different nanoparticles depended drastically on their sizes and no isolated peaks for the smaller particles were obtained.

It was thus decided to evaluate the kinetic rate constants via UV-Vis, taking into account the intrinsic error of the technique and the necessary normalizations.

The time required for the acquisition of each spectrum, at the chosen concentrations, was on the order of 3 minutes.

A typical series of spectra obtained monitoring AZOAuNPs via UV-Vis after irradiation, is shown in figure 4.2.4. All the nanoparticles samples showed similar behavior.

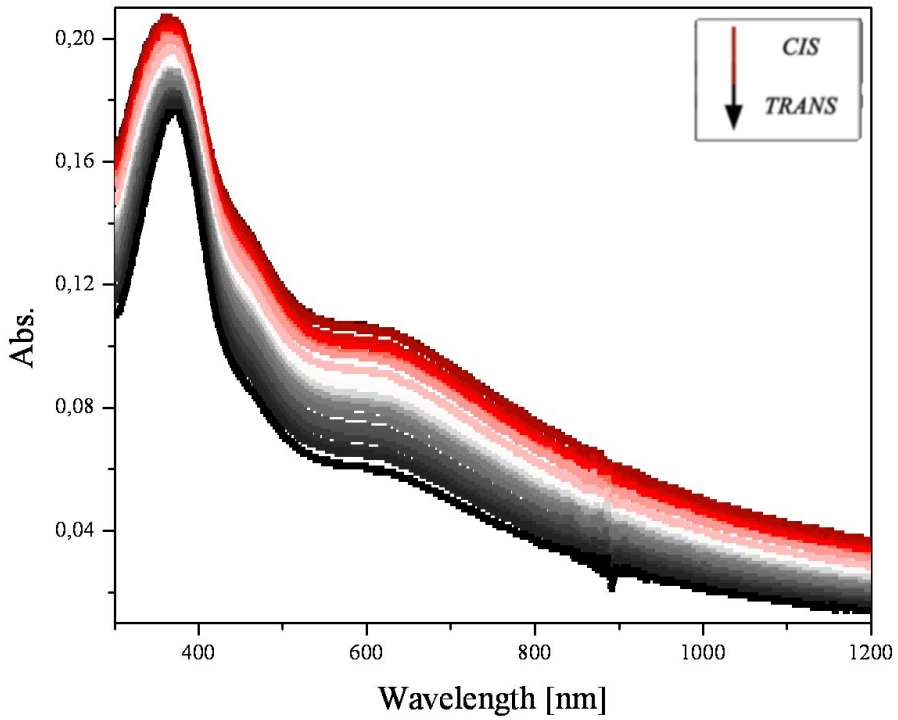

Figure 4.2.4 Series of spectra obtained, leaving an irradiate sample in dark, i.e. allowing the azo moieties to isomerize from the *cis* to the thermodynamically more stable *trans*. No normalization have been performed on these spectra.

The main features in the spectra are the decreasing absorbance around 1200, 600 and 365 nm, together with a red-shift of the peak at 365 nm (between 345 and 375nm) and a blue-shift of the peak at 600 nm (between 510 and 610nm). This is the exact opposite behavior to when UV irradiation is applied. The peak at ~365 nm is ascribable to the AZO moieties while the band at ~600nm to the SPR of the gold nanoparticles and the absorbance around 1200nm to the light scattering of large aggregates.

To be able to understand the behavior of the nanoparticles in solution and obtain kinetic data, 32 samples were prepared and fully characterized.

Since not only a variation in absorbance but also a shift in λ_{MAX} is observed during the reversible solvation process, normalizations of the curves need to be considered.

4.2.2 SPR - first experimental evidences and choice of the kinetic system

The processes involved in the first part of the reaction, going from the solid nanoparticles to the intermediate state, are based on the aggregation/solvation

behavior of the nanoparticles and are directly relatable to the behavior of the SPR. Hence, the aggregation-solvation rate could be studied evaluating the changes in the SPR of the nanoparticles with irradiation. The scattering absorbance at ~1200nm could be taken into account for this computation too, but being less sensitive than the SPR it was decided to base all the following studies on the variation of the SPR prior normalizing at 1200nm.

Regarding the first reaction from the *trans* to the intermediate state: Figure 4.2.5 presents the variation of the spectra while irradiating of AZOAuNPs immediately after synthesis and purification. Irradiation cycles of 1h were applied. As shown the absorbance of the first peak increases and blue-shifts, changes that are reversed in the dark. This behavior is more evident in samples just prepared than after cycles of irradiation. The peak obtained in this way represents the maximum *cis* concentration obtained in all the other cycles.

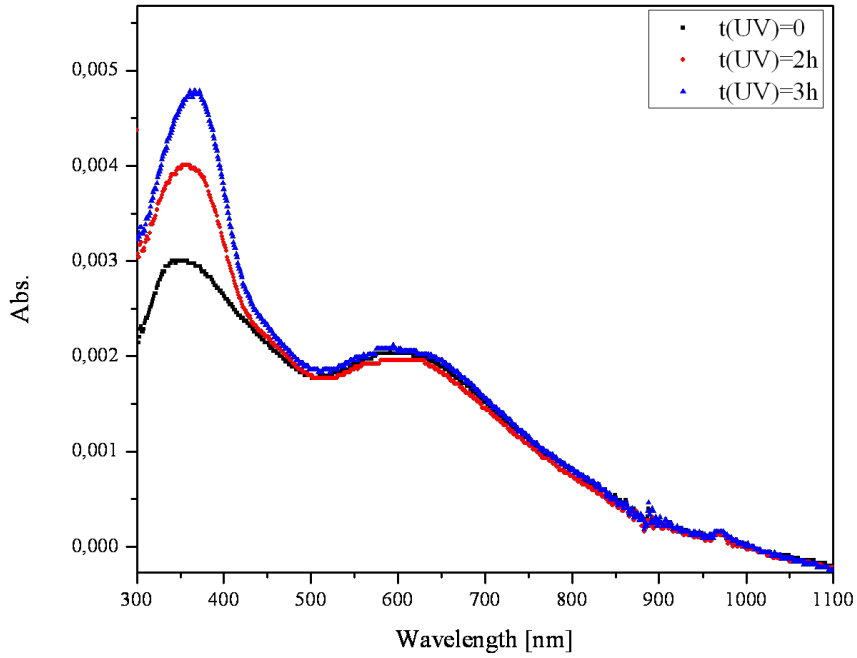

Figure 4.2.5 Illustrative UV-Vis spectra of the freshly synthesized azobenzene coated gold nanoparticles in black just after synthesis, in red after 2h of UV irradiation and in blue after 3h of UV irradiation.

Unfortunately, the spectral variation is clearly visible only for the first cycle, the behavior strongly depends on the number of irradiation cycles used, and also the time of irradiation required to obtain a specific *cis* concentration differed from sample to sample. This is not surprising given the heterogeneous nature of NP samples, and meant that no clear kinetic constant determination was possible.

Moreover, it is not possible to unequivocally identify if the intermediate state is in the *trans* or *cis* form, however as it has exactly the same characteristics as the *cis* in all the other cycles it is possible to hypothesize that it is the *cis* isomer.

Assuming that to be the *cis* isomer it is anyway not clear why the *trans* spectrum has two possible spectra, i.e. the black line spectrum in Figure 4.2.5 and then a spectrum having higher absorbance than the *cis*, as typical in azobenzene's systems. Being the presence of the first *trans* state only visible over the first irradiation cycle, and since from then on the system showed only two states (*cis* and *trans*) it was decided to consider the kinetics as shown in Equation 4.2.

$$Trans \underset{k2}{\overset{k1}{\rightleftarrows}} Cis \qquad (4.2)$$

No intermediate is considered and only a k_1 from the *trans* state to the *cis* and k_2, the rate constant for the reverse reaction need to be computed. In this case the equations for reversible first order reaction are going to be employed.[20] Firstly, to avoid the complications of the behavior under irradiation, the reaction was monitored in the dark.

4.2.3 Experimental evidences and data treatment to extract the precipitation kinetic constant

As the isomerization and precipitation processes occur simultaneously it is necessary to understand the kinetics of decrease in the area under the SPR. This data can be then compared with the kinetic constant found for the AZO molecule via ^{1}H-NMR in order to get insight over the precipitation mechanism.

It should be noted that UV light does not affect the SPR when no AZO is absorbed on the surface of the nanoparticles.

Each spectrum acquired could be fitted by a minimum of three components, peaking at: ~365nm, ~450nm and ~600nm, corresponding respectively to the main absorption peaks of the AZO in the *trans* and *cis* configuration and the SPR (Figure 4.2.6).

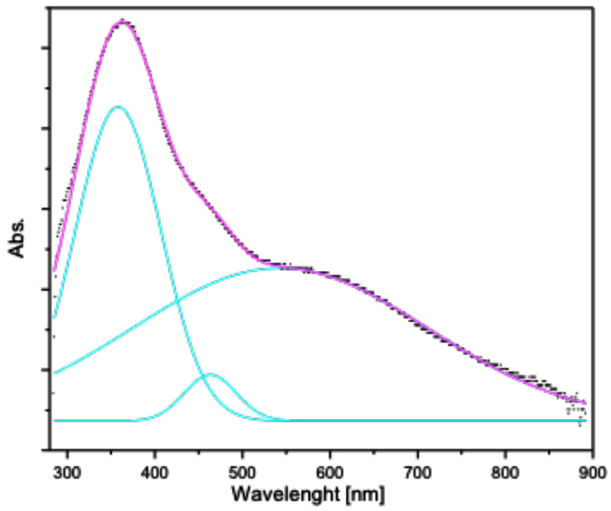

Figure 4.2.6 Peaks fitting of a typical spectrum of gold nanoparticles coated with azobenzene moieties, three peaks are underlined at 365, 450 and 600nm.

Once the fitting of the SPR is done, it is possible to extract the relative concentrations of each component as a function of time, considering first order kinetics who doesn't necessary complete, i.e. between a postulated starting and ending point. Given that the system has several competing pathways, a full kinetic analysis is very difficult. To try to isolate a simple process it was decided to pump the system as much as possible to the *cis* form such that the kinetic at early-times, could show a linear behavior. This assumption seems valid for the first minutes; it is in fact possible to extract a linear behavior from the data (Figure 4.2.7).

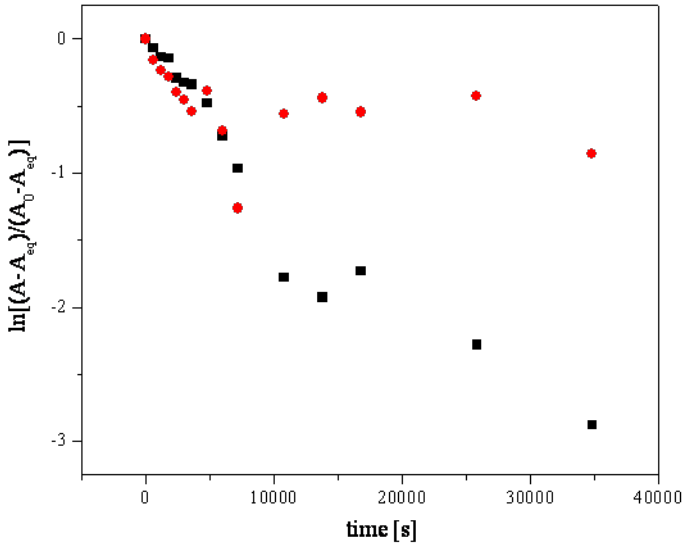

Figure 4.2.7 Logarithm of the integral of the SPR versus time for the two sizes considered, in black 15nm size particles and in red the 3nm ones for the *cis* to *trans* isomerization.

It can be seen that for the first 10 minutes the two systems show similar behavior while when the time in dark increase the kinetics of the processes show different behavior with the bigger particles showing a rather linear behavior over all the time while the smaller ones showing non-linear behavior.

Two are the possible approaches, which in this case give opposite behavior, *i.e.* considering the early stage kinetic, and obtaining an higher kinetic constant for the smaller nanoparticles compared to the bigger, or the overall process, and obtaining opposite trend.

By considering the early stage a smaller error over the fitting results but also smaller representativity of the overall process. Since for practical porpoises, when employing the nanoparticles, the time required for measurements, sample preparation, etc. normally exceed the first 10 minutes, we choose to consider the overall process, by computing the error both due to the fitting and to the repetition of the measurements. The bigger nanoparticles show a higher precipitation kinetic constant compared with the smaller ones, even if it is important to consider the fitting error on the smaller ones.

Once we have obtained information about the precipitation kinetics it was possible to proceed on the kinetic of isomerization.

4.2.4 Experimental evidences and data treatment to extract the isomerization kinetic constant

Being the kinetics of the precipitation process different, depending on the nanoparticles' size, another important normalization needs to be done at 600nm[21]. Normalizing for the integral of the surface plasmon resonance allows comparison of equal amount of AZO on the surface granting an accurate determination of the *cis* to *trans* ratio in the system.

Figure 4.2.8 shows, as an example, a set of spectra after normalization.

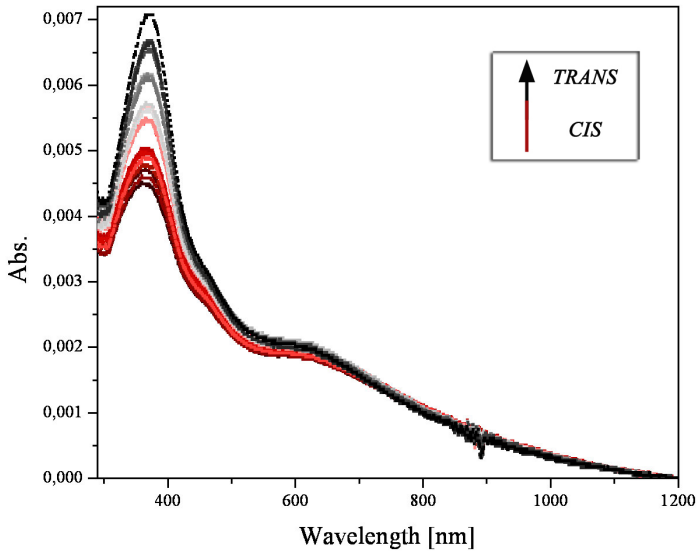

Figure 4.2.8 Typical spectra of an irradiated sample in dark after scattering and SPR normalization.

From the absorbance at the maximum wavelength of the *trans*, which changes from sample to sample, and through subtraction of the absorbance of the SPR at the same wavelength and via kinetic extraction, plotting and characterization, it was possible to obtain the different logarithm of the concentrations versus time graphs.

Treating with a system subject to physical state variation means adding uncertainty to the problem. While irradiating, it is possible that the nanoparticles more external in the aggregates will be the ones that disaggregate first, but it is not possible to avoid considering that smaller aggregates can detach all together from the biggest ones, causing higher variation of the spectra and in more position. The same phenomenon, but involving aggregation steps, can occur when the reversed isomerization is considered. The treating of k_2, following the previous statement becomes easier because the information regarding the different aggregates present in the optical pathway are considered by normalization of the SPR (Figure 4.2.9).

As for the case of the precipitation kinetics even here the early stage regime shows a different behavior compared with the overall process, even if the trend with the size is consistent over all the process. As in that case the overall process was chosen in order to take into account the variability of the system as well and because more representative of all the stages and the complexity of the system.

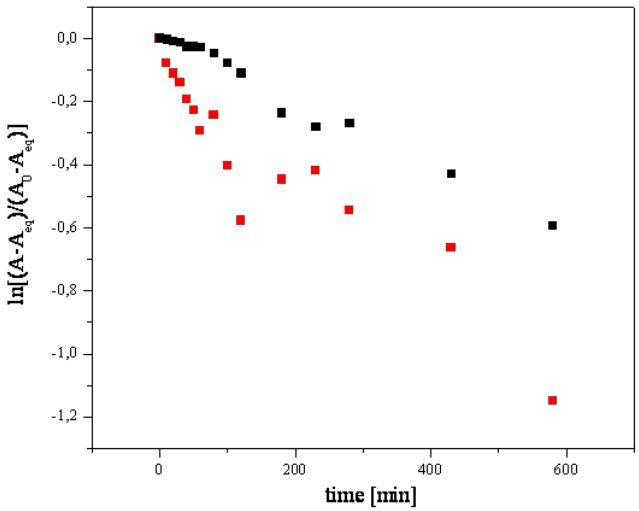

Figure 4.2.9 Logarithm of the normalized concentration versus time of irradiates samples kept in dark, for the different systems considered. In red the 3nm nanoparticles and in black the 15 nm ones.

Figure 4.2.10 presents the comparison between the obtained data with the ones obtained in the case of a SAM absorbed on flat gold. Higher variability was found for the azobenzene absorbed on flat gold and for the smaller gold nanoparticles considered due, in the first case, to the smaller concentration of azobenzene in the optical pathway giving higher variability from measurement to measurement, and in the second case, to the high heterogeneity of the system. The error presented takes into account both the error between different samples and the fitting error.

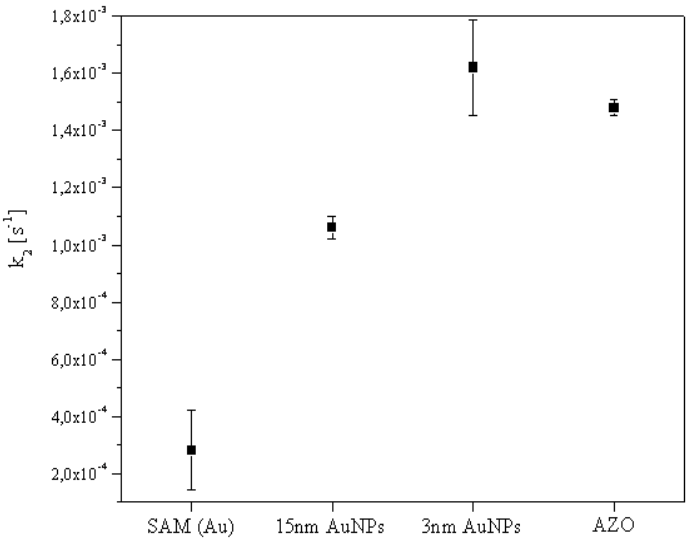

Figure 4.2.10 Comparison between the k_2 obtained for a SAM on gold, a 15nm gold nanoparticle, a 3nm gold nanoparticle and azobenzene in solution.

The graph reveals a trend in the kinetic constant with respect to the curvature of the nanoparticles, or more accurately, with the size of the domains and so the degree of pi-stacking between the azobenzene moieties. This proves that the higher thermal stability of the *cis* form for the SAM absorbed on flat surfaces can be attributed to the intrinsic nature of the molecules involved and most likely to the pi-stacking between them. It is also important to notice an opposite trend, between different sizes nanoparticles for what concern the precipitation kinetics. This opposite behavior might be a reason why direct evaluation of the rate of the reaction results not possible.

4.2.5 Evaluation of the kinetic constants involved during the *trans* to *cis* isomerization

If, when considering the reverse *cis* to *trans* isomerization, the high amount of variables involved allowed only partial determination, in the case of the forward reaction an additional degree of complexity rise. By evaluating through UV-Vis spectroscopy, it isn't in fact possible to keep the sample under irradiation while measuring, and being the time needed to acquire a spectrum, at the chosen concentration, roughly 3 minutes it is not possible to compute each time the amount of reversed reaction mostly from a precipitation point of view (see paragraph 4.2.3).

The data acquired showed in fact no linear behavior within irradiation.

From a comparison point of view, moreover, a data treating based on ^{1}H-NMR wasn't possible since only overlapped peaks were present in the smaller nanoparticles.

4.2.6 Conclusions and prospective

In summary it was possible to determine only some of the kinetic constants involved in the overall process due to the high variability of the system and of the multiple competitive processes involved.

Still, a variation of the precipitation kinetics of the nanoparticles depending on the sizes was obtained and, most importantly, a trend for the *cis* state stability depending on the pi-stacking was demonstrated. Both processes present, for early reaction times a linear behavior, following a first order (or pseudo first-order kinetic

law). For longer times a quasi-linear behavior is shown as well but with a different slope to indicate different stages in the process.

4.3.1 Surface Enhanced Raman Spectroscopy on AZO coated AuNPs-Generalities

Aim of the project was to determine through Surface Enhanced Raman Spectroscopy the coupling between AZO moieties when in the *trans* or the *cis* configuration and when absorbed on different sized nanoparticles.

Raman Spectroscopy is a powerful technique to characterize the samples because it depends on the vibrational modes of the molecules and in particular their ability to polarize. A Raman spectrum will depend not only on the characteristics of the molecule itself but also on its chemical and physical environment. Figure 4.3.1. presents a sketch of the SERS measurements.

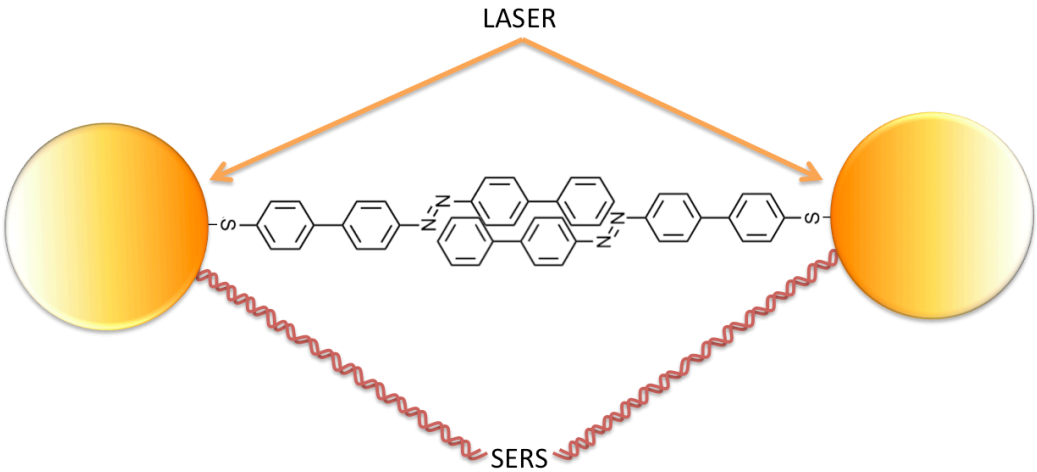

Figure 4.3.1 SERS cartoon. Two neighbors gold nanoparticles with absorbed azobenzene moieties are irradiated with a laser at a specific wavelength. Due to surface properties the intensity of the laser will be reflected and will increase while the azobenzenes will polarize and emit at a different frequency. (Insights on the Raman and Surface enhanced Raman techniques are presented in Chapters II and III)

First, it was necessary to investigate the behavior of the azobenzene molecules when not absorbed on nanoparticles.

Figure 4.3.2 shows a typical obtained spectrum of the molecule in the *trans* configuration and the molecular modes involved when using a 633nm laser and 10 seconds acquisition time.

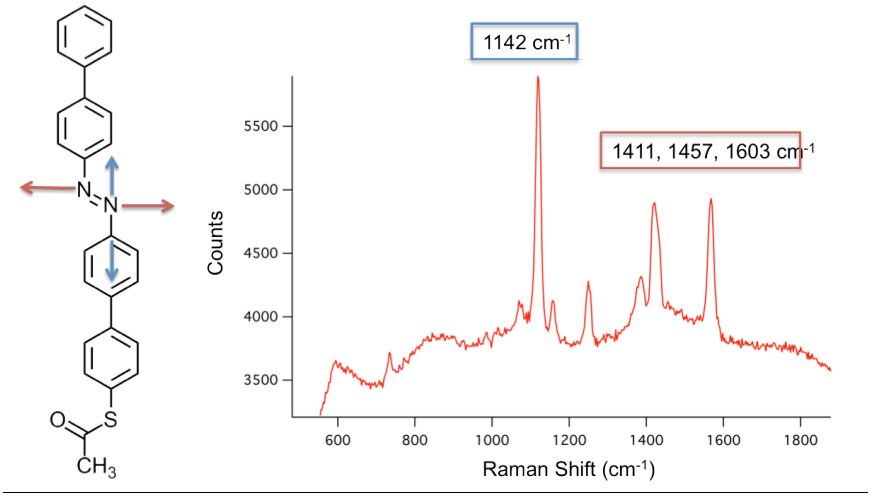

Figure 4.3.2 On the right the chemical formula of *trans* AZO and two polarization modes showed at the right in the Raman spectrum.

As shown in literature, there are two main documented changes in the SERS spectra when isomerizing an azobenzene absorbed on a gold nanoparticle surface, i.e. a lowering of the Raman absorption resulting in a lower definition of the signals involved,[22] and a shift of the Raman signal to give one broad absorption band[23]. The same feature shown for the *cis* moieties was seen in the case of highly aggregated nanoparticles, maybe due to the lower intrinsic polarizability in a high concentration matrix. As a result the unique identification of the *cis* isomer is difficult. Figure 4.3.3 shows the typical *cis* isomer spectrum.

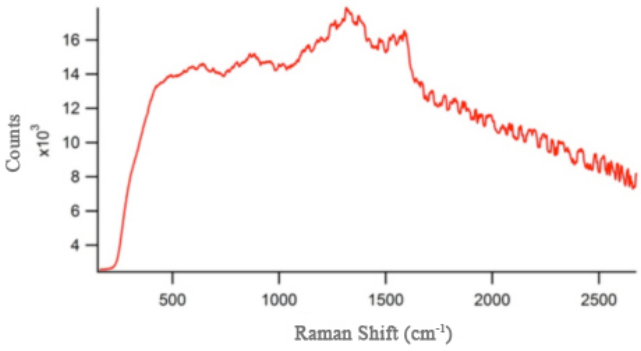

Fig.4.3.3 Typical Raman Spectrum of AZO molecule in solid, *cis* isomer.

Since the features of the *cis* spectrum were not well resolved, it was decided to acquire spectra in solution, unfortunately, no big differences were observed.

Two different procedures were employed: one using nanoparticles dispersed in toluene and a second one adding DMF to tune the aggregation. The substrate utilized was glass coverslips: sonicated in acetone for 15 minutes, 2 times in sodium hydroxide for 5 minutes, and 2 times in MilliQ water for 15 minutes, then Argon blowed and exposed to ozone for 15 minutes.

4.3.2 Experimental evidences obtained utilizing toluene solutions

To get a full picture of the system, a first set of over 15750 spectra was acquired in different conditions as summarized in Table 1. Freshly cleaned cover-glasses were employed as substrates. Six different nanoparticle samples were employed: two independently synthesized samples of 3nm azobenzene coated gold nanoparticles, two independently synthesized samples of 15nm gold nanoparticles. And two mixed (dodecanthiol and azobenzene) coated gold nanoparticles samples, one 3nm size and the second one 15 nm size. Each nanoparticle sample was deposited between 3 and 10 times to obtain statistical averaging over the deposition process and statistical representativity of the data obtained. The nanoparticles employed as well as the molecules were dispersed in toluene.

Table 1. Experimental Conditions tested

Material	**Deposition conditions**	**Additional measurements information**	**Mapping**
AZOAuNP1	Drop casting in dark	a) in dark	
		b) under UV irradiation	
	Drop casting of irradiated solution under UV	a) under UV irradiation	
		b) 24h after a)	
		c) under 2nd UV cycle	
AZOAuNP2	Drop casting in dark	a) In dark	×
		b) After 3 days	×
	Drop casting of irradiated solution under UV	c) Under Uv irradiation	×
		d) After time.	×

		e) Under UV irradiation	×
DTAZOAuNP2	Drop casting in dark	a) In dark	
		b) After 3 days	
	Drop casting of irradiated solution under UV	a) Under Uv irradiation	
		b) After time.	
DTAZOAuNP1	Drop casting in dark	a) In dark	
		b) After 3 days	
	Drop casting of irradiated solution under UV	c) Under Uv irradiation	

Furthermore it was found that both increasing the concentration of nanoparticles and irradiating gave rise to similar features in the acquired SERS spectra as well as an increased intensity of the Raman spectra acquired.

Figure 4.3.4 shows the typical spectra when either moving to a more concentrated part of the sample or keeping the same density but irradiating the sample.

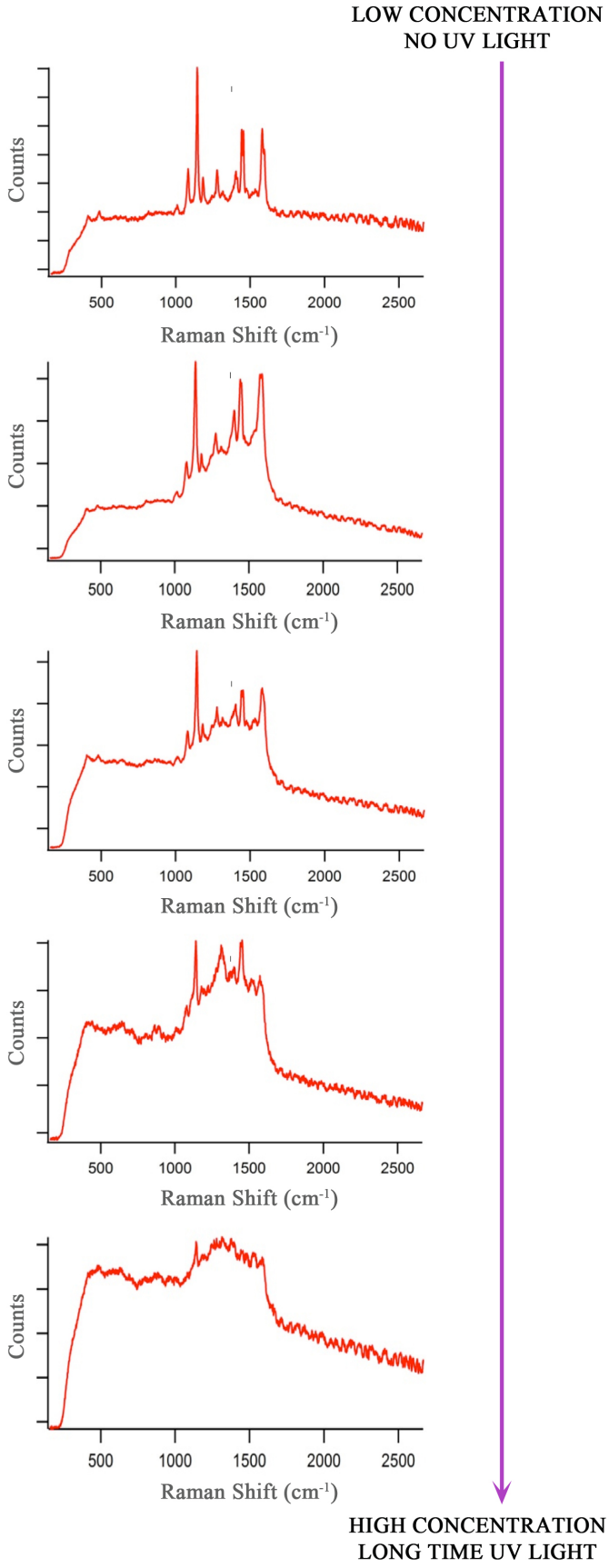

Figure 4.3.4 Dependence of the observed azobenzene spectra under prolonged irradiation or increased concentration.

As the features of the *trans* isomer are easily definable, it was decided to evaluate the amount of *trans* in each sample and study the variation of it with irradiation. Column charts in which the black part represents the amount of trans in the samples will be presented from now on.

Regarding the smaller nanoparticles (AZOAuNP1 a and b), Figure 4.3.5 shows a comparison between samples deposited in *trans* or *cis* but measured after at least two days to allow complete relaxation to the *trans* form. The result is expressed as *trans* ratio and it is equal to 78.43% ±0.71. The low standard deviation between measurements suggests how in a sample of small nanoparticles the variation due to deposition is not a possible factor determining the error.

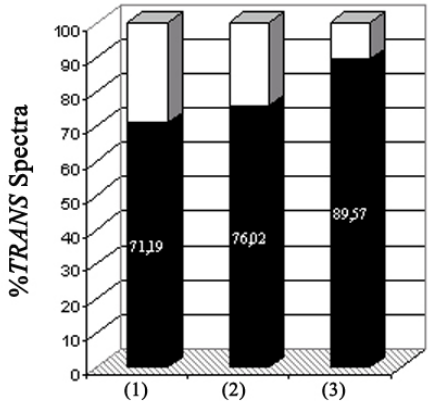

Figure 4.3.5 Comparison between the different deposited samples.

Another factor to be considered was the switching ability of the NPs when deposited in dark or under UV irradiation, considering the tendency of the samples to aggregate. A comparison between AZOAuNP1 samples when deposited in *trans* (in dark) or in the *cis* (deposited after irradiation in solution and drop casting under UV light) but measured just after deposition, is presented in Figure 4.3.6.

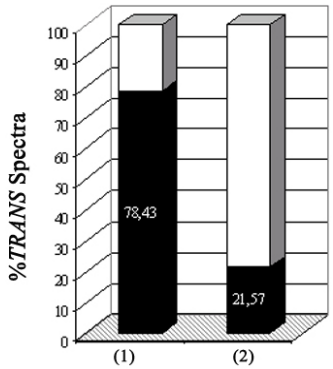

Figure 4.3.6 Comparison of the percentage of *trans* spectra when AZOAuNP1 are deposited in dark or under UV irradiation.

The ability of perform cycles of the AZOAuNP1 deposited in dark was found to be very poor and even the first irradiation didn't give appreciable results.

Better results were obtained when the nanoparticles were firstly deposited in *cis* form (Figure 4.3.7).

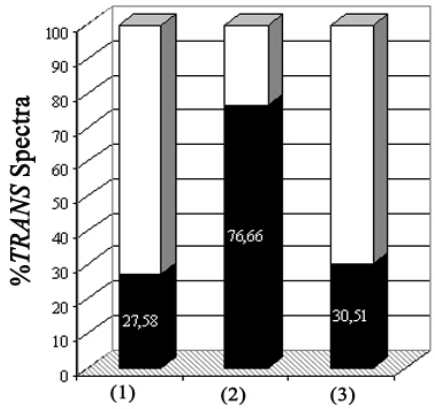

Figure 4.3.7 Percentage of *trans* azobenzene detected from left to right: just after deposition under UV (sample irradiated for more than 24h), after 24h time in order to allow relaxation to the *trans* form and after 1h of UV irradiation in situ.

As presented, the samples prepared in this way were able to isomerize giving an appreciable difference between the percentage of *trans* moieties before and after irradiation. Unfortunately no more than three cycles were possible since the samples were then not switching anymore.

Moving to the bigger nanoparticles better results were obtained from the point of view of switching percentage. Fully *trans* spectra were recorded when depositing the sample in dark and no *trans* when depositing in *cis*. Unfortunately no cycles were possible, likely due to fast ageing of the sample.

In general, the intensity of the Raman spectra obtained when the azobenzene is absorbed on 3nm particles is at least three times smaller than when absorbed on 15 nm particles as shown in Figure 4.3.8. Thus further experiments focused on the bigger particles.

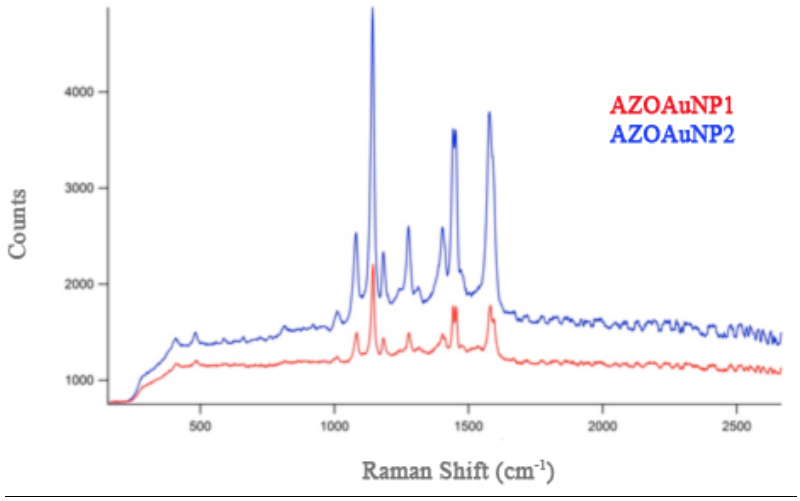

Figure 4.3.8 Typical Raman spectra of AZO *trans* isomer when absorbed on 3nm (red spectrum) or on 15nm (black spectrum) nanoparticles.

The bigger nanoparticles show higher Raman intensity, but, unfortunately, bigger nanoparticles also deeply affects cyclability *in-situ*, lowering the reliability of repeated acquisitions.

4.3.3 Experimental evidences obtained utilizing toluene : DMF solutions

It was decided to further investigate the smaller nanoparticles by adding a mixture of solvents, i.e. toluene: DMF (90:10). 4352 spectra were acquired and averaged in order to get good statistics.

The best results from the point of view of switching and cyclability were obtained when drop casting in the dark 200µl of a solution kept at 100°C for 1-2 minutes while stirring.

The illumination/measurements sequence was composed by the following:

1. First spectrum in dark
2. 2 h UV illumination
3. Second Spectrum
4. 24 h in dark at room temperature
5. Third Spectrum
6. 3 h UV illumination
7. Fourth spectrum

One of two results were obtained: either a *trans*-like spectrum, or else no features at all were registered. Figure 4.3.9 reports the typical *trans*-like spectra acquired for the samples spin cast from 10% DMSO in toluene for each cycle tested.

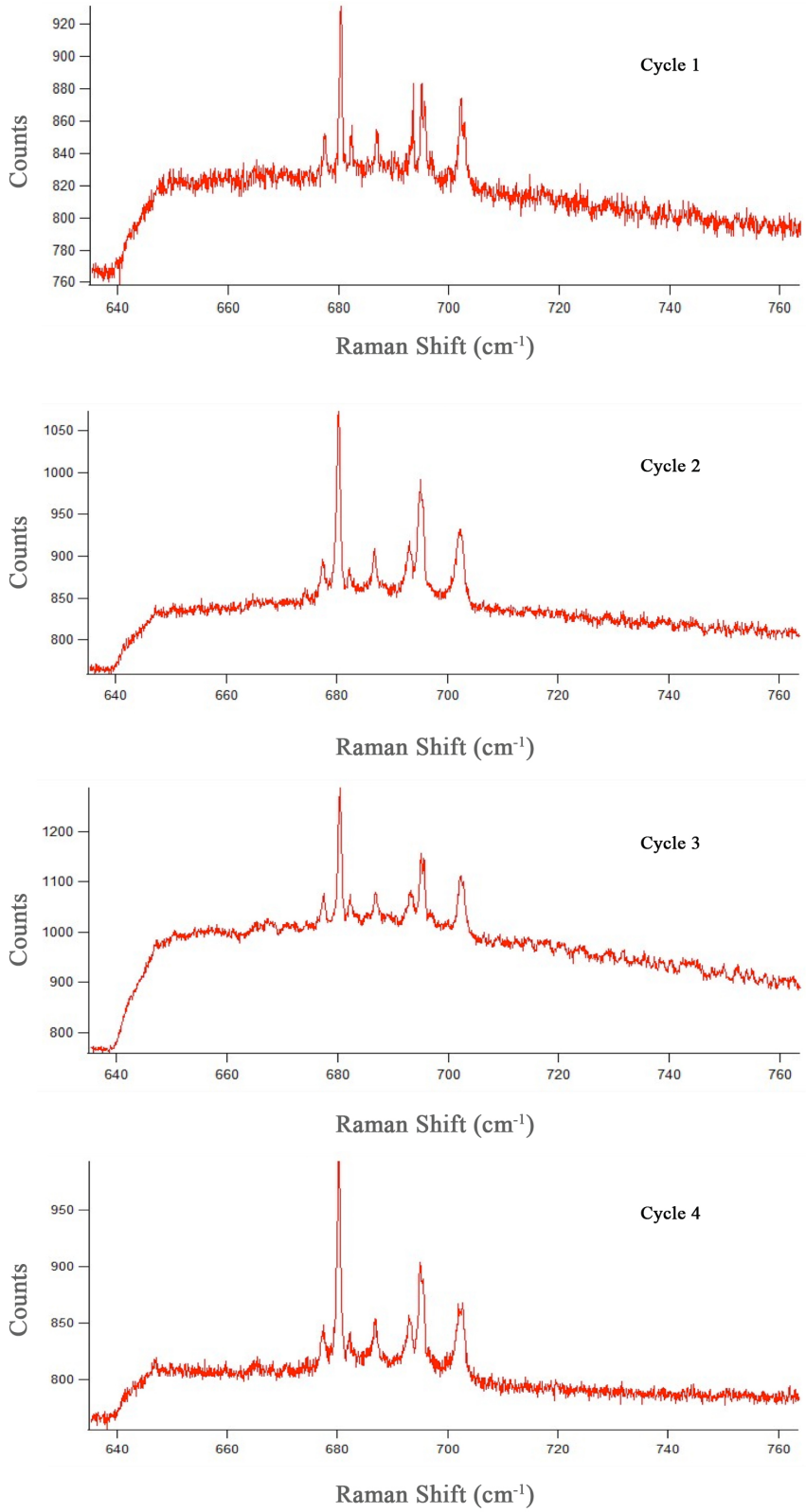

Figure 4.3.9 Typical Raman *trans* spectra observed at each irradiation cycle.

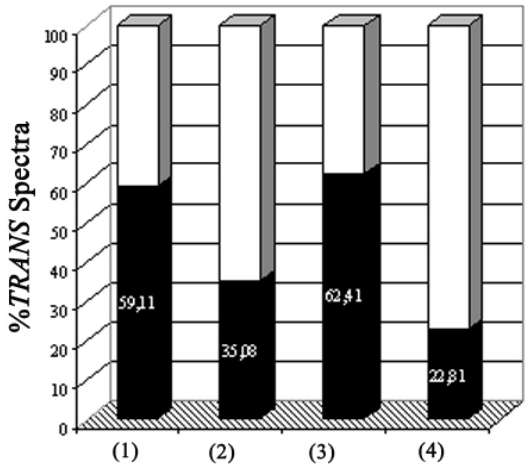

Figure 4.3.10 Comparison between the amount of *trans* AZO within irradiation: 60% in the first cycle, 35% in the second one, 62% in the third one, 23% in the fourth one (solvent?).

By adding DMF the investigated system maintains clearly a *cis-trans* cycle and shows higher reversibility than in absence of DMF (Figure 4.3.10).

The increased intensity of the Raman spectra after UV irradiation was also found on these samples even if over the cycles a gradual decrease can be noticed as well. A possible explanation is that damage to the samples due both to the UV light used for switching and the high intensity laser used for SERS accumulates with time, thus appearing to give less *trans* signals and lower intensity.

Until now, only the sample with 10% DMF was measured. This is a high amount, and therefore the particles will lie further from each other. This can explain the low intensity and the need for high acquisition times.

Due to systemic fluctuations, over 20000 spectra were acquired, allowing determination of the basic features of the spectra. More analysis with a smaller amount of DMSO on both the bigger and smaller nanoparticles needs to be done.

More measurements to obtain a full description of the system and higher number of cycles is currently ongoing.

Nevertheless it is clear that we have observed reversible isomerization of the azobenzene moieties on the nanoparticles via SERS spectroscopy over several irradiation cycles.

These promising initial studies suggest that with further fine tuning it should be possible to observe the same reversible isomerisation process in a dilute sample with SERS spectra from a few or ideally even a single molecule.

Appendix

All the reagents, solvents included, except water, were purchased from Aldrich. The MilliQ water was provided in our laboratory using a MQ water filter (Millipore-Direct Q 3).

The UV-Vis spectra were recorded with a Spectrophotometer UV-Vis-NIR (Shimadzu UV-3600) and for contemporary measurements of more sample and temperature control a JASCO V-670 equipped with a PAC-743R sample holder (6 cells and temperature control). ^{1}H-NMR spectra were recorded on Bruker Advance 400 (400.14 MHz). The irradiation lamp was a UV lamp with λ_{max} of emission centered around 366 nm (Benda NU-8 KL). All the images were acquired with a FIB (model FEI Dual Beam Strata 235) equipped with a STEM detector (TEM module, FEI).

The STEM images were acquired with a FIB (model FEI Dual Beam Strata 235) equipped with a STEM detector (TEM module, FEI). The TEM images were acquired by employing a Philips CM100 transmission electron microscope at 80kV equipped with a 2000 by 2000 pixel charge-coupled Veleta camera from Olympus._The particles were deposited by drop-casting the colloideal dispersion in solvent on a carbon coated gold-plated copper grid and air-dried.

Raman spectroscopy and Raman mapping were performed employing an invert optical microscope (Olympus, IX71, or Nikon TiU) equipped with a 100x oil immersion objective (Olympus 100x NA=1.3 UPlanFLN, or Nikon Plan Fluor 100x N.A. = 1.3). Two spectrometer were employed: an Andor, Shamrock 303 or Horiba, iHR320 both coupled with an Electron magnifying CCD camera (Andor, Newton DU970P-BV or DU920P-BR-DD). The excitation source was a He-Ne laser (JDS Uniphase, 1145P, 28 mW or Research Electro-Optics, Inc., 32413, 35.0mW, 632.8 nm wavelength). An interference filter (Chroma technology corporation, Z633/x10) was employed in order to selectively chose the 632.8 nm radiation. The samples excitation was performed by mean of a circular polarized light, compensating the polarization shifts induced by the dichroic mirrors through λ/4 and λ/2 wave-plates. After passing through the dichroic mirror (Z633RDC, Chroma Technology Co.) equipped with an additional spectral filter (HQ645LP, Chroma Technology Co.) the Raman scattering was collected utilizing the CCD camera.

References

1 Hodak, J. H., Henglein, A. & Hartland, G. V. Photophysics of nanometer sized metal particles: Electron-phonon coupling and coherent excitation of breathing vibrational modes. *Journal of Physical Chemistry B* **104**, 9954-9965 (2000).

2 Jain, P. K., Lee, K. S., El-Sayed, I. H. & El-Sayed, M. A. Calculated absorption and scattering properties of gold nanoparticles of different size, shape, and composition: Applications in biological imaging and biomedicine. *Journal of Physical Chemistry B* **110**, 7238-7248 (2006).

3 Kawai, T., Nakamura, S., Sumi, A. & Kondo, T. Control of dispersion-coagulation behavior of Au nanoparticles capped with azobenzene-derivatized alkanethiol in a mixed chloroforrn-ethanol solvent. *Thin Solid Films* **516** (2008).

4 Manna, A. *et al.* Optimized photoisomerization on gold nanoparticles capped by unsymmetrical azobenzene disulfides. *Chemistry of Materials* **15**, 20-28 (2003).

5 Myroshnychenko, V. *et al.* Modelling the optical response of gold nanoparticles. *Chemical Society Reviews* **37** (2008).

6 Rechberger, W. *et al.* Optical properties of two interacting gold nanoparticles. *Optics Communications* **220**, 137-141 (2003).

7 Sendroiu, I. E., Mertens, S. F. L. & Schiffrin, D. J. Plasmon interactions between gold nanoparticles in aqueous solution with controlled spatial separation. *Physical Chemistry Chemical Physics* **8**, 1430-1436 (2006).

8 Sidhaye, D. S., Kashyap, S., Sastry, M., Hotha, S. & Prasad, B. L. V. Gold nanoparticle networks with photoresponsive interparticle spacings. *Langmuir* **21**, 7979-7984 (2005).

9 Zabet-Khosousi, A. & Dhirani, A. A. Charge transport in nanoparticle assemblies. *Chemical Reviews* **108**, 4072-4124 (2008).

10 Zhou, J. F., Sedev, R., Beattie, D. & Ralston, J. Light-induced aggregation of colloidal gold nanoparticles capped by thymine derivatives. *Langmuir* **24**, 4506-4511 (2008).

11 Mustafa, D. E. *et al.* Surface Plasmon Coupling Effect of Gold Nanoparticles with Different Shape and Size on Conventional Surface Plasmon Resonance Signal. *Plasmonics* **5**, 221-231 (2010).

12 Zhang, J., Whitesell, J. K. & Fox, M. A. Photoreactivity of self-assembled monolayers of azobenzene or stilbene derivatives capped on colloidal gold clusters. *Chemistry of Materials* **13**, 2323-2331 (2001).

13 Klajn, R., Wesson, P. J., Bishop, K. J. M. & Grzybowski, B. A. Writing Self-Erasing Images using Metastable Nanoparticle "Inks". *Angewandte Chemie-International Edition* **48**, 7035-7039 (2009).

14 Raimondo, C., Reinders, F., Soydaner, U., Mayor, M. & Samorì, P. Light-responsive reversible solvation and precipitation of gold nanoparticles. *Chem. Commun.* **46**, 1147-1149 (2010).

15 Elbing, M. *et al.* Single Component Self-Assembled Monolayers of Aromatic Azo-Biphenyl: Influence of the Packing Tightness on the SAM Structure and Light-Induced Molecular Movements. *Adv. Funct. Mater.* **18**, 2972-2983 (2008).

16 Browne, K. P. & Grzybowski, B. A. Controlling the Properties of Self-Assembled Monolayers by Substrate Curvature. *Langmuir* **27**, 1246-1250, (2011).

17 Kumara, M. T., Tripp, B. C. & Muralidharan, S. Self-assembly of metal nanoparticles and nanotubes on bioengineered flagella scaffolds. *Chemistry of Materials* **19**, 2056-2064 (2007).

18 Petkov, V. *et al.* Structure of gold nanoparticles suspended in water studied by x-ray diffraction and computer simulations. *Physical Review B* **72** (2005).

19 Balmes, O., Malm, J. O., Pettersson, N., Karlsson, G. & Bovin, J. O. Imaging atomic structure in metal nanoparticles using high-resolution cryo-TEM. *Microscopy and Microanalysis* **12**, 145-150 (2006).

20 Connors, K. A. Chemical Kinetics. *John Whiley & Sons, Inc.* (1990).

21 Aslan, K., Luhrs, C. C. & Perez-Luna, V. H. Controlled and reversible aggregation of biotinylated gold nanoparticles with streptavidin. *Journal of Physical Chemistry B* **108**, 15631-15639 (2004).

22 Zheng, Y. B. *et al.* Surface-Enhanced Raman Spectroscopy to Probe Reversibly Photoswitchable Azobenzene in Controlled Nanoscale Environments. *Nano Letters* **11**, 3447-3452 (2011).

23 Jung, U. *et al.* Gap-mode SERS studies of azobenzene-containing self-assembled monolayers on Au(111). *Journal of Colloid and Interface Science* **341**, 366-375 (2010).

Chapter 5. 100 and 50 nm- gap electrodes

By designing, an electrical junction can feature either a vertical or horizontal geometry. The former can rely on different type of electrode pairs such as those based on Hg drop,[1] SPM techniques,[2] etc. Unfortunately, while being easier to be implemented on the laboratory scale to get reproducible measurements, vertical nanoscopic junctions are not very relevant for technological applications. On the other hand, horizontal nanoscale junctionsrequire technologically demanding top-down tools to perform the fabrication, but they are of potential technological relevance as they can be integrated into complex circuitry. Moreover, tailoring interfaces and controlling the integration of conducting molecular based architechtures between metallic nanoelectrodes is a challenge. The use of metallic nanoparticles has been shown to be a smart solution to facilitate the junction formation.[3] It therefore appears appealing the formation of horizontal junctions integrating AZO coated metallic nanoparticles to generate light responsive devices.

This Chapter focuses on the functionalization of 100 and 50 nm gap electrodes and their use to test the electrical conductivity of AZO molecules. Previous studies on conductivity and switchability of AZO molecules were performed on devices in vertical configuration (measured via C-AFM and Hg-drop electrodes) demonstrating a reversible change of conduction under illumination.[4,5]

5.1.1 100nm gap electrodes, aim and materials

Light switchable molecular devices based on responsive microspheres as a new way to better understand the electrical conductivity of AZO molecules. The aim of the project was the characterization of AZO-SAMs in horizontal configurations.

To validate the results, three types of SAMs have been prepared and investigated via microsphere-based junctions; i.e. AZO-SAMs coating both the nanotrenches and the microspheres, AZO coated microspheres and alkylthiol coated nanotrenches (and vice versa) and alkylthiol SAM coating both the nanotrenches and the microspheres.

The last experiment was performed as blank to detect any possible artifacts in the circuit (e.g. defects in the SiO_2 substrate, traces of metallic doping, etc., which can result in photoconductance artifacts).

The preparation and characteristics of the microspheres employed are presented in Chapter III.

The AZO SAMs were prepared by immersion of the freshly cleaned substrates in a 10^{-5}M solution of AZO in degassed and alumina filtered chloroform for 24-48 hours to allow higher molecule packing.[6] They were then rinsed and nitrogen flow dried.

For the alkylthiol SAM it was decided to use a dodecanthiol because it is of the characteristic high resistance and because well known in the literature as non-switching via illumination at the wavelengths considered. A total amount of 126 nanotrenches were prepared on both cover glass (0.13-0.17 nm thick) and Si/SiO_2 wafers (550nm thermal SiO_2 to prevent electrical shorts). Two different setups were tested to evaluate the effect of environmental conditions and way of illumination. Figure 5.1.1 shows sketches of the circuits used for measurements. The first setup consisted of measurements performed in a glovebox (water and oxygen levels below 10ppm) illuminated from above (365nm, 87μW/cm^2), measured by means of an electrometer, Keithley 2536, interfaced by in-house developed software. The second setup consisted of an inverted optical microscope with LED light source focused on the sample through the microscope objective (N.A. = 0.65) when using transparent substrates and from the top through the illuminating condenser (N.A. = 0.55) when using Si/SiO_2 wafers.

A detailed description of nanotrenches and microspheres fabrication is

presented in the Methods Chapter (III). The nanotrenches fabricated exhibited a leakage current under illumination below 10pA with 1V bias applied. After SAMs preparation, 90 nanotrenches showed comparable behavior and after microspheres deposition only 25 (20% of the total) resulted in working devices, these samples were tested further. Of the excluded devices 10% showed short circuits (over 10 μA current under 1 V bias) probably due to high microspheres coverage and metal-metal interconnections as estimated by SEM micrographs. It was then decided to scale down the microspheres concentration even if this resulted in a large fraction of nanotrenches that remained electrically opened.

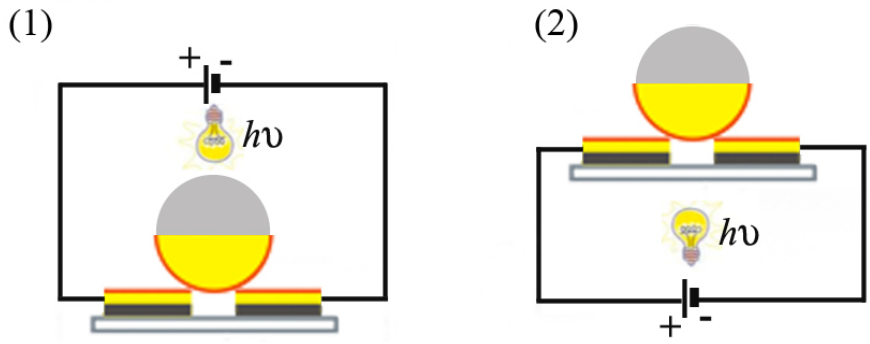

Figure 5.1.1 Sketches of circuits used for measurements. The Au hemisphere of the particle as well as the electrodes (in yellow), are coated with a chemisorbed self-assembled monolayer (in red) of either C12 or AZO (1) with above illumination in glove-box (2) with bottom illumination in air.

Figure 5.1.2 shows the typical IV characteristics of the nanotrench electrodes before and after microsphere trapping. After closing the circuit the current showed Ohmic behavior assuring a close circuit measurement.

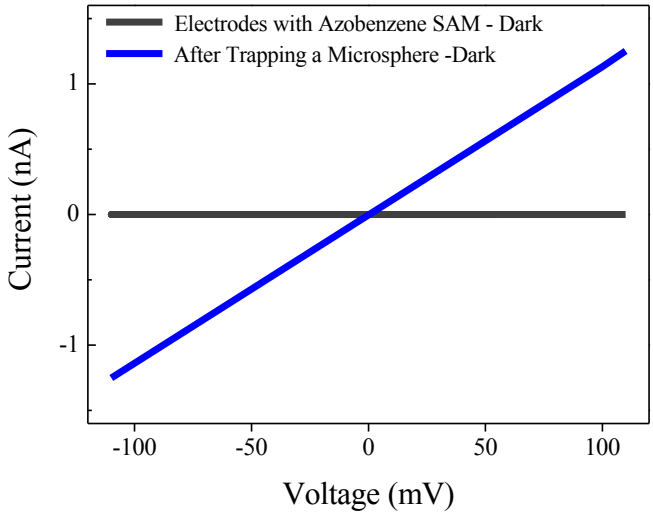

Figure 5.1.2 IV curves of nanotrench electrodes before (black line) and after (blue line) microsphere trapping.

Rigorous criterions for the choice of sample were applied, i.e. only samples exhibiting at least two orders of magnitude more than the initial current (after microspheres deposition) were considered. Table 5.1.1 present a summary of the fabricated devices.

Table 5.1.1 Summary of all the fabricated devices, type of measurements performed and previous results.

Type of junction	Fabricated			Measured		Shorts	Connected
	Total	Cover-glass	Si/SiO_2	*hv* from above	*hv* from below		
AZO-AZO	98	49	49	49	49	2	18
AZO-Alk	21	14	7	7	14	2	5
Alk-Alk	49	28	21	21	28	3	18
TOT.	168	91	77	77	91	7	41

5.1.2 Shining light from above the sample

95% of the devices analyzed by irradiating from above were measured using the first setup. Most of the devices didn't show any switching behavior. The others showed non-reproducible and unconventional behaviors even when the open nanogap had been previously tested applying a 10V bias and a switching had been seen. Figure 5.2.3 shows some examples of the tested devices.

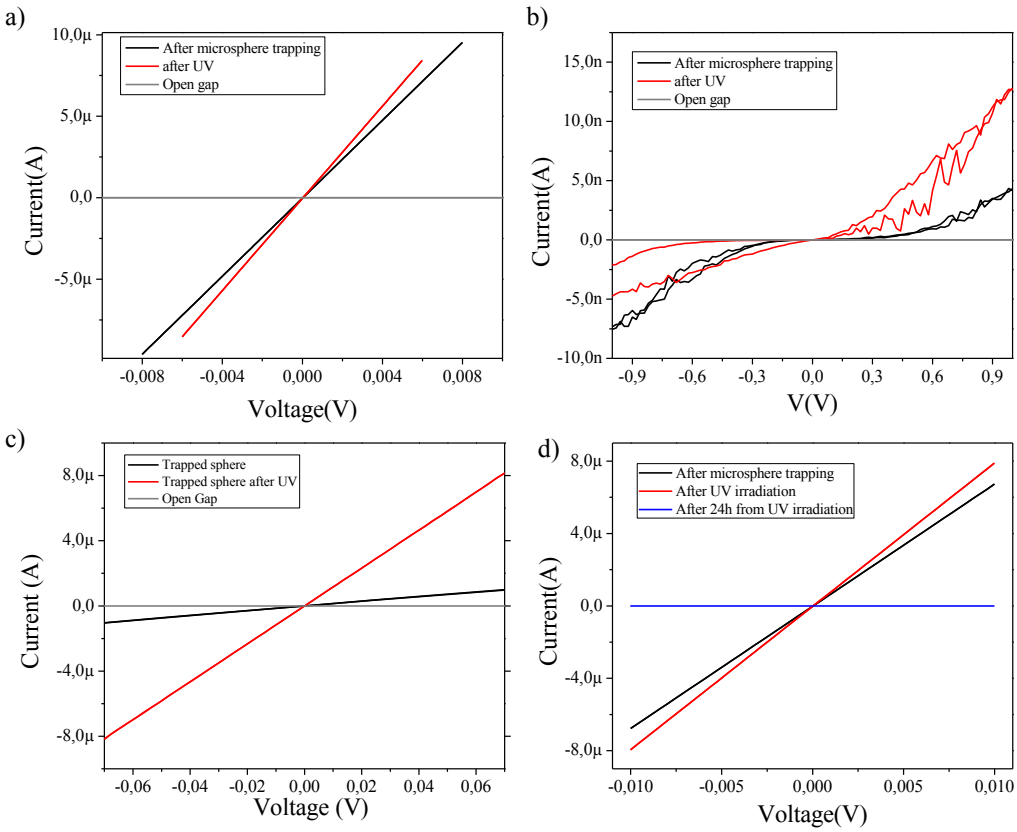

Figure 5.1.3 IV characteristics measured with the first setup and with the sample irradiated from above. a), b) and c) show three representative IVs before trapping, after trapping and after UV illumination respectively for the samples that showed switching within UV irradiation while d) shows a typical behavior after 24 hours in dark from the UV illumination.

As presented in figure 5.1.3 the currents measured were high if compared to normally measured nanogap electrodes, probably indicating a too high concentration of nanospheres and Au-Au interconnection. Only one sample gave the typical currents even if no linear behavior over bias was observed. Most of the samples, even when switching showed no current if measured after 24h time.

Most of the samples didn't show any switching behavior. A probable explanation for this is the lower light-exposition due to microsphere shadow.

To prove that the mainly non-switching behavior was related to the irradiation position, a sample was tested with the second setup. No switch was observed in this case either. A summary of the results obtained using the setup described above is reported in Table 5.1.2.

Table 5.1.2 Summary of all measurements performed and of results obtained by measuring in a glovebox and shining light from above the sample.

Type of junction	Connected	Switching	Non-Switching
AZO-AZO	11	3	8
AZO-Alk	4	2	2
Alk-Alk	9	2	7

Due to the unimpressive results obtained through this technique, it was decided to focus on the second setup, irradiating the samples from below.

5.1.3 Shining light from below the sample

Table 5.1.3 reports the results obtained for the nanotrench junctions prepared on cover glass when irradiating the samples from below.

Table 5.1.3 Summary of all measurements performed and of results obtained measuring in air and shining light from below the sample.

Type of junction	Connected	Switching	Non-Switching
AZO-AZO	7	7	0
AZO-Alk	1	1	0
Alk-Alk	9	1	8

A total of 17 samples showed the right characteristics (see subchapter 5.1) to be considered in the study. The switching criterion was chosen to be a reversible change that exceeded 10% of the previous value upon illumination. The quantified resistance's ratios were between 1.1 and 3.0, value notably lower than the ones previously reported in the literature.[4,5] This difference is probably due to the different geometry of the electrodes, being not vertical but horizontal. However, it should be noted that considering the intrinsic characteristic of the devices we would expect an opposite trend: the previously presented junctions were Metal-Molecule-Metal, whereas in this case are Metal-Molecule-Molecule-Metal. The absence of chemical bonds between the two organic molecules usually implies a significantly lower conductance. A typical IV behavior within irradiation is shown in Figure 5.1.4. The black line represents the electrical response of an open trench, the blue line of a trench

having a microsphere trapped. When irradiating at 365nm a higher current is observed. A linear behavior was observed in the ±1V range while increasing the Voltage range non-linear behavior could be observed. This non-linear behavior was not reproducible from trench to trench and it was probably dependent on the intrinsic electrical instability of the nanotrench itself.

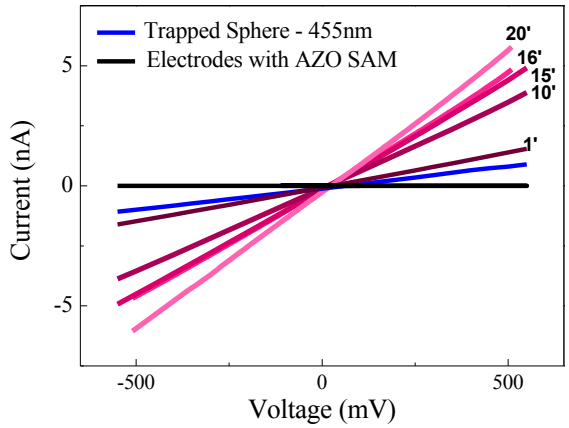

Figure 5.1.4 IV curves behavious with UV irradiation. Black: before microsphere trapping, Blue: after microsphere trapping, Magenta: behavior when irradiated.

The overall process reversibility was tested in all the switching devices typically giving the behavior shown in Figure 5.1.5 where the samples coated with AZO in the *trans* configuration (curve 1) were first exposed to 365nm light to allow the *trans* to *cis* isomerization (curve 2), then to 455nm light to allow the back *cis* to *trans* reaction (curve 3) and again to 365nm light providing unambiguous evidence for the full reversibility of the process (curve 4).

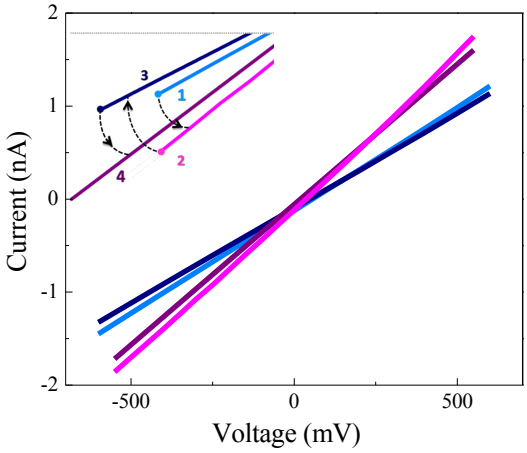

Figure 5.1.5 IV curves of switching samples when exposed to cycles of UV and Vis light, (1) before exposition to any light (postulates *trans* form), (2) after exposition to UV light (*cis* form), (3) after Vis light (*trans* form) and finally (4) after exposition to UV light again (*cis* form).

It is worth mentioning that only 16 out of the 17 junctions prepared showed consistent switching behavior. The Alk junction showed a really poor conduction (R ≈ 3GΩ) and no reversibility. A possible explanation for this behavior could be instability due to UV light mediating modification of the junction. Another important check was performed to assure that freshly prepared samples (postulated *trans*) were in fact not showing any switching behavior at 455 nm. This additional check proved that the starting samples were in fact in the *trans* configuration and the current modifications measured could be attributed to isomerization of the film. Moreover, several tens of switching events were recordable without any optimization. A representative graph is shown in Figure 5.1.6 where the measured resistance is plotted versus the number of following irradiation events.

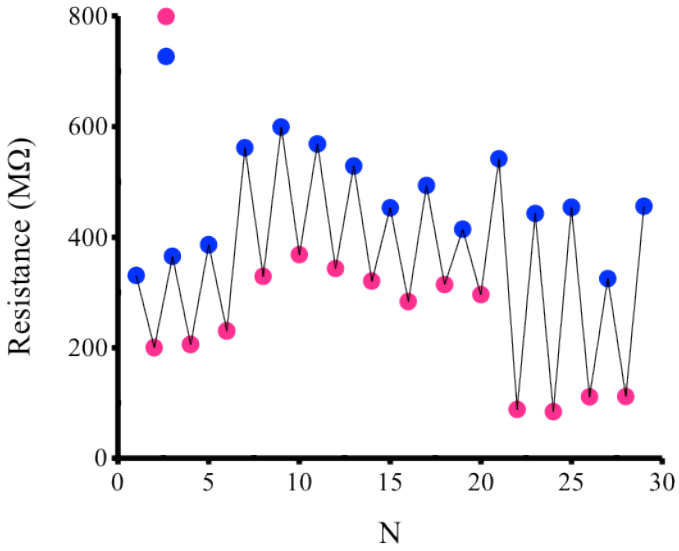

Figure 5.1.6 Measured resistance vs number of opposite irradiation events on a single, representative, junction.

The evaluated switching time was around 10 minutes and the same for both the reactions when alternatively irradiating with 365 and 455nm wavelengths.

Particularly important is that up to 30 cycles were achievable in this particular geometry demonstrating a high long-term stability of the junctions and almost no fatigue contrary to what is generally reported on these kind of switches and device geometry.

Only on one extensively studied sample, after over 30 switches, was it possible to observe fatigue effect. The current variation was measured over time, treating the sample with cycles of UV light (to allow the *trans* to *cis* reaction) and

dark to allow the back *cis* to *trans* reaction. Figure 5.1.7 shows the obtained behavior. It was possible to notice how, on an already stressed sample, kept under UV light, after reaching a maximum of variation, the current tended to decrease, to values more similar to the *trans* configuration. Nevertheless, if allowed to completely back isomerize to the *trans* configuration, it was possible to induce again the *trans* to *cis* reaction. A *cis* to *trans* transition under UV via STM studies is already documented in the literature[7] driving us to improve the stability studies to understand how long-term stabilization and irreversibility under UV can be optimized.

As this behavior was observed only in one sample more tests need to be done to evaluate the statistics.

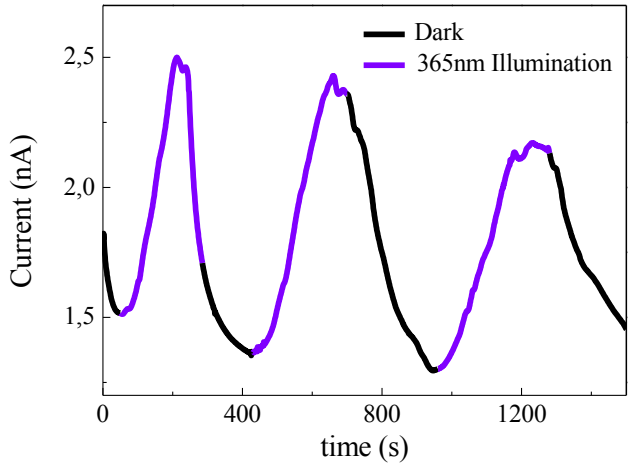

Figure 5.1.7 Current modulation within cycles of UV light and dark on an overstressed sample. The violet line represents the behavior under UV while the black like represents the one under dark conditions. The decreasing behaviour over irradiation has been attributed to overstress of the studied device.

5.1.4 Discussions

When measuring the IV characteristics of an AZO-SAM via nanotrench junctions gold coated interconnected by half gold coated microspheres, it is possible to properly evaluate the switch only when the system gets irradiated from the proper position. Irradiating from above the junction doesn't allow reliable results over the azobenzene switching, most probably due to the nanospheres shadow over the junction. UV illumination has been proven to modify the overall circuit but statistical data allows to define this event as highly improbable and any current modification is anyway not reversible. When irradiating from below the sample, instead, the AZO

molecule has been confirmed to switch reversibly for tens of cycles giving reproducible results and no fatigue is shown except for one overstressed sample. The current variation over isomerization is much lower than the one obtained on different geometries due to a different connection between molecules. The observed electrical transport originates from charge transfer, most probably non-resonant tunneling, through the molecules.

Therefore, AZO molecules can be inserted into not only vertical but horizontal electrode geometry where they show switching behavior. The devices work with high reproducibility and stability over a period of days in ambient conditions. This particular characteristic allows realization and investigation of multifunctional molecular materials.[8]

5.2 50nm gap electrodes

50nm gap electrodes, fabricated as presented in Chapter III (Methods), were employed to get insights on the tunneling resistance in a horizontal geometry and involving a smaller number of molecules in the process. The preparation and analysis method were designed to overcome one of the biggest issues of Molecular Electronics, i.e. statistical representativity of the acquired data. Normally a high number of devices need to be tested to get reliable experimental evidence,[9] one of the aims of this project was to reduce the amount of devices needed, but still allowing high statistical evidence by C-AFM technique. The specifics of the AFM, C-AFM techniques and of the nanotrenches fabrication and characteristics and theory behind can be found in Chapters II and III. The SEM images of the interconnected electrodes featured in the samples are presented in Figure 5.2.1 together with sketches of the circuits. As reported in Chapter III, the sample preparation consisted of 6 steps:

1. Cleaning the protecting polymer resist layer on top of the junctions.
2. AZO-SAM functionalization of the electrodes (described in Chapter III).
3. Hitching of the electrode over a magnet by means of tape in order to insulate the bottom third electrode and connect the device to a magnetic substrate to allow stabilization over C-AFM measurements.
4. Connection via silver-paste of every other electrode obtaining a device composed of every other electrode connected, while the middle electrodes are left un-connected. (see Figure 5.2.1, 4 for the picture of the result).

5. Deposition of 80 nm gold nanoparticles (characteristics of the nanoparticles can be found in Chapter II) on the nanogaps via drop casting.
6. Electrical measurements.

All the samples were checked via AFM and Keithley before and after SAM functionalization to choose the test-electrodes.

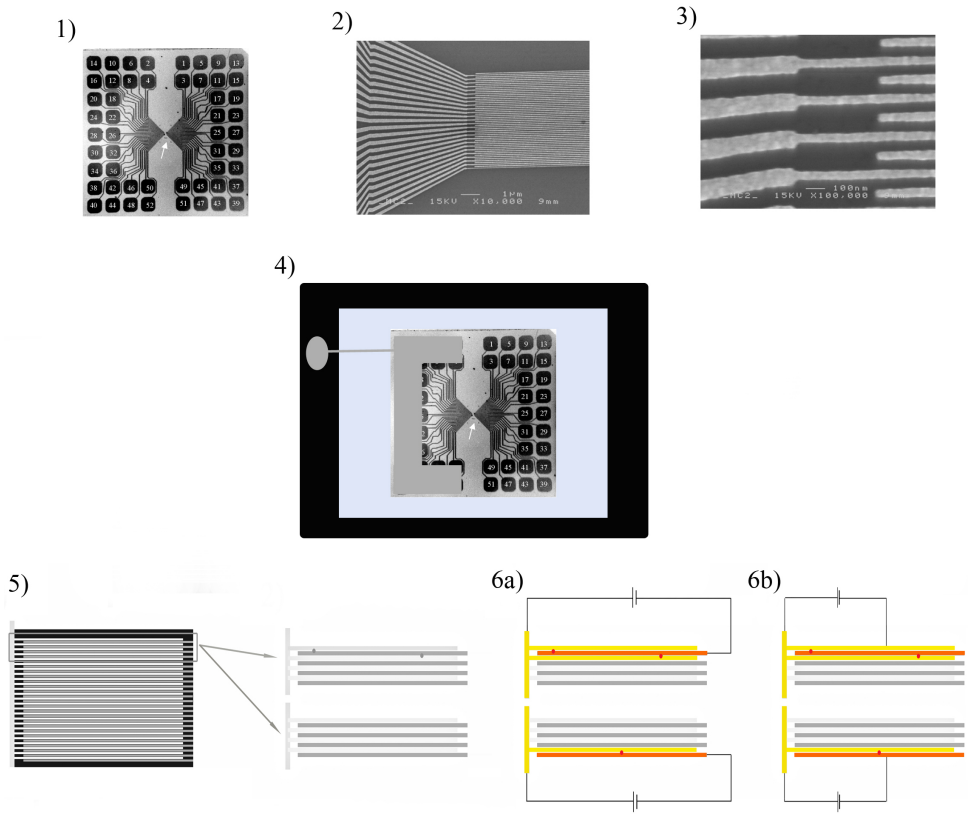

Figure 5.2.1 50nm gap electrodes. 1), 2) and 3) the SEM images of the nanogap. The full electrode and two magnifications of the nanogap electrodes respectively. 4) The preparation of the electrode gluing it over a magnet to insulate the gate electrode and allow stabilization for C-AFM measurements. The left side of the electrode is connected with silver paste and then on the magnet to allow bias application through that electrode. The electrodes in the devices are interdigitated and connected through nanoparticles. 5) Scheme of the interdigitated electrodes. 6) Schematic representation of the circuit when measuring through a keithley, *i.e.* over all the gap, a) and through a C-AFM, *i.e.* over the length of the gap, b).

After getting information about the basic reliability of the system, one of the critical steps is the nanoparticles deposition, *i.e.* drop casting the correct concentration of nanoparticles needed to create a circuit without forming short circuits (Figure 5.2.4).

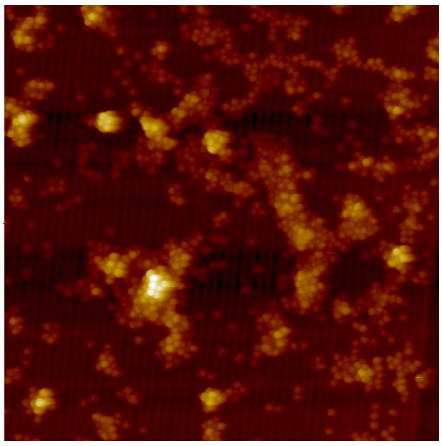

Figure 5.2.4 AFM, tapping mode image of a test electrode covered with a high concentration of nanoparticles. 5 μm × 5 μm images, z scale = 100 nm.

The electrical characterization over the devices covered with a high concentration of nanoparticles gave a metal-like behavior with low resistances, suggesting metal interconnection between the different electrodes. Accordingly, the chosen approach was based on the use of a very low concentration of nanoparticles that still allowed charge transfer characterization on a smaller number of molecules by using conducting AFM (for the specifications see Chapter III). The overall gap was separately measured employing macroelectrodes.

As statistical representativity was one of the main goals of the project, it was decided to perform the electrical characterization only on the electrodes integrating exactly 80 nm particles (the nanoparticles always present a certain size distribution), in order to extrapolate the evidences from the same junctions. To be able to identify which electrodes could be taken into consideration and how many 80 nm nanoparticles were connecting the electrodes, AFM images of all the electrodes' lengths were acquired, as presented in Figure 5.2.5, and an analysis based on the height threshold was performed. Figure 5.2.5 presents the application of different thresolds to the same image. The electrodes featuring nanoparticles smaller or bigger than 80nm (±5nm) were not studied further.

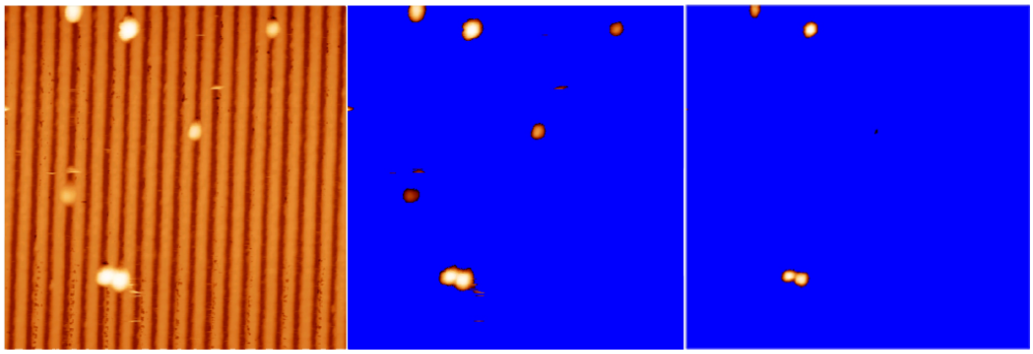

Figure 5.2.5 LEFT: 2µm AFM image of nanotrenches after 80 nm particles drop casting (z scale 100nm). MIDDLE: 40nm threshold application (to identify all the objects roughly able to connect the electrodes). RIGHT: 75nm threshold application (to identify only the 80 nm particles)

5.2.1 Full circuit measurements via electrometer

In order to be sure of the reliability of the nanotrenches when drop-casting nanoparticles, characterizations over the overall gaps were performed. To perform the data analysis, a simple sketch of the circuit needs to be drawn. Due to the design of the nanotrenches the overall circuit is composed of three electrodes electrically connected by a certain number of resistances in parallel, i.e. the nanoparticles.

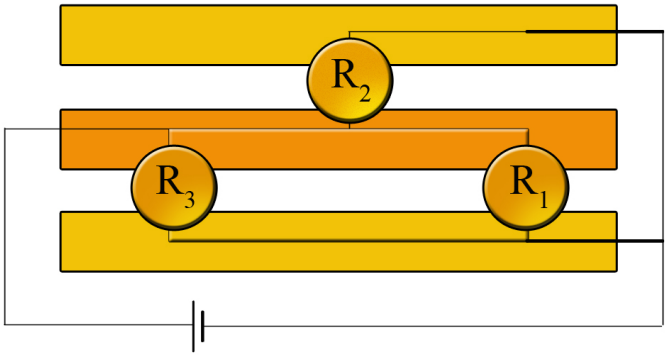

5.2.6 Representative sketch of the circuit used to measured the tunneling resistance of the different nanoparticles.

The experimental setup used was the same presented in Chapter 5.1.1 (first setup). Over 150 electrodes were measured. Figure 5.2.7 presents the logarithm of the inversed resistance for the samples tested. For further studies, only nanotrenches showing values lower than $1\mu\Omega^{-1}$ were taken into consideration, since higher values were most probably related to nanotrenches' defects or Au-Au contacts between electrodes and nanospheres. Depending on the statistical population of measurements,

four main resistance regimes (1000-100nΩ^{-1}, 100-10nΩ^{-1}, 10-1nΩ^{-1}, 1n-100pΩ^{-1}) were chosen with the same orders of magnitude to be able to perform statistical characterization.

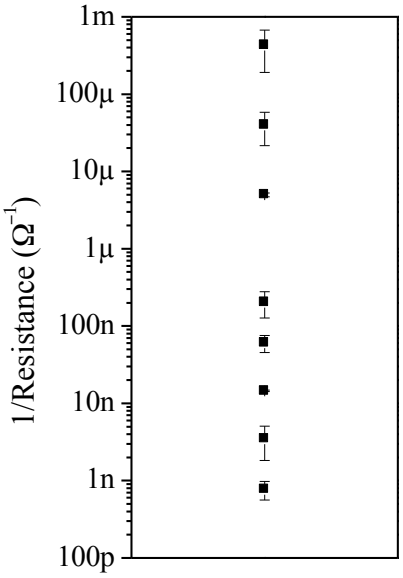

Figure 5.2.7 Inverse of the resistance for the tested electrodes.

After deciding the electrode criteria, the designate ones were further tested, by applying UV light. As previously reported[5] the illumination with UV light should decrease the tunneling resistance, as an effect of the isomerization of AZO from the *trans* to the *cis* isomer. Of the 75 non-connected electrodes under study, 27 showed resistances in the chosen ranges. Of them, 24 showed a decrease of resistance over irradiation while 3 showed an increase (Figures 5.2.8 and 5.2.9). The amount of increase nevertheless was not highly reproducible from electrode to electrode.

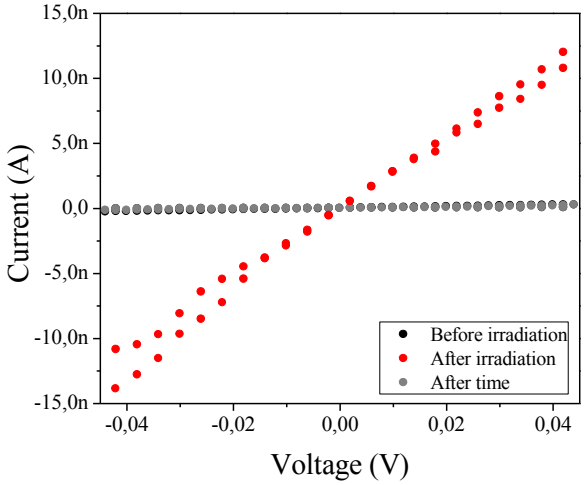

Figure 5.2.8 IV characterization of a full electrode showing low current. In black just after nanospheres deposition, in red after UV irradiation, in grey after 24h in the dark to allow relaxation

from the *cis* to the *trans* form. IVs before irradiation and after 24h time superimpose.

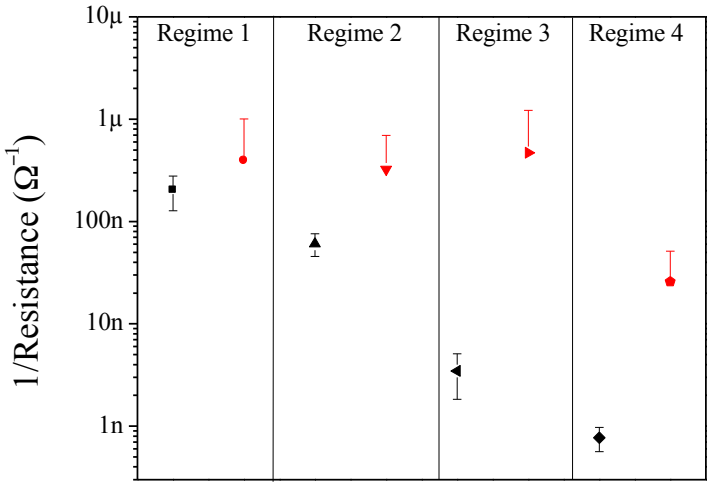

Figure 5.2.9 Inverse of the resistance for each chosen regime, in black before irradiation and in red after irradiation with a 365nm source.

In conclusion, the tested nanotrench electrodes gave resistances in four different regimes, most probably related to the amount of nanoparticles embedded in the gap. 88% of the cases show consistent behavior with UV irradiation.

5.2.2 Conductive-AFM measurements and full characterization

To get a better insight into the behavior of the system, and in particular of a few nanoparticles, C-AFM was the elected technique, as it allows: surface visualization, conduction characterization via mapping of the overall surface and acquisition of single IVs. Figure 5.2.10 shows an example of a typical result obtained by C-AFM. The upper image shows the height and the lower image the current. Every other electrode was connected via silver paste to the bias, reason why one out of two always showed much higher conductivity. The left scale presents the relation between color and conductivity in the current image. The image, and in particular the center part of each electrode, gives immediate information on the amount of spheres connecting the electrodes and the current involved, i.e. the typical tunneling resistance of the molecule considered. It is important to exclude from the generalization the borders of the electrodes since a higher current in this position might arise from a geometrically intrinsic fault of the technique itself, i.e. higher contact when the tip faces an object during a mapping.

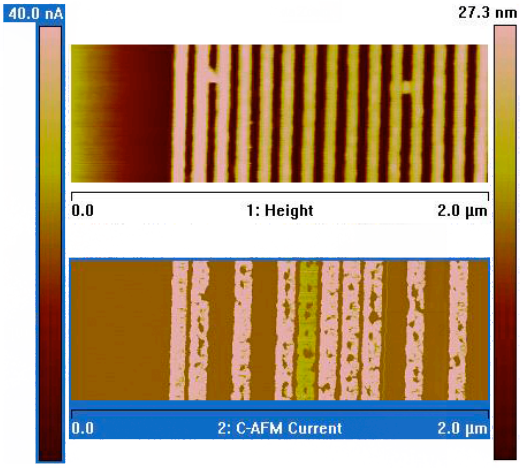

Figure 5.2.10 TOP: height image of nanotrenches interconnected by spheres; BOTTOM: current mapping of the same electrode.

To prove that the information obtained is not related to defects or mistakes in measurements, but to different amount of current, Figure 5.2.11 shows the base 10 logarithm of the current and the height profile of the same electrodes shown in Figure 5.2.10. The necessity of plotting in logarithm scale arises from the high difference in current between connected and not connected electrodes, due to the generally high resistance of organic molecules, even if fully conjugated.[10] The height profile (Figure 5.2.11 1)) confirm the same actual height for the electrodes considered independently on which one is connected while the current profile (Figure 5.2.11 2)) shows as expected higher current for the connected electrodes (red) while the not-connected (black) show a current profile dependent on the number of nanoparticles connecting the electrodes.

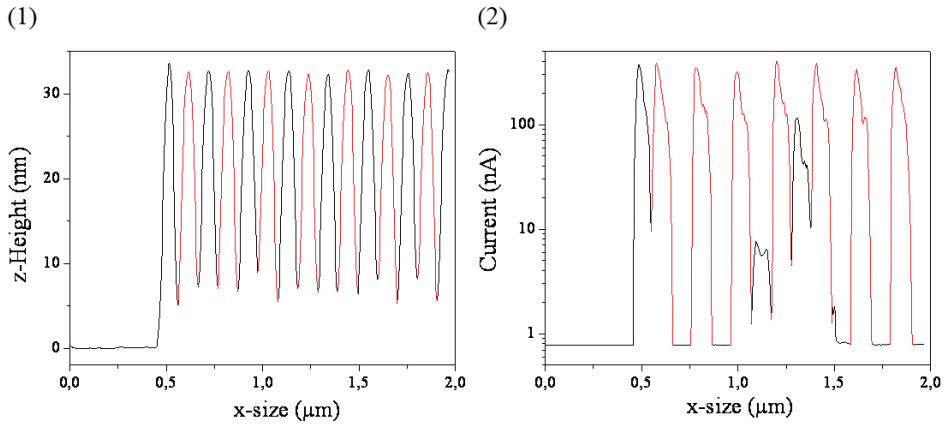

Figure 5.2.11 Average height (1) and current (2) profiles over 171 acquired lines. The current is plotted in base 10 logarithmic scale. The black lines represent the not-connected electrodes and in red the connected electrodes.

To then obtain quantitative information on the junctions considered and to prove how the current profiles can be used as a fast statistical check of a full electrode, a series of IVs was acquired. In figure 5.2.12 the points where the IVs were acquired are superimposed to the previously acquired AFM image. Three points outside the electrodes were always registered to give information about the leakage current of the currently studied device. A four points series for each electrode was then measured to perform statistics.

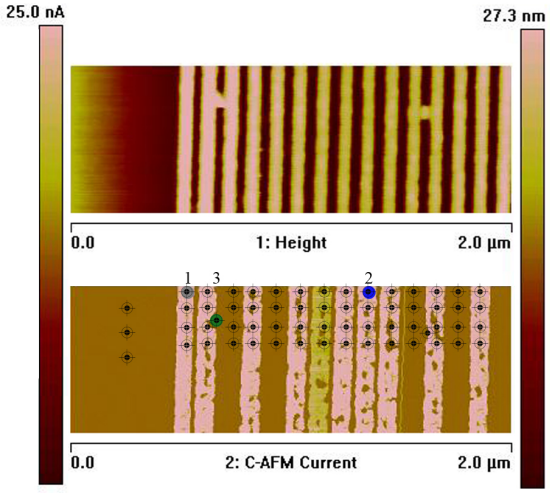

Figure 5.2.12 TOP height image of the nanotrenches. BOTTOM: current image superimposed with the picture of the position where the single IVs measurements were performed. Every black sign corresponds to one position where the IV characteristics have been measured. The positions signed with the grey (1), blue (2) and green (3) corresponds to the IVs in Figure 5.2.13

The possible IVs obtained are presented in Figure 5.2.13

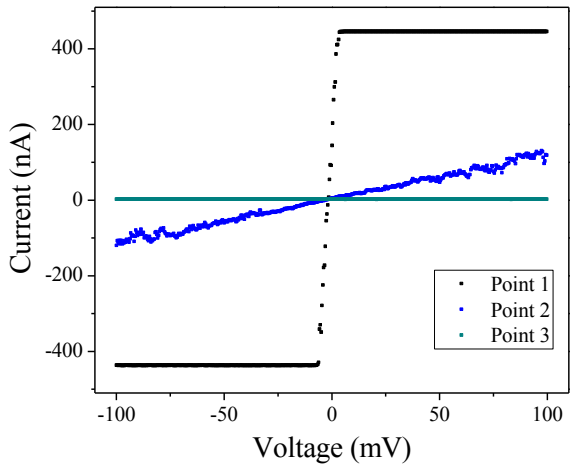

Figure 5.2.13 IVs point by point acquired by C-AFM, different possibilities depending on the connection between the substrate and the AFM tip.

In this kind of measurement, a main factor requiring consideration is the interaction tip-substrate. Unfortunately the electrode's gold roughness measured over 4, 0.125μm^2 areas was 5.95±0.65nm. Such a high roughness induces worse SAMs packing and not always optimum interaction tip-surface.

As shown in figure 5.2.13 there are the possible scenarios:

1. Direct connection of the tip with gold creating short circuits.
2. Ohmic behavior in a certain applied bias range typical of resonant tunneling, increasing the bias range non linear behavior was observed.
3. No good connection between tip and substrate with consequently no measured current.

For these reasons it was decided to exclude all too high (shorts circuits) and too low (no interaction) values. When a good connection was achieved measurements over 4 points at about 50 nm distance from each other, when no nanoparticles were present in that specific area, showed almost identical behavior.

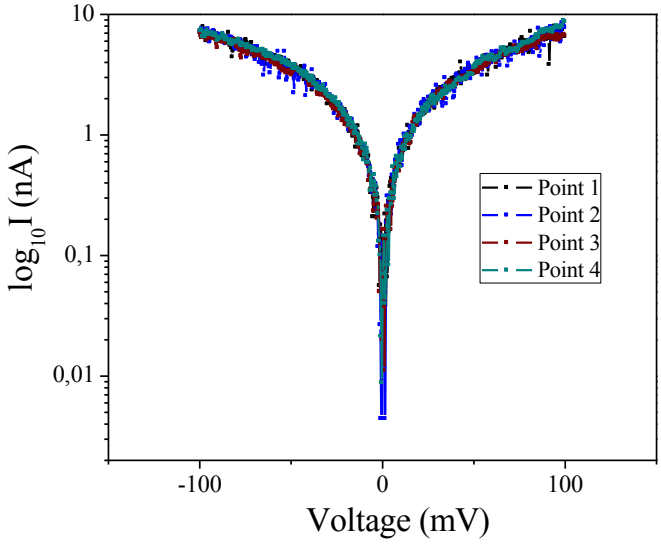

Figure 5.2.14 IV characteristics acquired in four different points on a single electrode, except rare cases the IVs are superimposable..

244 junctions were measured, 122 of which were not connected, 43 of which were in the chosen resistivity range.

Two are the main results obtained until now. A linear behavior of the inverse of the resistance versus the number of particles (Figure 5.2.15) and non-resonant tunneling behavior of the IV characteristics profiles, similar to the ones already reported in literature for the same molecule.

The linear behavior presented in Figure 5.2.15 is consistent with the circuit

model of a number of equal resistances connected in parallel. The behavior of the IV characteristics is consistent with a non-resonant tunneling behavior.

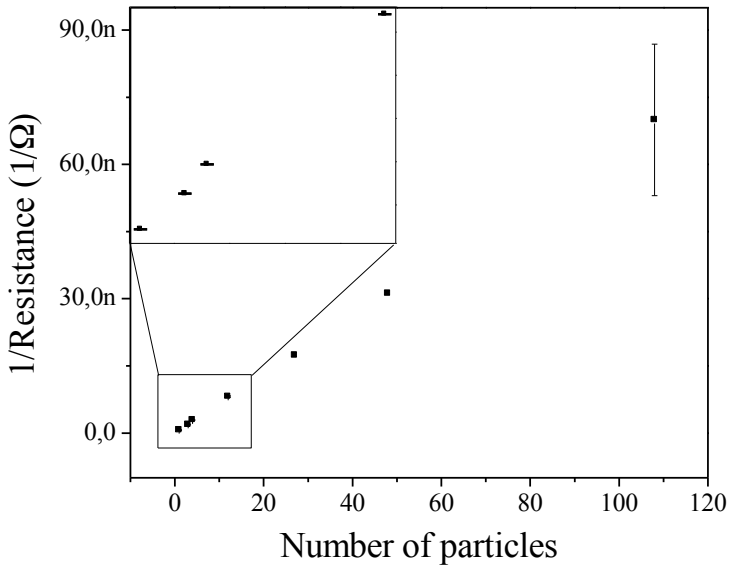

Figure 5.2.15 Graphical representation of the inverse of the resistance over the number of particles.

To better understand the system a sketch is presented in Figure 5.2.16. In the case of a single particle three are the resistances in series that need to be considered.

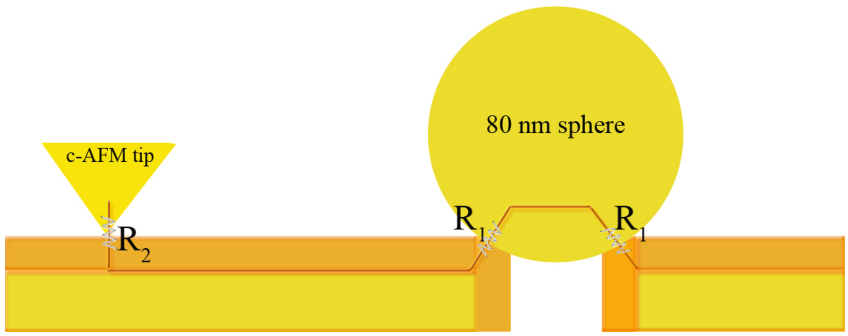

Figure 5.2.16 Schematic representation of the resistances involved when a single nanoparticle is considered.

The total equation can be then written as:

$$R_{TOT(1-Sphere)} = 2R_1 + R_2 \tag{5.1}$$

$$R_1 = R_{0,1}e^{\beta d} \tag{5.2}$$

Here, R_2 is equivalent to the resistance measured through the molecular SAM and R_1 is the resistance measured for one junction electrode-nanoparticle.

R_2 can be extracted from the intercept at 0 of Figure 5.2.15, since the dependence of the total resistance on its contributions for n particles follows equation 5.3:

$$R_{TOT\ (n-Spheres)} = n(2R_1) + R_2 \qquad (5.3)$$

The R_2 value extracted is $8.5\times10^8 \pm 6.8\times10^7$ Ω.
Coming back to the 1 junction case, considering R_{TOT} measured 1.54×10^9 Ω and substituting in (5.1), R_1 will be 3.65×10^8 Ω.

From the measures performed, an estimation of β and $R_{0,1}$ is not possible, but it is possible to roughly estimate if the value extracted is consistent with the system studied.

By employment of the β extracted via Hg-drop electrodes[4] and c-AFM[5] for this molecular system a contact resistance in the range of 10^4 is evaluated, in accordance with the c-AFM measurements.[5]

This is anyway a rough estimation and until the statistical acquisition of the 50 nm gap junctions when irradiated with UV, *i.e.* evaluation of the *cis* form, will be accomplished no conclusive result is ensued.

5.2.3 Conclusions

In summary it has been possible to create an easy and effective way to get high statistics over Me-molecules-Me junctions, the results obtained are consistent with the one expected for such system but a comparison with a lower molecular length in order to evaluate the non-resonant tunneling decay constant and the contact resistance is still ongoing. The technique employed is nevertheless promising in order to perform a deep and fast statistical study of Molecular Electronics devices.

Appendix

The 100 nm gap nanotrenches were prepared on both cover glass (0.13-0.17 nm thick) and Si/SiO_2 wafers (550nm thermal SiO_2 to prevent electrical shorts).

The electrical measurements were performed via electrometer, Keithley 2536, interfaced by in-house developed software.

The electrical measurements fro below the sample were performed via inverted optical microscope with LED light source focused on the sample through the microscope objective (N.A. = 0.65) when using transparent substrates and from the top through the illuminating condenser (N.A. = 0.55) when using Si/SiO_2 wafers.

Sicastar®Monodisperse silica Microspheres with mean diameter ranging from 100 nm to 1.00 μm (Micromod) and Polystyrene monodisperese microspheres (Polysciences) mean diameter 1.00 μm were employed for the microsphere trapping as explained in Chapter III.

All the intermittent-contact (tapping) mode AFM images were acquired under ambient conditions by employing a Digital Instruments Dimension 3100 AFM equipped with a Nanoscope IV controller. The chosen cantilevers were standard silicon with a nominal force constant of 40N/m (Veeco MPP-11120).

All the conducting AFM measurements were acquired by using the same AFM device but equipped with a C-AFM add-on module. The cantilevers employed were NANOSENSORS PPP-CoNT-Pt-50, 0.02-0.77 N/m, Pt/Ir coating both on tip and detector side.

The irradiation lamp was a UV lamp with l_{max} of emission centered around 366 nm (Benda NU-8 KL) 87 μW/cm^2.

References

1 Tran, E., Rampi, M. A. & Whitesides, G. M. Electron transfer in a Hg-SAM//SAM-Hg junction mediated by redox centers. *Angewandte Chemie-International Edition* **43**, 3835-3839 (2004).

2 Mativetsky, J. A., Palma, M. & Samori, P. Exploring electronic transport in molecular junctions by conducting atomic force microscopy. *Topics in Current Chemistry* **285**, 157-202 (2008).

3 Dadosh, T. *et al.* Measurement of the conductance of single conjugated molecules. *Nature* **436**, 677-680 (2005).

4 Ferri, V. *et al.* Light-powered electrical switch based on cargo-lifting azobenzene monolayers. *Angewandte Chemie-International Edition* **47**, 3407-3409 (2008).

5 Mativetsky, J. M. *et al.* Azobenzenes as light-controlled molecular electronic switches in nanoscale metal-molecule-metal junctions. *Journal of the American Chemical Society* **130**, 9192-9193 (2008).

6 Elbing, M. *et al.* Single Component Self-Assembled Monolayers of Aromatic Azo-Biphenyl: Influence of the Packing Tightness on the SAM Structure and Light-Induced Molecular Movements. *Advanced Functional Materials* **18**, 2972-2983 (2008).

7 Comstock, M. J. *et al.* Reversible photomechanical switching of individual engineered molecules at a metallic surface. *Physical Review Letters* **99** (2007).

8 Faramarzi, V. *et al.* Optically switchable molecular device using microsphere based junctions. *Applied Physics Letters* **99** (2011).

9 Kim, T. W., Wang, G. N., Lee, H. & Lee, T. Statistical analysis of electronic properties of alkanethiols in metal-molecule-metal junctions. *Nanotechnology* **18** (2007).

10 Wang, G., Kim, T. W., Jang, Y. H. & Lee, T. Effects of metal-molecule contact and molecular structure on molecular electronic conduction in nonresonant tunneling regime: Alkyl versus conjugated molecules. *Journal of Physical Chemistry C* **112**, 13010-13016 (2008).

Chapter 6. Photoresponsive Transistors

6.1 Aim of the project and chosen materials

A second application of the studied toolbox involved creating multifunctional Organic Field Effect Transistors (OFETs).

It was recently demonstrated how AZO molecules can be integrated in OFETs by chemisorption of an azobenzene SAM on the Au source and drain electrode to confer dual functionality, i.e. gate and light response.[1] The transistor showed photochemical control over the charge injection and extraction at the metal-semiconductor interfaces in a process modulated by charge tunneling. Unfortunately the process allowed a charge photo-modulation up to only 20%, and a maximum of three modulation cycles were possible.

To improve this device, we targeted two aims: a higher current modulation and higher number of cycles. Increasing the current modulation allows higher sensitivity detection broadening the application fields of photo(UV)-responsive devices. Increasing the number of possible cycles allows actual use of the device for applications and long-lasting performances.

To accomplish such goals it was evident that the device geometry needed to be changed.

General information on OFET fabrication and the recent discoveries are presented in Chapters 2 (Introduction) and 3 (Methods).

On the other hand, Au nanoparticles, as presented in Chapter 2, are well known to have a size-dependent electronic structure and, when integrated in devices, a high and reversible charge retention ability that can be exploited for memory-effect devices.[2]

Instead of relying on the injection, the chosen way to photo-modulate the transport through the channel is based on the incorporation of Au nanoparticles coated with AZO moieties in a polymeric semiconductor. As a model system a well known semiconducting polymer, i.e. poly(3-hexylthiophene) (P3HT), has been chosen particulartly in view of its high mobility[3].

For the sake of comparison the study was extended to a nanoparticle system coated with non-photoresponsive SAM, i.e. a mixture of dodecanethiol and S-[4-[4-(phenylethynyl)phenyl]-ethynyl]benzene-thiol (OPE) that was synthesized in the same size of the AZO coated gold nanoparticles to be able to obtain comparable results. OPE molecules show interesting electronic properties, due to the fully conjugated backbone[4] and can be used as non-photoresponsive comparisons of AZO.

As described in Chapter 4 AZO protected AuNPs show a UV-irradiation dependent aggregation/density in solution. It was then decided to exploit this property to tune the nanoparticles' dispersion in the blend and get information on the charge retention dependence on the aggregate size.[5]

Practically speaking, to gain a complete understanding we have to base our studies on OFETs incorporated in the channel: (i) bare P3HT, (ii) P3HT blended with not-photoresponsive nanoparticles and (iii) P3HT blended with photoresponsive nanoparticles, with higher or lower degree of aggregation.

Figure 6.1.1 shows the chemical formula of AZO and OPE (a and b), a sketch of the differently coated nanoparticles (c and d) and an illustrative cartoon of the designed transistor (e).

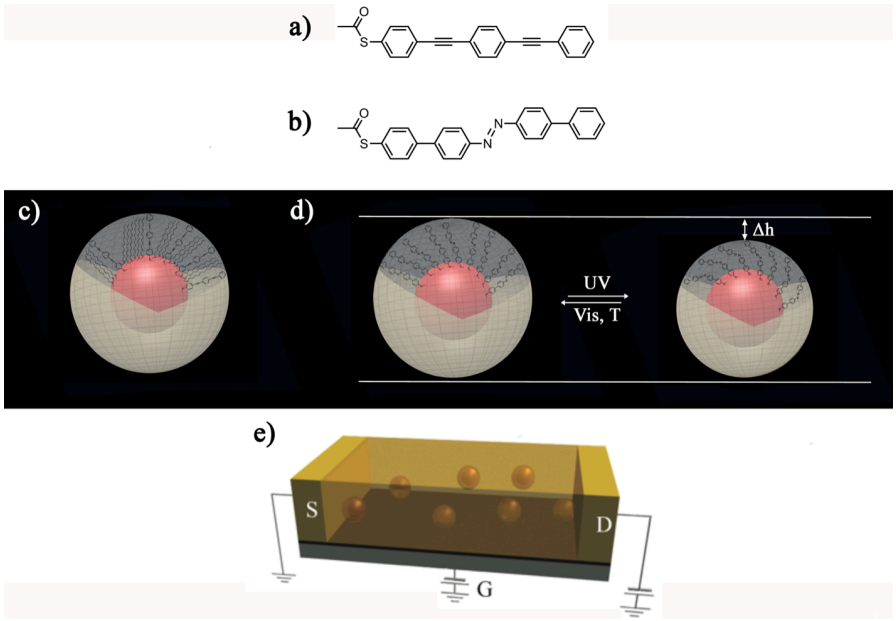

Figure 6.1.1 Illustrative description of the different components of the conceived transistor. (a) and (b) chemical formula ofacetyl-protected AZO thiol and acetyl-protected OPE thiol, respectively; (c), (d) and (e) schemes of the different kind of nanoparticles blended in the semiconductor namely OPE-NPs, AZO(*trans*)-NPs and AZO(*cis*)-NPs where the isomerization process of AZO moieties (mediated by UV light in the forward or visible light and T for the reverse reaction) on nanoparticles is highlighted ; and (e) general design of the transistor.

6.2 Sample Preparation

A general sample preparation method consists of six basic steps:

- Substrates cleaning
- Transfer of substrates and reagents in inert atmosphere
- Solvation of semiconducting material (with or without nanoparticles)
- Spin- coating of the semiconductor on the cleaned substrate
- Thermal annealing (to evaporate the solvent)
- Measurements

In this general approach the critical steps were mixing and solvation of the chosen semiconducting polymer with the AuNP.

To be able to elect the best combinations of NPs and P3HT concentrations, preparation method and solvent ratio, the devices performance was studied as a function of the relative amount of nanoparticles, the type of SAM coating the

nanoparticles and the homogeneity of film morphology. Over 150 samples were prepared featuring a total of 12 different preparation methodologies, 24 different concentrations of nanoparticles and P3HT, 4 different solvent ratios and 5 different systems.

One of the most challenging studies involved the nanoparticles concentrations in the blend. As an example, Figure 6.2.1 shows the different nanoparticles concentrations tested for the final chosen samples and the optical images of two transistors as proof of the high inhomogeneity of the film when increasing the nanoparticle concentration.

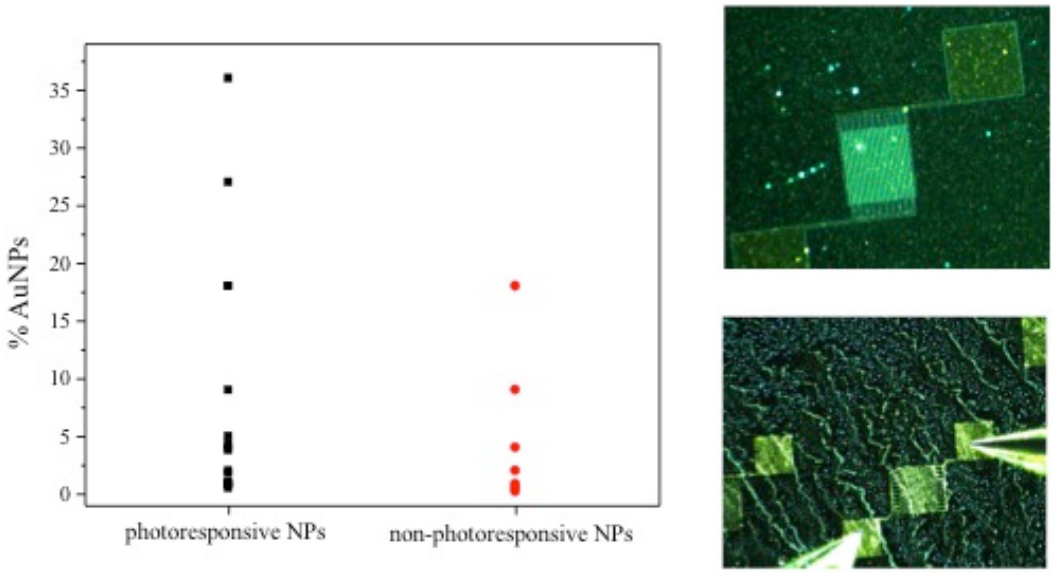

Figure 6.2.1 Left: representative visualization of the different nanoparticle concentrations tested to obtain the best performance. The NP % in the blends varied between 0.2 to 40%; Right: two optical images of tested transistors.

It was found that devices integrating differently coated nanoparticles exhibited a marked field-effect i.e. dependence of the drain current from the gate voltage, only up to a certain threshold concentration in the blend (C_{TH}). Beyond C_{TH} a decrease in the source-drain current (I_D) occurred, probably due to progressively increasing dimension of the aggregates resulting in a conjugation disruption of the π-π stacked P3HT architectures or to a spatially extended electronic trap.[6] Figure 6.2.2 shows this specific effect on a representative sample.

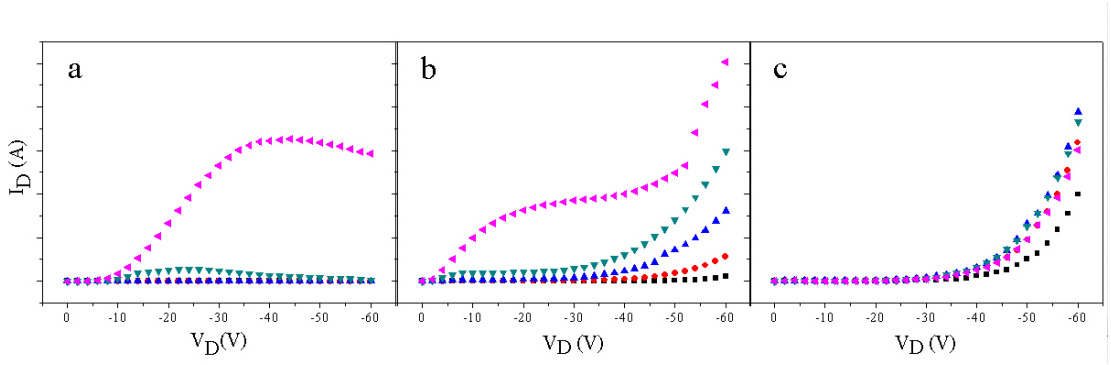

Figure 6.2.2 Output characteristics for a representative AZO coated NPs/P3HT based device increasing the NPs% (a) 0.75wt.%NPs, (b) 2.00wt.% NPs, (c) 4.00wt.% NPs.(V_G = 80, 40, 0, -40 and -80 V, L= 5μm).

In light of such a key role played by aggregation, the highest concentration that, once blended, showed a gate-response was used for each sample type.

After considering all the factors involved, two methods were chosen to prepare the OFETs: Method 1 (M1) in dark, and Method 2 (M2) under UV illumination. Both methods were performed in an inert nitrogen atmosphere.

The general procedure consisted of blending the solution of AuNPs in toluene with the solution of P3HT in $CHCl_3$ in proportion 2:1. This ratio was chosen to limit solubility issues, solvent related, both for P3HT and nanoparticles. Depending on the preparation method two different AZO-based devices were obtained, due to the different aggregation propensity presented in Chapter 4.[5] The main differences were from the aggregation and the field effect performances point of views. The AZO devices prepared with M1, keeping the AZO moiety during blending and deposition in its *trans* configuration will be named "a-AZOAuNPs" (where "a" stands for **a**ggregated) while the AZO devices prepared with M2, allowing the AZO moiety to be in its *cis* configuration and so disaggregated will be called "s-AZOAuNPs" (s meaning **s**olvatated). Transmission electron microscopy (TEM) micrographs of precursor octadecanthiol (named Alk) coated AuNPs, s-AZONPs, a-AZONPs and OPE-NPs are presented in Figure 6.2.3, providing evidence for the similar size of the observed features in s-AZONPs and OPE-NPs and of the dissimilar aggregation propensity of s-AZONPs and a-AZONPs.

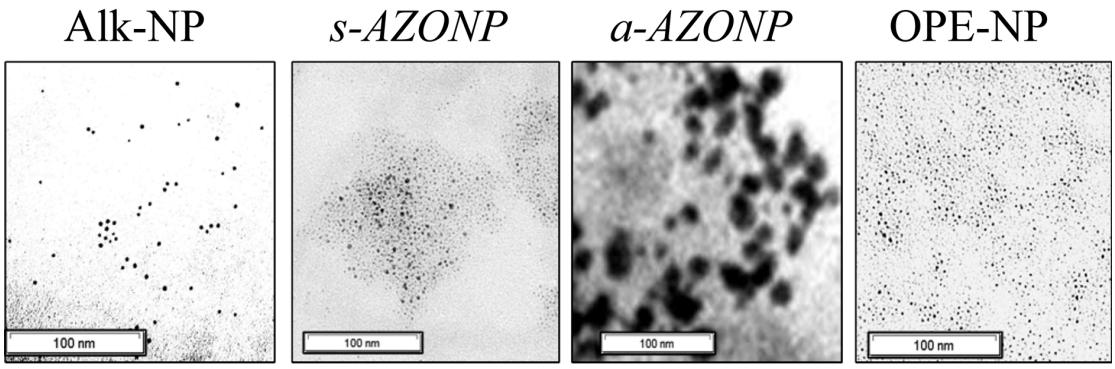

Figure 6.2.3 TEM images of precursor octadecanthiol (named Alk) coated AuNPs, *s*-AZONPs, *a*-AZONPs and OPE-NPs not blended.

Considering the C_{TH} criterion, the wt.% of NPs chosen for s-AZONPs was 18 and only 1 for a-AZONP (due to its high aggregation propensity), 18wt.% was also chosen for OPE-NPs to allow optimal comparison with the s-AZONP device.

No non-photoresponsive dye was chosen as comparison medium for a-AZONPs because, due to the high aggregation and the particular, demanding and selective characteristics no optimal medium was found. We decided to consider the close analogy with s-AZONP and draw a comparison between the two.

The details of the preparation methods are:

(M1) Freshly synthesized NPs were mixed with P3HT to have the C_{TH} % of NPs and a final 1 mg/ml solution of P3HT. Once the blends of the solutions were prepared, they were stirred at 60˚C until dry. A toluene:$CHCl_3$ mixture (2:1) was then added and stirred for 30 minutes at 60˚C to achieve combination of the two reactants and to ensure the *trans* state of the NPs. 100 µl of solution was then spin coated for 60 seconds at 1500 rpm on cleaned pre-patterned substrates. Finally, the film was annealed at 50˚C for 1 h.

(M2) Freshly synthesized NPs (dissolved in a solution at the same concentration as M1) were first irradiated with UV light (365 nm, 87 µW/cm^2) for 1 h, then mixed with P3HT to obtain the C_{TH} % of NPs and a final 1 mg/ml solution of P3HT. The solvent was gradually evaporated inside the glove box until dry. Then the solvent mixture was added to the solid and the solution was further stirred in a quartz cuvette for 1 h. 100 µl of solution was then spin coated for 60 seconds at 1500 rpm on cleaned pre-patterned substrates. Finally, the film was annealed at 40˚C for 1 h. Every step of this method was performed under UV irradiation.

Importantly, for each newly synthesized sample the time needed for the *trans* AZO on the nanoparticles to isomerize to the *cis* form was evaluated by UV-Vis. (For a more detailed description of reaction kinetics of AZO on nanoparticles see Chapter 4).

Both OPE-NPs/P3HT and P3HT films were separately prepared following M1 and M2 to allow comparison. No significant variation in the performance of these lasts two devices was observed comparing the two methods.

6.3 Morphological Characterization

Since one of the goals was to study the charge transport within the devices, it was necessary to characterize the morphology of the blend, since charge transport will drastically depend on the presence of ordered domains and aggregates.

In order to obtain direct evidence of the film morphology in the channel two methods were employed: AFM visualization in intermittent contact (tapping) mode of the upper surface of a typical transistor and TEM imaging of the coated nanoparticles when blended with P3HT. The root mean square roughness (R_{RMS}) and the aggregate diameters extracted from the AFM images allow comparison between the different blends, and they confirm the extracted data when coupled with TEM images. Figure 6.3.1 shows the AFM and TEM images of the blends. In the latter, the comparison was done varying the concentration of the nanoparticles on the TEM grid in order to consider 1000 particles, for statistical reasons, for each system. As the TEM micrographs were recorded with a resolution of 0.51nm/pixel, a column width of 0.5 nm was chosen for the histograms. A detailed description of the AFM and TEM techniques can be found in Chapters 2 and 3.

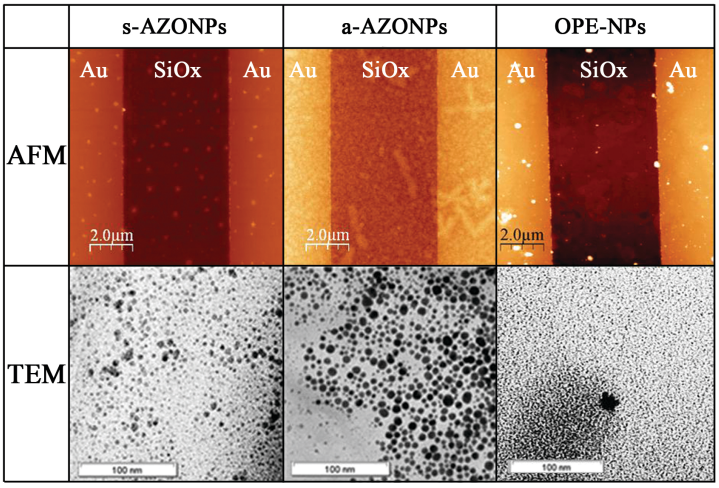

Figure 6.3.1 Top: AFM topographical images of the different typology of OFETs prepared. Bottom: TEM images of the different nanoparticles once blended with P3HT.

Table 1 shows the morphological data extracted from the AFM and TEM images of the blends. The P3HT does not present aggregates. Both AFM and TEM images confirmed close morphological similarities between *s*-AZONPs and OPE-NPs based blends, confirming their use as comparative systems. The *a*-AZOAuNPs based device instead, despite the much lower nanoparticles concentration in the blend shows much higher R_{RMS} and aggregates size confirmed both via AFM and TEM providing unambiguous confirmation of their tendency to aggregate in the film.

Table 1 Comparison between the threshold concentration, the roughness of the surface (extracted from AFM pictures), the aggregated diameters (extracted from AFM and TEM images), and the nanoparticle aggregate size (from TEM).

	P3HT	**OPE-NPs / P3HT**	***a*-AZONPs / P3HT**	***s*-AZONPs / P3HT**
C_{TH}	/	18%	1%	18%
R_{RMS}, AFM (16µm^2 area) [nm]	0.61 ± 0.17	1.11 ± 0.28	4.41 ± 1.02	0.83 ± 0.21
Aggregates diameter, AFM [nm]	/	3.0 ± 2.0	5.5 ± 4.0	2.5 ± 0.5
Nano-objects size [nm]	/	1.3 ± 0.9	5.6 ± 3.4	1.2 ± 0.8
Aggregates diameter, TEM [nm]	/	3.0 ± 2.0	5.5 ± 4.0	2.0 ± 0.5

One of the possible methods to estimate the conjugation level of the P3HT is through UV-Vis spectroscopy.

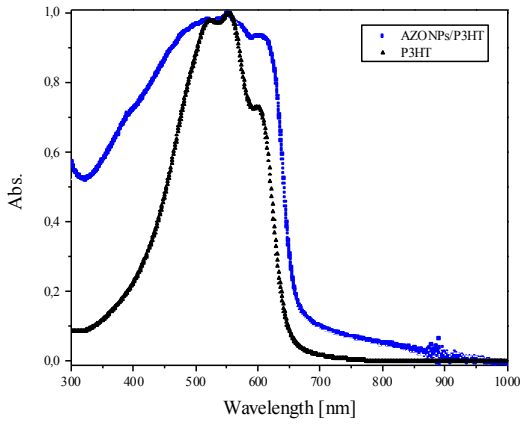

Figure 6.3.2 UV-Vis spectra of (black) P3HT film and (blue) blend *a*-AZONPs/P3HT spin-coated on quartz slides under the same conditions. The different intensities of the peaks between the two samples arise from a different crystallinity of the P3HT with and without nanoparticles.

In order to gain deep insight into the intrinsic morphology at the nanoscale of the blends, spin-coated films of the same solutions on quartz were prepared and UV-Vis spectra acquired. Figure 6.3.2 shows the difference in spectrum between a P3HT film and an aggregated sample of AZONPs.[7]

Unfortunately, a real comparison between the UV-Vis characterization of spin-coated films on quartz and on the transistors SiO_2, is not straightforward. Quartz and thermally grown SiO_2 are in principle chemically equivalents, but they have different roughness. AFM measurements of R_{RMS} of the used quartz slides gives about 2 nm while the thermally grown SiO_2 present in the channel of Fraunhofer transistors has a R_{RMS} equal to 0.2 nm, measured over a 0.5cm^2 area.

It is however possible, since the two materials are from all the other point of view similar, to make a first comparison to understand how blending with nanoparticles interferes with the P3HT crystalline structure.

Don Park et all[7] demonstrated how the addition of a non solvent to a P3HT solution leads to an increase in the absorbance at ~600 nm accompanied by a redshift of the main band at ~450 nm, which can be ascribed to an enhancement of the crystalline nature of the polymer-based film; as a result the transistors fabricated with this solvent mixture exhibited better performance.

Main differences in Figure 6.3.3 between the two UV-Vis spectra are the higher absorbance of AZONPs/P3HT at 365 nm (typical of the AZO moiety), the

different ratio between the peaks at 555nm and 600nm higher in the case of the P3HT and a higher AZONPs/P3HT absorbance at longer wavelengths. All features can be explained in view of a better P3HT crystalline packing in the case of AZONPs/P3HT when compared to pure P3HT films. Taking into account all experimental artifacts such as different surface roughness, broadening of AZO absorption when in solid state,[8] and contribution of the nanoparticles surface plasmon resonance (SPR) which absorption is distribution dependent, we can at least state that P3HT does not spectroscopically present features relatable to higher packing in the basic crystalline structure compared to AZONPs/P3HT.

It is possible, assuming the absorption at higher wavelengths is related with the SPR, to normalize subtracting the effect of the SPR. However, this normalization does not radically change the situation since the AZONP/P3HT peak at 600 nm will still be higher than the one of the P3HT.

In conclusion, the morphological characterization indicates, in comparison with monocomponent P3HT films, that the AuNP/P3HT blend film features greater propensity to aggregate without disrupting the P3HT crystalline domains.

6.4 Electrical Characterization

All the devices were electrically tested in glovebox by employment of an electrometer. Output and transfer characteristics as well as cyclic transfer, time dependents behaviors were first measured for each sample in order to understand the basic behavior, the dependence from the concentration of nanoparticles and the reliability of the methods employed during preparation.

The same tests were as well performed after film irradiation with UV light and after days in dark in order to get the full picture on each device.

An in-depth description of the measurements performed and data extraction is presented in Chapter 3.

The devices prepared showed field effect and were stable over a period of months, if kept inside the glove-box, after preparation.

Limitations of the device were also observed: the application of a bias higher than 40V yielded in some of the nanoparticles based devices the occurrence of bias stress that was evidenced by a lowering of the performance.

Figure 6.4.1 shows the behavior for *a*-AZONPs/P3HT and *s*-AZONPs/P3HT besed devices applying a bias range between -40V and +40V.

As shown in the figure, the bias applied affects the *s*-AZONPs to a lesser extent than the *a*-AZONPs. For devices incorporating *a*-AZONPs, the transistor performance nearly disappears after 1-3 cycles of applied bias. To be able to fully compare the two devices, the voltage was limited to a smaller range even if not all the devices could reach saturation.

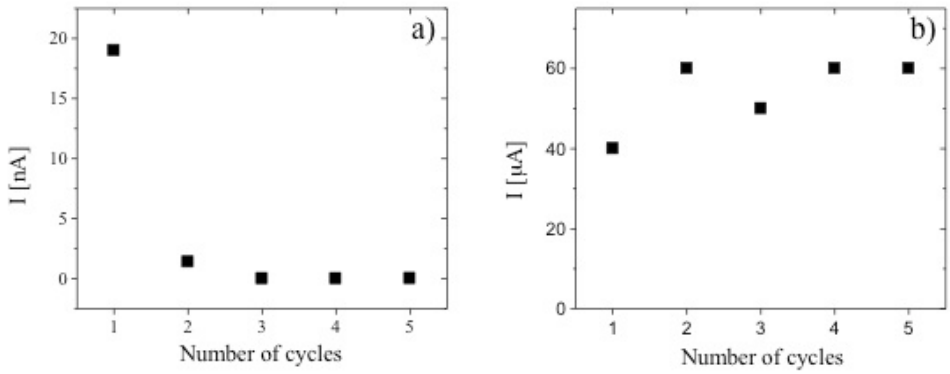

Figure 6.4.1 Current extracted from the output curves (I_D-V_D), applying a V_D= -40V to 40V when measuring the same device multiple times consecutively (a) *a*-AZONPs (b) *s*-AZO-NPs.

The output and transfer characteristics are presented in Figures 6.4.2 and 6.4.3, respectively.

The main differences between the four samples are: film morphology (see section 6.3), the presence of trapping centers, i.e. the nanoparticles and the inter-crystalline domains,[9-11] in the device and the different coating layer in the nanoparticles which are embedded in the polymeric matrix.

Insight into the electric behavior of the nanoparticles is presented in Chapter 2.

As expected, the incorporation of AuNPs in the film reflects in a decrease of drain current when compared to the one-component P3HT based FETs.

A comparison between morphology and the average transistor characteristics (mobility and threshold voltage) are presented in table 6.4.1 and are extracted from at least four different devices for each system before irradiation. It appears that there is a direct correlation between the mean charge carrier mobility (μ_{mean}) value and the morphology of the film, being the largest for the bare P3HT and the lowest for the *a*-AZONPs/P3HT. The *s*-AZONPs/P3HT and OPE-NPs based devices revealed similar

magnitudes, with a four-fold reduction when compared to the neat P3HT devices, respectively.

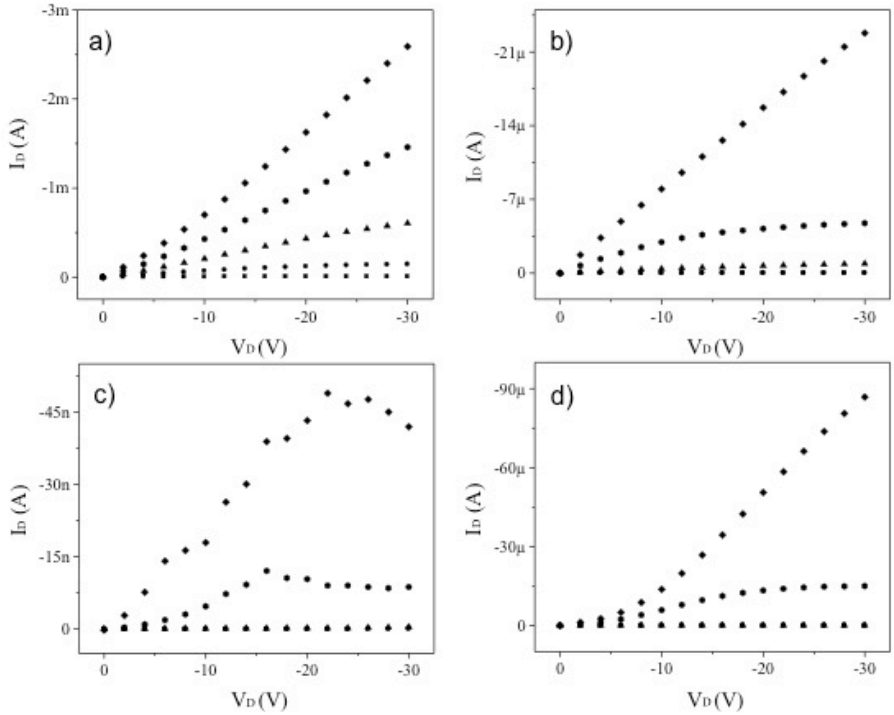

Figure 6.4.2 Output characteristics of (a) P3HT, (b) OPE-NP/P3HT, (c) *a-AZONP*/P3HT, and (d) *s-AZONP*/P3HT recorded at different V_G= -40, -20, 0, 20, 40 V. Channel length (L) = 5 μm.

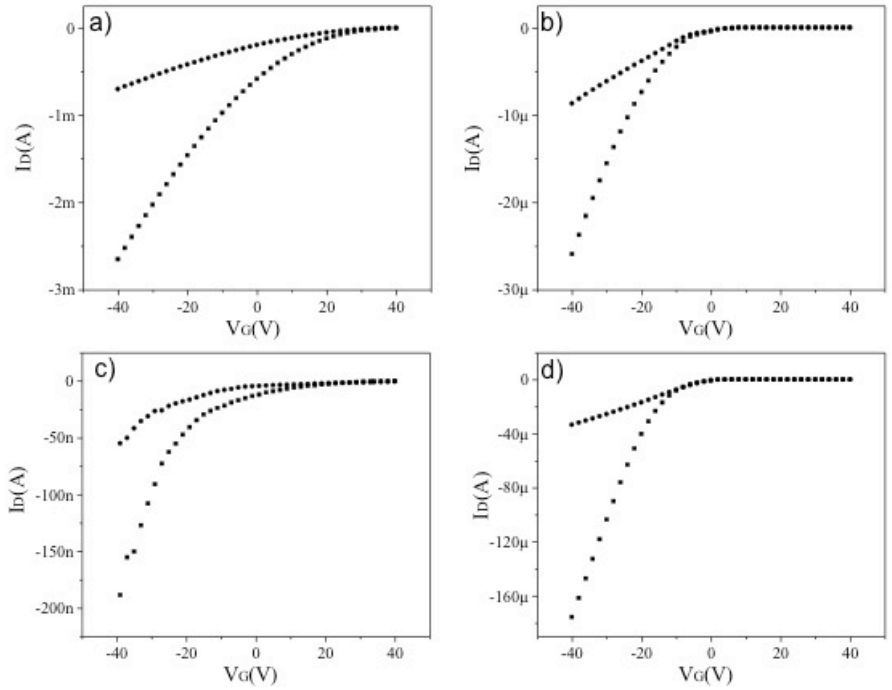

Figure 6.4.3 Transfer characteristics recorded at V_D = -10V and V_D = -30V, L = 5 μm. a) P3HT device, b) OPE-NPs/P3HT device, c) *a*-AZONPs/P3HT device, d) *s*-AZONPs/P3HT device.

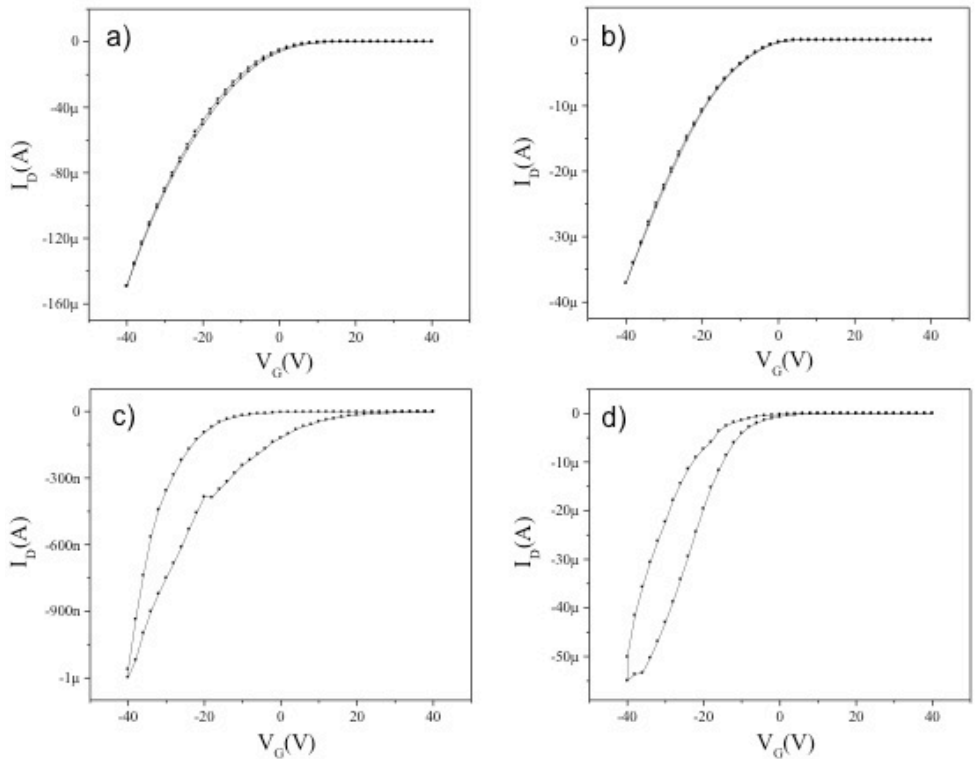

Figure 6.4.4 Transfer characteristics recorded as cycles from V_G=-40V to V_G=+40V and back to V_G=-40V, (V_D= -30V, L=5 μm)) obtained for the four different devices before irradiation: (a) P3HT, (b) OPE-NPs/P3HT, (c) *a-AZONP*s/P3HT, and (d) *s-AZONP*s/P3HT

Table 6.4.1 Comparison between morphology and the average transistor characteristics (mobility and threshold voltage) extracted from at least four different devices for each system before irradiation.

	P3HT	**OPE-NPs / P3HT**	***a*-AZONPs / P3HT**	***s*-AZONPs / P3HT**
C_{TH}	/	18%	1%	18%
R_{RMS}, AFM (on 16μm^2 area) [nm]	0.61 ± 0.17	1.11 ± 0.28	4.41 ± 1.02	0.83 ± 0.21
Aggregates diameter, AFM [nm]	/	3.0 ± 2.0	5.5 ± 4.0	2.5 ± 0.5
μ_{mean} [cm^2 V^{-1} s^{-1}]	3.9E-3±1.6E-3	9.2E-4±4.8E-5	1.2E-6 ±8.4E-7	1.1E-3 ±9.2E-4
μ_{max} [cm^2 V^{-1} s^{-1}]	6E-3	9.9E-4	2.2E-6	2.6E-3
V_{TH} [V]	5.7 ±4.9	4.1±4.4	-0.1 ±16.75	-10.0 ±7.8

All the reported data are extracted as described in Chapter 3.

To further understand the role and typology of the different trapping centers, we focused our attention on the transfer characteristics at different applied gate bias polarities with and without UV illumination. In particular we explored the effect of the different AuNP coating, including the isomerization state of the AZOs. Figure 6.4.4 displays the representative graphs and Table 6.4.2 the associated values. The efficiency of charging and releasing is reflected in the observed relative hysteresis, which can be expected to be larger in presence of more generated/retained (trapped) charges or when the discharging process is longer.[12]

As expected, lower hysteresis was found for the P3HT device; still it does not equal 0, probably due to the formation of bipolarons in the hopping transport through the semiconductor. Moreover, it is important to notice that the solvent used to dissolve P3HT is a mixture of toluene and chloroform, therefore the packing will not be as ordered as in the presence of only chloroform (which is a better solvent for the polymer); more defects will be present implying lower general performances and higher hysteresis.[13,14]

Considering the same nanoparticle sizes, in general, a difference in charge retention performance might rise from: 1) a different coating layer, i.e. originating a different tunneling barrier in the charge injection/extraction from the nanoparticles, or 2) a different dispersion in the polymeric matrix that might involve a variation in the polymeric packing and, more probably, a different charge-retention-time.

As expected, from their intrinsic characteristics and the inhomogeneity of the films, the nanoparticle-based devices show higher hysteresis.

Of all the tested devices, the *a*-AZOAuNPs-based device shows higher hysteresis, whereas similar yet lower hysteresis was found for *s*-AZONPs and OPE-NPs. The slightly smaller hysteresis of OPE-NPs can be attributed to the hydrophobic nature of the alkanethiol SAM able to enhance the crystallinity of the film and to promote less trapping centers in the P3HT yielding a lower hysteresis.

Another possible explanation for the different hysteresis found for the *s*-AZONPs/P3HT and OPE-NP based devices can be the mechanism governing the charge-transport between the semiconductor and the NPs. Two mechanisms are possible: either hopping or tunneling transport.[15,16] The different nature of the coating layer (being either an alkanethiol, a fully conjugated aromatic molecule or AZO) can be expected to influence the tunneling barrier. In principle, the higher the tunneling barrier the lower the charge retained but for longer. Due to the mixed-molecules

nature of the OPE-NPs (synthesized in the ratio 9:1 dodecanthiol:OPE) and in particular the high presence of dodecanthiol, the OPE-NPs will have a higher contribution to the tunneling resistance.

It is reasonable to assume that the above-mentioned reasons will be enough to produce a difference in hysteresis between *s*-AZONPs and OPE-NPs of 2.2V in the dark.

To further differentiate the two systems and to further prove that a charge trapping process in the studied system is indeed possible, the work function (WF) values of the drop-casted films of OPE-NPs and *s*-AZONPs on freshly cleaved mica were determined by photoelectron spectroscopy in air, giving WF values of 4.44 ± 0.05 eV and 4.53 ± 0.07 eV, respectively. In both cases, the energetic barrier difference (mismatch of energetic levels) between the functionalized AuNPs and the HOMO of the P3HT (4.8 eV) slows down the charge detrapping since the lower WF of the AuNP can facilitate the transport (and trapping) of holes from the semiconductor to the NPs, but it disfavors the injection of the holes back to the P3HT.

Table 6.4.2 Mobility and Threshold Voltage values extracted from the hysteresis experiments.

	μ ($cm^2 V^{-1} s^{-1}$)		V_{TH} (V)	
	Fwd.	Bwd.	Fwd.	Bwd.
*s-AZONP*s/ P3HT	5.7E-6 – 3.7E-3	1.6E-6 – 5.6E-3	-8.41 / -29	-7.9 / -26.9
*a-AZONP*s/ P3HT	7.7E-5 – 7.9E-4	1.6E-4 – 5.3E-4	11.8 / -18.3	-11.19 / -21.6
OPE-NPs/ P3HT	8.8E-4 – 1.2E-3	1.1E-3 – 1.2E-3	4.1 / 9.0	3.8 / 8.3
P3HT	3.8E-3 – 3.2E-2	4.0E-3 – 3.3E-2	10.9 / 20.1	8.7 / 20.1

6.5 Dependence on UV irradiation

The response of the transistor to UV light was investigated over several irradiation cycles. Each cycle was composed of three steps involving electrical characterization (1) just after preparation, (2) after UV irradiation and (3) after 24h time in dark (to allow complete back *cis*-to-*trans* reaction). After the first characterization, the *s*-AZONP/P3HT device was kept in dark for 24 hours before starting the first complete cycle. At least three cycles were performed on each device.

Figures 6.5.1 and 6.5.2 displays the typical output and transfer characteristics, respectively, of the third cycle. By choosing the third cycle a valid comparison in the closest possible light and bias stress conditions is ensured.

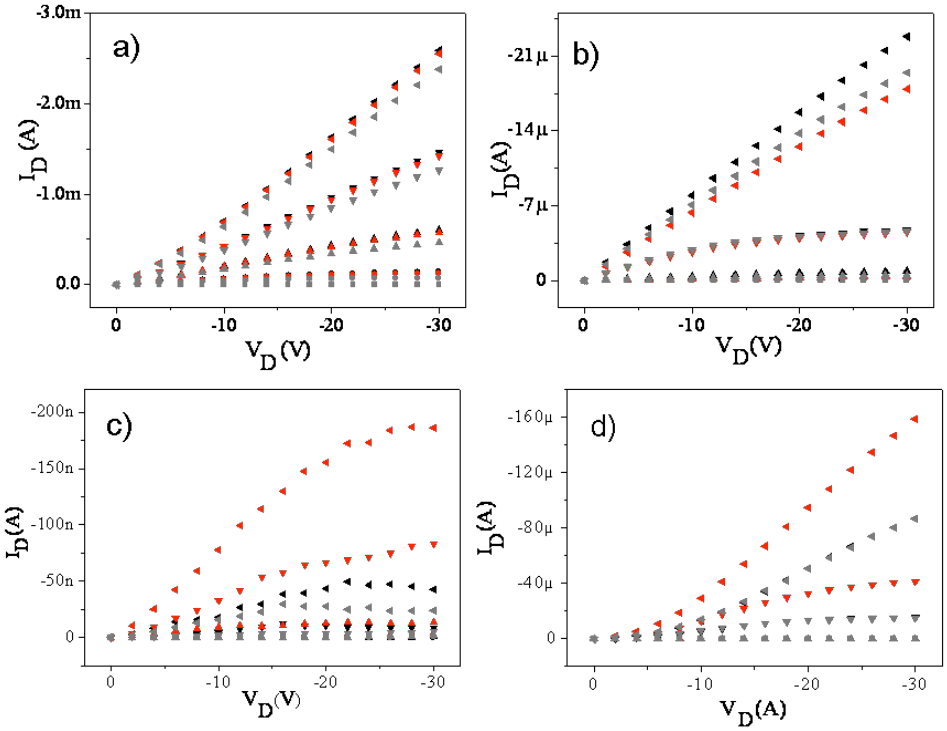

Figure 6.5.1 Output characteristics of (a) P3HT, (b) OPE-NP/P3HT, (c) *a-AZONP*/P3HT, and (d) *s-AZONP*/P3HT recorded at different V_G= -40, -20, 0, 20, 40 V. In black, the initial state (after keeping the device in the dark for 24 hours), in red after 45 min of UV irradiation and in grey after further 24 h in dark. Channel length (L) = 5 µm.

First, all the exploited molecules absorb UV light to a certain extent,. It becomes important to understand how the UV absorption modifies the transport characteristics of each single dye. The chosen p-type semiconductor, P3HT, absorbs in the UV region. The P3HT response to UV light is well documented, for instance

Manceau et al. report the degradation effect of UV light on P3HT, monitored via UV-Vis and IR spectroscopies, over a 10000 hour exposure period in the absence and presence of oxygen.[17] Since in absence of oxygen no real irreversible degradation is documented over the 1000 h time frame and our experiments were performed irradiating for 45 minutes, it is reasonable to affirm that the P3HT does not degrade in the tested experimental conditions while photo-generation of charges may occur.

Likewise OPE molecules absorb in the UV region, but a difference in conduction upon UV-irradiation is not likely to occur.

Even if both OPE and P3HT absorb in the UV region, in this measurement timescale, no evident increase in current could be noticed, instead for the OPE-NP/P3HT devices a decrease was recorded.

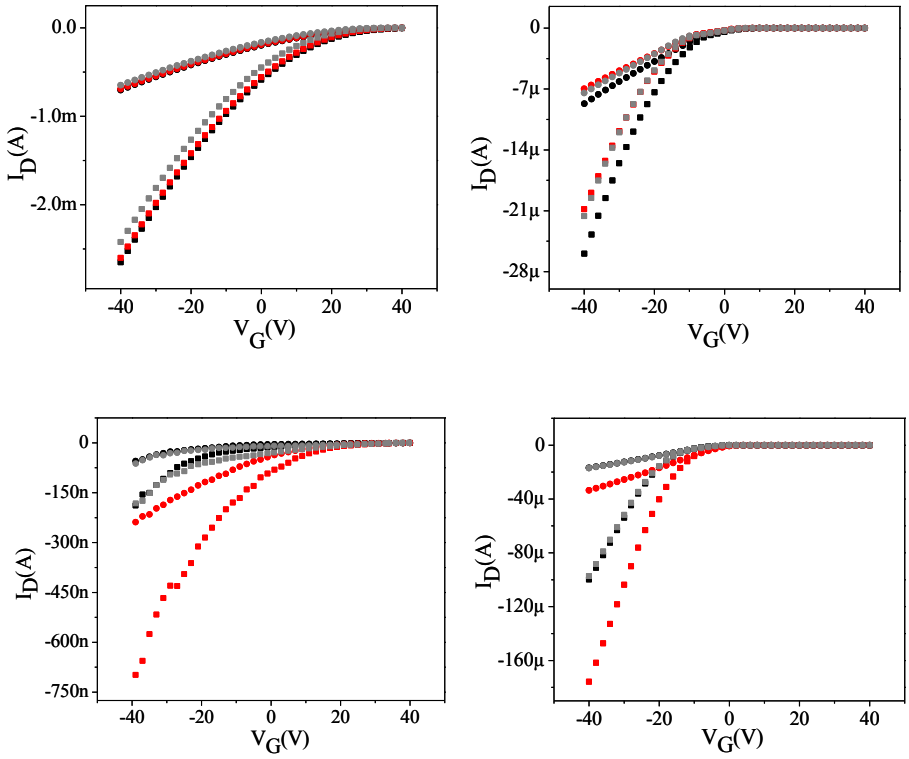

Figure 6.5.2 I_D - V_G characteristics at V_D = -10V and V_D= -30V, L=5 µm. a) P3HT device, b) OPE-NPs/P3HT device, c) *a*-AZONPs/P3HT device, d) *s*-AZONPs/P3HT device. In black, the initial state (after keeping the device in the dark for 24 hours), in red after 45 min of UV irradiation and in grey after further 24 h in dark. Channel length (L) = 5 µm.

After UV light irradiation, the I_D in *s*-AZONP/P3HT exhibits a 7-fold increase, a behavior that may be attributed both to the conjugated nature of the SAM

and to its reduced thickness when adopting the *cis* state,[18] i.e. lowering the tunneling resistance.[19]

Figure 6.5.3 displays the percentage of variation of some characteristic FET parameters as $I_{D,max}$, μ and threshold voltage (V_{TH}) within irradiation. The parameters were extracted from the transfer curves (see Figure 6.5.2). Upon UV irradiation the V_{TH} shifted to higher values in the cases of the AZONPs, which at the voltage applied, translates to a higher amount of charges in the channel, leading to an increased μ and $I_{D,max}$. A decrease of all the % values presented was instead observed for the OPE based device probably due to the long exposure to UV light while P3HT showed almost no change. A possible explanation is that the photo-generated charges in the P3HT rapidly recombine when the P3HT is alone but get trapped in the nanoparticles in the OPE-NPs/P3HT devices.

The largest current variation upon UV irradiation was detected for the *a*-AZONPs/P3HT, but this device showed a drastic decrease in response after a few cycles (maximum 5, in the best case). Such a large fatigue, accompanied by low result reproducibility, is likely due to the high tendency of the nanoparticles to aggregate.

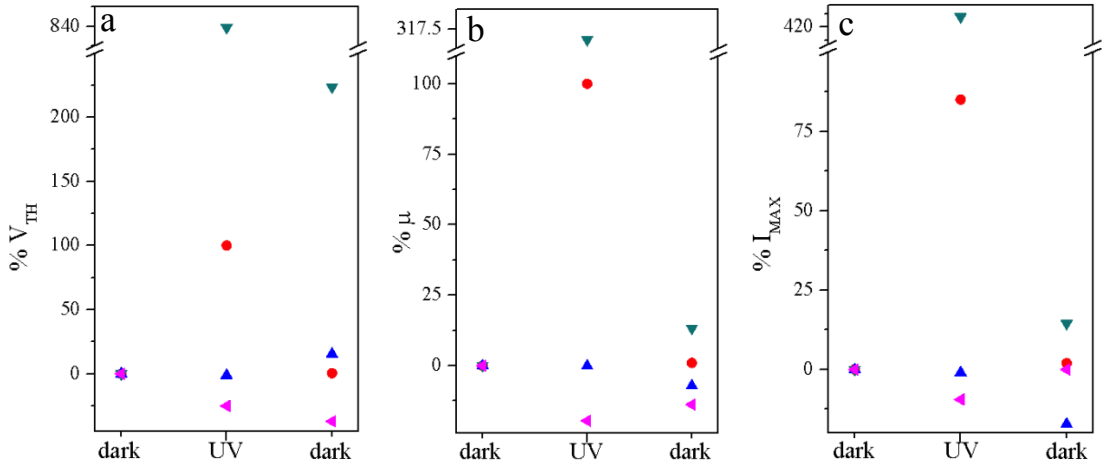

Figure 6.5.3 Maximum percentage of variation during the irradiation cycles for the (a) V_{TH}, (b) mobility (μ), and (c) $I_{D,max}$ (extracted in the linear regime, V_{DS} = -10 V), for the four different devices. Blue: P3HT, in red the *s-AZONP*s, in green the *a-AZONP*s, in magenta OPE-NPs.

Furthermore, it is important to understand if, through irradiation, the process of charging, retention and discharging of the single device shows any difference compared with before irradiation.

The typical curves are presented in Figure 6.5.4 and the statistical data is given in Table 6.5.1.

The P3HT devices show the lower, but still evident, hysteresis. Such light response can be ascribed to an increased number of trapped carriers in the active layer either at the P3HT-SiO_2 interface or in the SiO_2,[20] and to the effect of vacancies on the electrical hysteresis.[21]

In the AZO nanoparticle-based devices the trapping/realizing process becomes more complex under UV illumination. It has been previously shown by c-AFM and Hg-drop electrodes that the tunneling resistance of an AZO molecular junction is higher for the *trans* configuration than for the *cis*, i.e. in dark or under UV irradiation, respectively.[18,22] This phenomenon has been attributed to the smaller thickness of the *cis* form. It is possible to postulate that the same phenomenon is present when the AZO SAM coats the nanoparticles. In this case, a lower tunneling resistance will translate into an easier charge storage and faster release. However, even if in the measurement's time scale the AZO SAM are only partially isomerized, the *cis* molecules will contribute to a higher efficiency of the trapping-detrapping process, producing a smaller hysteresis difference between dark and UV conditions than observed in the OPE-NPs/P3HT based devices.

Another factor that needs to be considered is that the photo-excitation hole density within the film contributes to the drain current shifting the V_{TH} to larger positive values.[23] This phenomenon was observed, even if with different magnitudes, in all the tested devices.

In general, the easier charge trapping/release process of the NPs coated with azobenzene will be faster when the AZO is in the *cis* form than when it is in the *trans* form, i.e. faster under illumination than in dark. One can therefore expect that this effect will create a high difference in I_D between sample illuminated or kept in the dark. The possible photomodulation of current in non-photoresponsive devices, instead, is expected to be caused by the photogenerated charges in the P3HT matrix.

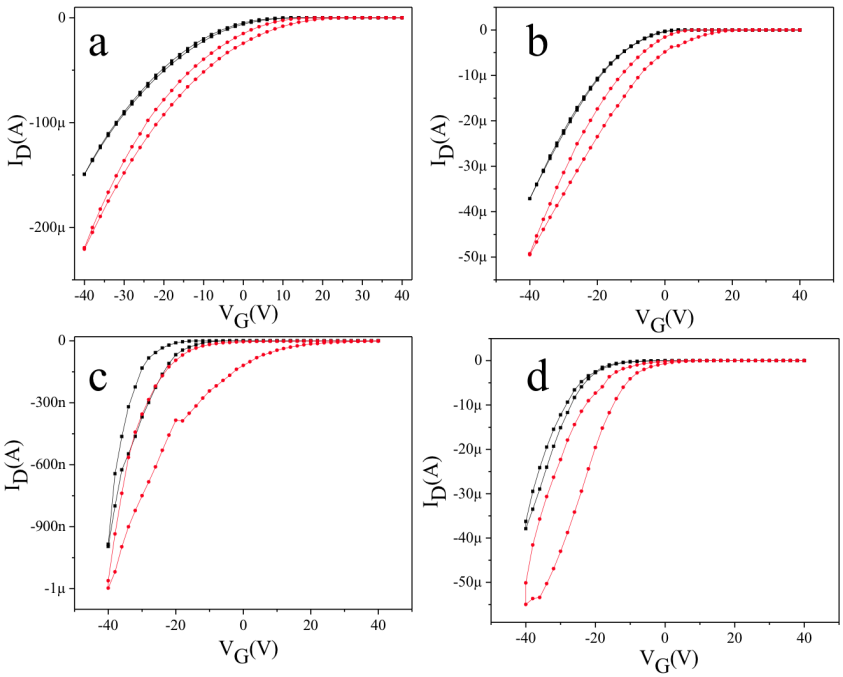

Figure 6.5.4. Transfer characteristics from -40V to +40V (back and forth), (V_D = -30V, L = 5 µm)) obtained for the four different devices; in black when the device is in dark and in red under UV (the measurement started to be recorded after 5 min of irradiation): (a) P3HT, (b) OPE-NPs/P3HT, (c) *a-AZONP*s/P3HT, and (d) *s-AZONP*s/P3HT

Table 6.5.1 Charge carrier mobilities (µ) and threshold voltages (V_{TH}), expressed as a range including the results obtained for the different devices tested for each particular system. The values were extracted from the forward (fwd.) and backward (bwd.) transfer curves for the devices in dark and under UV illumination.

			P3HT	**OPE-NPs / P3HT**	***a*-AZONPs / P3HT**	***s*-AZONPs / P3HT**
µ ($cm^2 V^{-1} s^{-1}$)	**Dark**	**Fwd.**	3.8E-3/3.2E-2	8.8E-4/1.2E-3	7.7E-5/7.9E-4	5.7E-6/3.7E-3
		Bwd.	4.0E-3/3.3E-2	1.1E-3/1.2E-3	1.6E-4/5.3E-4	1.6 E-6/5.6E-3
	Under UV	**Fwd.**	3.7E-3/3.0E-2	7.5E-4/9.0E-4	2.1E-5/3.6E-4	8.8E-6/5.4E-3
		Bwd.	4.6E-3/3.3E-2	1.1E-3/1.4E-3	9.6E-5/8.1E-4	1.1E-5/4.4E-3
V_{TH} (V)	**Dark**	**Fwd.**	10.9 / 20.1	4.1 / 9.0	11.8 / -18.3	-8.4 / -29.0
		Bwd.	8.7 / 20.1	3.8 / 8.3	-11.2/ -21.6	-7.9 / -26.9
	Under UV	**Fwd.**	23.5 / 21.0	19.4 / 22.2	19.0 / -2.6	7.1 / -7.8.0
		Bwd.	14.0 / 21.8	8.8 / 13.9	13.2 / 15.2	7.6 / -25.0

Hysteresys, [V]	**Dark**	0.4±0.3	1.2±0.5	5.5±4.5	3.4±1.3
	UV	3.6±3.4	10.7±0.8	20.5±9.5	12.2±4.6
	Δ	3.2±3.7	9.5±1.3	15.0±14.0	8.8±5.9
Max number of irradiation cycles		> 25	>25	3-5	>25

The *a-AZONP*s/P3HT transistor was not studied further mainly because of elevated fatigue during switching and poor basic transistor performance.

The switching behaviour of the other devices was, instead studied further. To determine the suitable irradiation times the I_D response over irradiation at the chosen gate voltage was monitored over time. Figure 6.5.5 shows the obtained result. An increase was registered that reached saturation within the 5 minute irradiation period. Consequently, cycles of irradiation of 5 minutes UV followed by 10 minutes in dark were performed to allow relaxation of the *cis* form to the thermodynamically more stable *trans*.

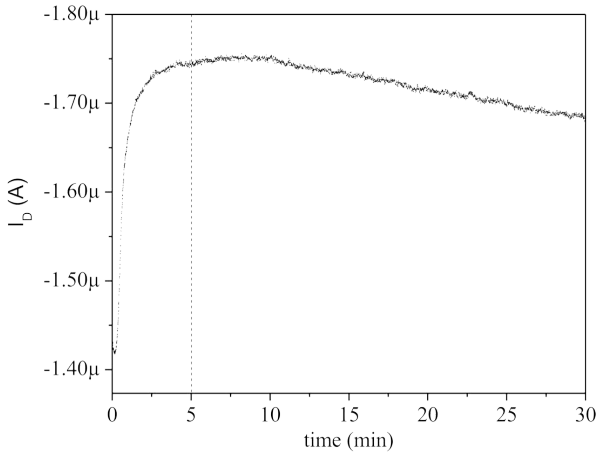

Figure 6.5.5. I_D *vs.* time at V_G= -5 V and V_D= -10V, for the *s*-AZONPs/P3HT base device under UV illumination (L=5 µm)

Figure 6.5.6 shows the behaviour of all the devices studied at $V_G - V_{TH}$ = -4V and V_D = -10V over the described irradiation cycles.

The applied voltage was chosen in order to inject the same amount of charges in each device and drawing a reliable comparison.

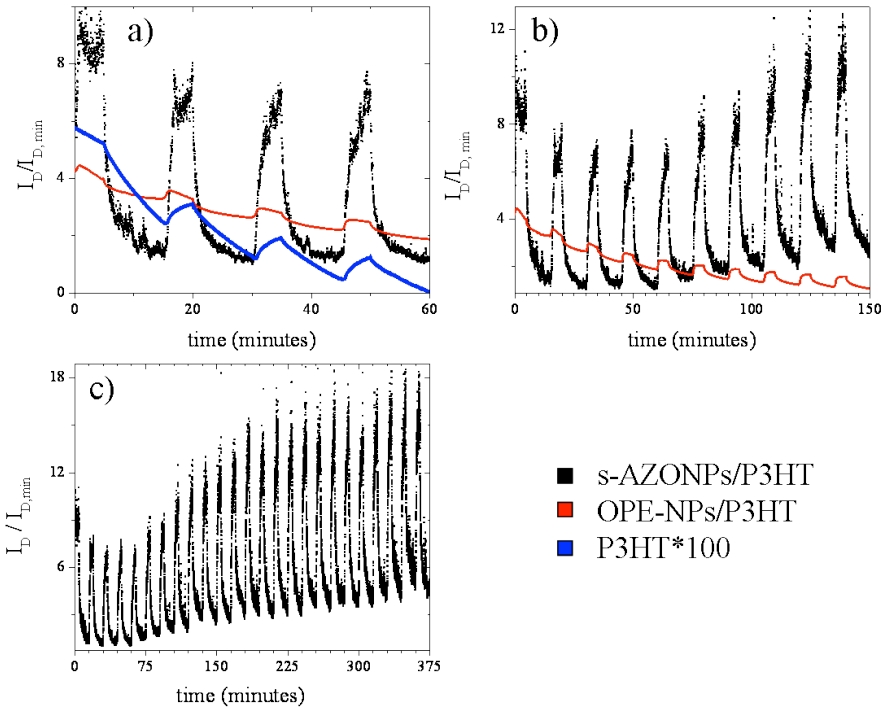

Figure 6.5.6. Photo-response cycles over time of *s-AZONPs*/P3HT (in black), OPE-NPs/P3HT (in red) and P3HT (in blue). For the latter, the $I_D/I_{D,min}$ was multiplied by 100 to allow a better comparison. (a) 4 cycles (b) 10 cycles, and c) 25 cycles. V_G -V_{TH} = -4V, V_D = -10V and L= 5 µm.

The same parameters were employed in the study of OPE-NPs/P3HT and bare P3HT based devices. All of the systems presented the same trend upon UV irradiation, an increase when irradiated with 365 nm light and a decrease once the light was switched off.

A markedly higher variation was detected for the AZO based devices.

The most probable interpretation is that this phenomenon is related to the isomerization of AZO molecules on the surface of the nanoparticles. This isomerization induces a variation of the V_{TH} promoting an increase of charges in the device, i.e. a higher detected current. To prove this statement the V_{TH} variation within irradiation cycles, at the same V_G, was monitored as well. Figure 6.5.7 presents the obtained results. Thanks to these measurements it was determined that the modulation of the current could not only be caused by the V_{TH} shift, whose contribution is smaller than the observed I_D modulation.

Another important observation is that both the bare P3HT and the OPE-NPs devices showed opposite trends overtime compared to the AZO-NPs since the bias stress is not compensated by an increase of current. Interestingly, this decrease in

current in the case of the P3HT device is much higher than in the AuNP. This may be attributed to a charging/discharging processes due to the presence of NPs that are responsible for more constant active charge carriers present in the semiconductor. A deeper study of the dynamics involved in this particular process is underway.

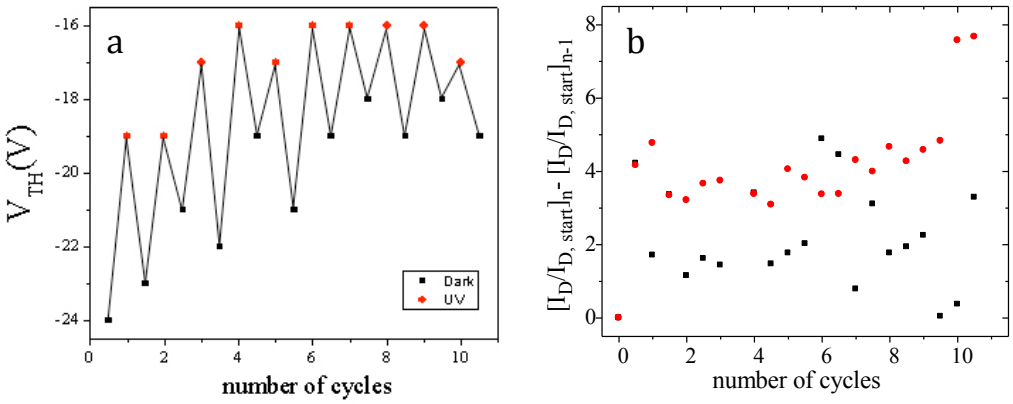

Figure 6.5.7 a) V_{TH} variation during the irradiation cycles performed on the s-AZONPs/P3HT transistor shown in Figure 7 (extracted in the linear regime (V_D=-10V)). b) Comparison of the I_D modulation (extracted in the linear regime (V_D=-10V)) within irradiation cycles in the same device: in red, I_D variation during the irradiation cycles performed on the s-AZONPs/P3HT transistor shown in Figure 7, and in black, I_D maximum obtained after sequential dark-irradiation cycles:

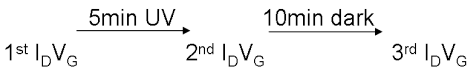

The I_DV_G were acquired in the dark

6.6 Conclusions and outlook

Considering the experimental results, a possible charge transfer mechanism was developed.

Figure 6.6.1 shows a sketch of the device and the possible pathways involved. The charge moves from the source (a) to the drain electrode (h) following the shown path. Each letter indicates a different "node" in the mechanism and symbolizes a change in the charge transport mechanism.

The following transport mechanisms are present in the device: (---) amorphous polaronic variable range hopping (VRH), (---) charge trapping in the nanoparticles, (---) crystalline polaronic VRH. The amorphous polaronic VRH is a typical behavior within the amorphous phases of P3HT, between crystal domains and the charge trapping time depends on the morphology;[9,10,24] The charge trapping in the

nanoparticles is favored due to WF(NPs) = 4.48 ± 0.06 eV and HOMO(P3HT) = 4.80 eV, and confirmed by the higher hysteresis in the "*Back and Forth* IdVgs[12]" and the positive (to higher currents) bias stress's drift of the device. Finally the crystalline polaronic VRH is a trap-free transport typical in the crystalline phases of P3HT.[9,10,24]

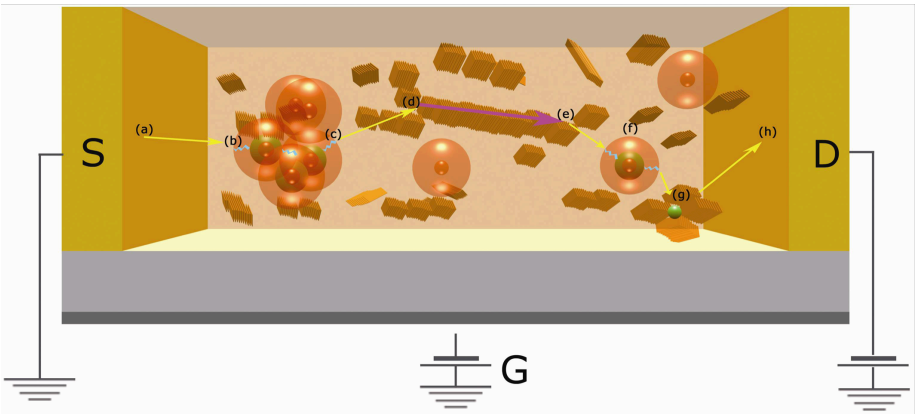

Figure 6.6.1 Cartoon of the charge transport mechanism in the device with (a) being the first electrode, (b) to (c) an aggregate of nanoparticles, (d) the initial point of a crystalline domain in P3HT, (e) the end point of a crystalline domain in P3HT, (f) nanoparticles, (g) inter-crystalline grains trap in P3HT and (h) the second electrode. Interactions between each domain are indicated as follows: polaronic variable range hoping (yellow), charge traipping in the nanoparticles (blue), and trap-free transport (pink).

In summary, the light-modulation of the current in an OFET based on AuNPs blended with P3HT has been demonstrated to be greatly enhanced when the AuNPs are functionalized with a photo-responsive azobenzene based SAM. The light-induced isomerisation between the *trans* and *cis* states of the molecules coating the AuNPs implies a variation of the tunnelling barrier (decreasing from *trans* to *cis* isomer), which plays a crucial role in the efficiency of the charge trapping/detrapping process within the film. Thus this approach makes it possible to confer a dual functionality on an organic transistor as it provides a means to gate the source-drain current through the channel both electrically (through gate control), as in a conventional transistor, and optically (through photochemical control). It also represents an innovative approach to digital commuting between optical and electric signals. Finally, such modulable transistor might be useful for applications in UV sensing.

Future work includes improving charge injection, and thus overall device performance, by adsorbing a SAM on the source and drain electrodes. Additionally, charge modulation can be increased by using a semiconductor that does not absorb in the UV region. It is also possible to modulate the device geometry in order to improve

interfacial transport or charges generation and so the performances. The work presented in this chapter demonstrates significant improvements to OFET device performance by irradiation of a device incorporating AuNPs functionalized with photo-responsive SAMs, laying the foundation for future studies and further device modifications.

Appendix

P3HT was purchased from BASF Chemicals (Sepiolid TM P200). All the reagents, solvents included, except water, were purchased from Aldrich. The MilliQ water was provided using a MQ water filter (Millipore-Direct Q). Biphenylazo derivative was synthesised as previously described.18

All organic field-effect transistors (OFETs (with a bottom-gate bottom-contact configuration) were prepared starting from n++-Si/SiO2 substrates exposing pre-patterned interdigitated gold source and drain electrodes (IPMS Fraunhofer). Before their use, they were rinsed with acetone and then isopropanol in an ultrasonic bath for 15 minutes each to remove the photoresist protecting layer and dried under nitrogen steam.

Spin-coating and electrical characterization were performed at room temperature and in an inert environment (glovebox, with water and oxygen levels below 10ppm) by means of an electrometer, Keithley 2536, interfaced by in-house developed software.

TEM images were acquired with a Philips CM100 transmission electron microscope at 80 kV. Electron micrographs were recorded on a 2000 by 2000 pixels charge-coupled device camera Veleta from Olympus. The particles were deposited by drop casting on top of a thin carbon film that spanned a perforated carbon support film covering a gold-plated copper microscopy grid. The grid was air dried.

Atomic Force Microscopy (AFM) images were acquired with a Veeco Dimension 3100 AFM running with a Nanoscope IV controller. AFM images were recorded in the intermittent contact (tapping) mode under ambient conditions. Standard silicon cantilevers were used (Veeco MPP-11100) with a nominal spring constant of 40 N/m, resonance frequency of 300 kHz and tip radius of 10 nm.

Photoelectron spectroscopy (AC-2; RKI Instruments) was used to measure the work function of the differently coated AuNPs.

The UV-Vis spectra were recorded with a Spectrophotometer UV-Vis-NIR (Shimadzu UV-3600). The irradiation lamp was a UV lamp with λ_{max} of emission centered around 366 nm (Benda NU-8 KL), 87 $\mu W/cm^2$.

References

1 Crivillers, N., Orgiu, E., Reinders, F., Mayor, M. & Samorì, P. Optical Modulation of the Charge Injection in an Organic Field-Effect Transistor Based on Photochromic Self-Assembled-Monolayer-Functionalized Electrodes. *Advanced Materials* **23**, 1447-1452 (2011).

2 Bozano, L. D. *et al.* Organic materials and thin-film structures for cross-point memory cells based on trapping in metallic nanoparticles. *Advanced Functional Materials* **15**, 1933-1939 (2005).

3 Sirringhaus, H., Tessler, N. & Friend, R. H. Integrated optoelectronic devices based on conjugated polymers. *Science* **280**, 1741-1744 (1998).

4 Wu, S. M. *et al.* Molecular junctions based on aromatic coupling. *Nature Nanotechnology* **3**, 569-574 (2008).

5 Raimondo, C., Reinders, F., Soydaner, U., Mayor, M. & Samorì, P. Light-responsive reversible solvation and precipitation of gold nanoparticles. *Chemical Communications* **46**, 1147-1149 (2010).

6 Nicholson, P. G., Ruiz, V., Macpherson, J. V. & Unwin, P. R. Effect of composition on the conductivity and morphology of poly (3-hexylthiophene)/gold nanoparticle composite Langmuir-Schaeffer films. *Physical Chemistry Chemical Physics* **8**, 5096-5105 (2006).

7 Park, Y. D. *et al.* Solubility-Induced Ordered Polythiophene Precursors for High-Performance Organic Thin-Film Transistors. *Advanced Functional Materials* **19**, 1200-1206 (2009).

8 Schonhoff, M., Mertesdorf, M. & Losche, M. Mechanism of photoreorientation of azobenzene dyes in molecular films. *Journal of Physical Chemistry* **100**, 7558-7565 (1996).

9 Arkhipov, V. I., Heremans, P., Emelianova, E. V., Adriaenssens, G. J. & Bässler, H. Equilibrium trap-controlled and hopping transport of polarons in disordered materials. *Chemical Physics* **288**, 51-55 (2003).

10 Calhoun, M. F., Hsieh, C. & Podzorov, V. Effect of interfacial shallow traps on polaron transport at the surface of organic semiconductors. *Physics Review Letters* **98** (2007).

11 Chen, C. C., Chiu, M. Y., Sheu, J. T. & Wei, K. H. Photoresponses and memory effects in organic thin film transistors incorporating poly(3-hexylthiophene)/CdSe quantum dots. *Applied Physics Letters* **92** (2008).

12 Egginger, M., Bauer, S., Schwodiauer, R., Neugebauer, H. & Sariciftci, N. S. Current versus gate voltage hysteresis in organic field effect transistors. *Monatshefte fur Chemie* **140**, 735-750 (2009).

13 Cheng, H. L., Lin, W. Q. & Wu, F. C. Effects of solvents and vacancies on the electrical hysteresis characteristics in regioregular poly(3-hexylthiophene) organic thin-film transistors. *Applied Physics Letters* **94** (2009).

14 Sethuraman, K., Ochiai, S., Kojima, K. & Mizutani, T. Performance of poly(3-hexylthiophene) organic field-effect transistors on cross-linked poly(4-vinyl phenol) dielectric layer and solvent effects. *Applied Physics Letters* **92** (2008).

15 Chen, S. W. Langmuir monolayers of gold nanoparticles: from ohmic to rectifying charge transfer. *Analytica Chimica Acta* **496**, 29-37 (2003).

16 Adams, D. M. *et al.* Charge transfer on the nanoscale: Current status. *Journal of Physical Chemistry B* **107**, 6668-6697 (2003).

17 Manceau, M. *et al.* Effects of long-term UV-visible light irradiation in the absence of oxygen on P3HT and P3HT:PCBM blend. *Solar Energy Materials and Solar Cells* **94**, 1572-1577 (2010).

18 Mativetsky, J. M. *et al.* Azobenzenes as light-controlled molecular electronic switches in nanoscale metal-molecule-metal junctions. *Journal of the American Chemical Society* **130**, 9192-9193 (2008).

19 Choi, S. H., Kim, B. & Frisbie, C. D. Electrical resistance of long conjugated molecular wires. *Science* **320**, 1482-1486 (2008).

20 Chua, L. L. *et al.* General observation of n-type field-effect behaviour in organic semiconductors. *Nature* **434**, 194-199 (2005).

21 Cheng, H. L., Lin, W. Q. & Wu, F. C. Effects of solvents and vacancies on the electrical hysteresis characteristics in regioregular poly(3-hexylthiophene) organic thin-film transistors. *Applied Physics Letters* **94**, 223302-223304 (2009).

22 Ferri, V. *et al.* Light-powered electrical switch based on cargo-lifting azobenzene monolayers. *Angewandte Chemie International Edition* **47**, 3407-3409 (2008).

23 Wasapinyokul, K., Milne, W. I. & Chu, D. P. Origin of the threshold voltage shift of organic thin-film transistors under light illumination. *Journal of Applied Physics* **109**, 084510-084514 (2011).

24 Guo, J. M., Ohkita, H., Yokoya, S., Benten, H. & Ito, S. Bimodal Polarons and Hole Transport in Poly(3-hexylthiophene):Fullerene Blend Films. *Journal of the American Chemical Society* **132**, 9631-9637 (2010).

Chapter 7. Conclusions and Outlooks

In summary, azobenzenes coated gold nanoparticles, 1-30 nm in size, have been synthesized and used as building blocks for the fabrication of complex devices.

Importantly, thiolated azobiphenyl molecules have been shown to undergo *trans-cis* isomerization even when chemisorbed on gold nanoparticles, differently from what normally demonstrated for other azobenzene molecules. The surface plasmon resonance, in this particular case, does not quench, the excited levels of the molecules, and the isomerization is allowed, as demonstrated by UV-Vis, ^{1}H-NMR and surface enhanced raman spectroscopy studies.

An aggregation/solvation process have demonstrated to reversibly occur when the nanoparticles are irradiated with UV light, and the azobenzene coating them is allowed to undergo isomerization from the *trans* to the *cis* form. Such process was found being reversible upon illumination with visible light.

By tuning the interaction between single nanoparticles it is possible to smart embed them in a second material granting prediction of, for example, the charge transfer mechanism involved.

A study of the kinetics of the isomerization process allows both understanding of the high stability of the *cis* form and of the high yield os *trans* to *cis* isomerization

when adsorbed on flat surfaces. A dependence of the kinetic constant of the back *cis* to *trans* isomerization from the sizes of the nanoparticles considered has been found, demonstrating an effect of the pi-stacking on the stability of the *cis* form.

Azobenzenes have been integrated into nanotrenches, with horizontal geometry, connected by micro or nanospheres and the current characteristics of both isomers have been measured. When working with tranches separated by 100 nm gaps, high reproducibility have been found over multiple switching cycles in air. The 50 nm gap electrodes showed switching behavior as well over the full nanojunction and an interesting dependence of the color in c-AFM mapping images from the number of nanoparticles connecting the electrodes when zooms over areas are considered. The nonresonance decay factor extracted from these measurements was consistent with the one measured with other techniques.

High statistics is possible with few measurements using this last method.

Finally, a mixture of azobenzene coated gold nanoparticles and a polymeric p-type semiconductor have been utilized in organic field-effect transistors. An increase in current occurred when the device was subject to UV light and over 25 switching cycles were performed without performances loss. The device was found to be multiresponsive, *i.e.* tunable by application of both an optical and an electrical gate. An explanation of the charge transfer mechanism has been proposed as well by coupling electrical measurements with spectroscopy.

Metallic nanoparticles thus have been proven being versatile and nanostructured building blocks that can be used as nano-scaffolds once decorated with functional moieties to form a nanostructured material with tailored properties. It is possible to foresee their functionalization to allow them to respond to various external stimuli such as pH, pressure, etc. Multicomponent materials can be intermixed in a "smart" way in order to induce selective gradients and segregation at the nanoscale, as well as space-dependent behavior in large-scale devices. Hence, smart architectures can be engineered by exploiting fundamental physico-chemical characteristics of the studied system, to generate multi-responsive devices with properties that are tuned at both single molecule level and ensemble level.

UNIVERSITÉ DE STRASBOURG

Corinna RAIMONDO

Photoresponsive gold nanoparticles: Towards Multi-functional Organic Electronics Devices

Les trois dernières décennies ont vu l'émergence de l'Electronique Organique ainsi que son établissement en tant que domaine scientifique interdisciplinaire et dans notre vie quotidienne. On dénombre actuellement deux défis scientifiques majeurs dans ce domaine. Le premier est de s'attacher à augmenter l'efficacité des dispositifs par l'utilisation de nouveaux matériaux, plutôt le deuxième consiste en l'intégration de fonctionnalités multiples un seul dispositif. Atteindre ces objectifs nécessite la compréhension des mécanismes fondamentaux de la physico-chimie, gouvernants les propriétés de base de l'électronique organique tels l'injection ou le transfert de charge et le transport. Ces travaux de thèse rapport le développement de systèmes complexes, auto-assemblés, dont les propriétés électriques et optiques au sein de dispositifs organo-électroniques peuvent être modulées en réponse aux stimuli extérieurs. Ce but a été obtenu par le développement des briques élémentaires et par l'étude de leurs propriétés physico-chimiques afin de modéliser tous les mécanismes impliqués.

In the last three decades *Organic Electronics* emerged and established itself as an interdisciplinary field of science and as part of our daily life. Presently, the greatest scientific challenges in this field of research are two: the former relies on the improvement of devices efficiency which can be accomplished by using new materials, whereas the latter consist in the integration of multiple functionalities in a single device. To accomplish these goals one needs to develop a deep understanding on the fundamental physical-chemistry ruling the properties which are on the basis of organic electronics such as charge injection, charge transfer and transport. This PhD project reports the developing of efficient multicomponent electroactive self-assembled systems whose electro- and optical properties can be modulated, in devices, as a response to multiple external and independent stimuli. This goal has been achieved by engineering of the proper building blocks and the study of the the physico-chemical properties to be able to model all the mechanisms involved.